博士論文

Design of Multitone Waveforms for
RF Energy Harvesting Systems

（RFエネルギーハーベスティングシステムを実現する
マルチトーン波形の設計）

2020年12月4日

Graduate School of Information Science and Technology,
The University of Tokyo

池内　尚史

指導教員　　川原　圭博　教授

Abstract

The achievements made through the development of science and technology have been changing our lifestyles more conveniently. The integrated circuits introduced in almost every electronic device nowadays enable such devices more portable, more convenient, and more energy-efficient. Recently, the Internet of Things (IoT) has been widely known to people around the globe; collecting a considerable amount of information will become a new paradigm for humans to yield better quality of life, efficient operations in factories, and so forth. In making this paradigm, low power operations of sensor devices become one of the keys as the power supply becomes cumbersome when all these devices need to be connected through the cable or embed batteries that require periodic recharge frequently. An extreme version of low power operated sensors is the devices that work without batteries, which can be seen in daily life as a radio frequency identifier (RFID) tags, transportation cards, and as such. These devices cannot operate computationally intense tasks; however, simple sensing tasks can be substituted by these devices. Recent progress has made it possible to add software-programmable functions by users to such devices known as wireless identification sensing platforms (WISPs), which will expand the wide use of battery-less devices.

Battery-less devices require an external power source for operations. Radio frequency (RF) wireless power transfer (WPT) technology is receiving a lot of attention as a means of power supply to support the spread use of these battery-less devices. Recently the opportunities to exchange information through wireless transmission have been increasing, which results in flowing enormous amount of electromagnetic (EM) waves around us. In addition, the technologies to extract power from the EM waves have made it possible to extract sufficient power to drive simple sensors; conveniently harvest from the environment becomes one of the reasons for gaining the attention for the battery-less devices as a primary source of energy. However, the integration of power consumption from the clock, peripheral modules results in requiring mW of power even for battery-less devices to operate, which is beyond the limit that the ambient energy harvesting can supply. Therefore, relying on ambient energy from the environment still has a leap for supplying such devices; dedicated RF power sources are necessary to power these devices.

The origins of RF WPT date back to more than 100 years. In the past, researches on wireless power to devices such as helicopters and to the ground from space were prevalent applications for the RF WPT. Beamforming techniques were applied to such applications to deliver high power. Although such techniques are very promising for powering the battery-less devices, the required knowledge of channel state information (CSI) burdens the devices to calculate and deliver the information, which is cost-full operations for such devices. Recently, there is a growing expectation for WPT using multitone waveforms, where multiple tones are added to form beat-tones waveforms so that it generates a high peak to average power ratio. This nature results in having better efficiency without increasing the transmit power due to the nonlinear behaviors at the receiver side. In addition, naive multitone waveforms require very simple feedback techniques, if any, as opposed to beamforming, which is attractive for computationally limited devices. Thus, these techniques become necessary for operating battery-less devices. However, there are few studies that discuss the relationship between the parameters of multiple sine waves and the configuration of the receiver, and it is not clear what kind of waveforms should be created for the actual receiver circuit configuration in order to have better efficiencies or sensitivities. Failing to design proper waveforms results in deterioration of such performances, and thus it is important to tackle such problems.

Based on these issues, this paper proposes the following for RF WPT using multitone waveforms.

- Waveform design method for improving power conversion efficiency (PCE) performances based on the receivers' parameter characterizations are proposed. Prior to that, the PCE performances depending on the configurations of rectifiers are characterized based on rigorous experiments at UHF, including wire and wireless transmissions as well as noise conditions. The experiments show that there exist specific points (saturation points) for frequency spacing that multitone waveforms have to assign to improve the PCEs, and the saturation points can be controlled or strongly affected by the value of storage capacitance at the receiver. These investigations result in introducing the design instructions for multitone waveforms depending on the receiver circuits.

- Waveform design methods of increasing the sensitivities or peak voltage acquisitions are proposed. The performance of sensitivity or peak voltage acquisitions has also been characterized prior to this. Similar to the previous case, the saturation points can

be controlled or strongly affected by the value of storage capacitance at the receiver. However, based on the results, the frequency spacing of the multitone waveforms needs to be smaller than the saturation point of the peak voltage acquisition, which is one of the unique findings in contrast to the case for the PCE cases. In addition, the relation between the saturation point of PCEs and peak voltage acquisitions have been revealed. Based on the sensitivity analysis using practical devices, it has been revealed that the characterizations of the sensitivities of receiver devices depend on the types of DC–DC converters.

- Waveform design method for transmitting both information and power simultaneously has been proposed using multitone waveforms. The design waveform utilizes the nature of nonlinear devices, thereby generating varieties of output by shifting the tone configurations of the waveforms. Based on the analysis by simulations and experiments, it is possible to categorize the nonlinear outputs based on the arrangements of the intermodulation products (IM2s). It is also tested by the manufactured SWIPT circuits and verify that design waveforms can transmit information while transmitting power, which results in suppressing the voltage drop that occurred when transmitting information by utilizing frequency-shifted multitone waveforms.

Acknowledgement

I am grateful to my supervisor, Professor Yoshihiro Kawahara for instructing me during my carrier as a master and Ph. D. student. I am deeply grateful to Honorary Professor Tohru Asami for instructions during a master student as well as proof readings of papers before submissions with insightful indications. I am appreciated to Professor Joshua R. Smith for having me participating in his labs during the during the visit in Seattle as well as giving instructions with regard to research.

I am also appreciated to committees, Honorary Professor Tohru Asami, Professor Yoshihiro Kawahara, Professor Kaoru Sezaki, Associate Professor Makoto Takamiya, Associate Professor Shinya Ochiai, Associate Professor Shinya Sugiura for giving me a lot of comments to strengthen this thesis. Also I am appreciated to advisors, Associate Professor Yoshihiko Hasegawa, and Professor Kaoru Sezaki to have meetings to give me helpful comments and follow-ups. I also appreciated to EE and GCL officiers to help submitting a lot of paper works including scholarships.

I would like to express a great thanks to Dr. Yoshiaki Narusue, Dr. Masaru Takagi, Dr. Ryo Shigeta, Dr. Koya Narumi, Dr. Fuminori Okuya, Dr. Tung Duc Ta for a lot of instructions, proof reading, research collaborations, as well as daily conversations during my stay in Kawahara lab. I am gratefully thanks to my colleague Takuya Sasatani and Tatsuya Iizuka to share most of my time during as a student with a lot of advice not only with regard to research, but also daily lives. In addition, I would give special thanks to Ryo Takahashi, Matthew Ishige, Kazunobu Sumiya, Natsuki Ikeda, Yuki Nishizawa, Kouta Suzuki, Ken Takaki, and Hiromasa Hayashi for sharing a lot of things. I also give thanks to Ren Kurosawa, Masahiro Morita for the collaboration with some projects. I would thank to other members of Kawahara lab to have a great discussions with related to research.

I would like to give a special thanks to the lab members of the sensor systems labs in

University of Washington including summer intern students. I have learned a lot of things thanks to the heartful advices from Dr. Vaishnavi Ranganathan, Zeria Kapetanovic, Brody Mahoney. I also would like to express thanks to Gregory Moore for taking me a lot of places, helping me more engaged with labs members, Patrick Lancaster, Boling Yang, Ali Saffari Dr. Xingyi Shi and Dr. Saman Naderiparizi for giving me encouragement. I would like to give a greateful thanks to Jared Nakahara for proof readings as well as research discussions.

Finally, I would like to deeply give special thanks to my parents and brother for encouraging me in every aspect of my time during my life with great support.

Contents

List of Tables

List of Figures

CHAPTER 1

INTRODUCTION

1.1 Background

With the development of science and technology so far, integrated circuits have made it possible to achieve higher performance and smaller sizes in various electronic devices. This drives the prevalent use of terms, the Internet of Things (IoT); collecting a considerable amount of information will become a new paradigm for humans to yield better quality of life, efficient operations in factories, and so forth. In making this paradigm, low power operations of sensor devices become one of the keys as the power supply becomes cumbersome when all these devices need to be connected through the cable or embed batteries that require periodic recharge frequently. Nowadays, battery-free sensor devices have been gradually introduced in daily life. The prices of the items are automatically calculated using RFID tags, and transportation payments are conducted through the transportation cards. RFID/NFC tags unleash from

periodic charging, in contrast to smartphones. These devices cannot operate computationally intense tasks; however, simple sensing tasks can be substituted by these devices. In addition, recent progress has introduced wireless identification sensing platforms (WISPs), which add programable functionalities to the sensors, so the user can modify the sensors as they like; this will become the way things should be for the next generation of RFIDs.

Battery-less devices require an external power source for operations. Radio frequency (RF) wireless power transfer (WPT) technology is receiving a lot of attention as a means of power supply to support the spread use of these battery-less devices. Recently the opportunities to exchange information through wireless transmission have been increasing, which results in flowing enormous amount of electromagnetic (EM) waves around us. In addition, the technologies to extract power from the EM waves have made it possible to extract sufficient power to drive simple sensors; conveniently harvest from the environment becomes one of the reasons for gaining the attention for the battery-less devices as a primary source of energy. However, the integration of power consumption from the clock, peripheral modules results in requiring mW of power even for battery-less devices to operate, which is beyond the limit that the ambient energy harvesting can supply. Therefore, relying on ambient energy from the environment still has a leap for supplying such devices; dedicated RF power sources are necessary to power these devices.

There are various methods of receiving energy from the outside, such as photovoltaic and wind power, and the methods summarized by N. Garg et al. and their characteristics are shown in Fig. 1.1 [1]. With respect to harvest energy from wind energy and human motion, the availability of these energy is limited due to the geographical limitations of implementing the source or limited amount of harvesting energy. Therefore, utilizing these techniques to the applications to battery-less IoT devices is challenging. Unlike such techniques where the energy can be obtained continuously, the methods of energy harvesting using sunlight, light, and electromagnetic waves can obtain energy occasionally, but the geographical limitations are relatively small. Wireless power transmission using electromagnetic waves is particularly attractive because it can superimpose power as well as information. In addition, installing transmit sources are easy if the regulations are met. With the resent advances of using WPT

Energy source	Characteristics	Harvester	Power Density	Advantages	Disadvantages
Solar energy	Ambient, Uncontrollable, Predictable	PV Panel	15 - 100 mW/cm2	Consistent; Available during daytime; high output voltage;	Not available in night; efficiency is low during cloudy days; Deployment Constraints
Wind energy	Ambient, Uncontrollable, Predictable	Anemometer	1200 mWh/day	Available in open areas	Not available in closed areas
Finger Motion	Active human power, fully controllable	Piezoelectric	2.1 mW	Available whenever needed	Energy is harvested only when finger is moved
Footfalls	Active human power, fully controllable	Piezoelectric	5 W	Available whenever needed	Highly variable output
Vibration (indoor Environments)	Ambient, Uncontrollable, Unpredictable	Electromagnetic Induction	0.2 *mW/cm*2	Without voltage source	Brittle materials
Thermal Energy	Ambient, Uncontrollable, Unpredictable	Thermocouple	≅50 mW/cm2	Long life, reliable with low maintenance	Low energy conversion efficiency
Motion	Non-Ambient, Controllable, Partly-predictable	Piezoelectric	200 μW/cm2	Light weight	Highly variable output
Breathing	Passive human power, uncontrollable, unpredictable	Ratchet-flywheel	0.42W	Available all the time.	
Radio frequency	Non-Ambient, Partly-controllable, Partly-predictable	Rectennas	1 μW/cm2	Sufficient in urban areas; very high energy density; Allow mobility	Few in suburbs; material in radioactive are extremely dangerous; low power density

Fig. 1.1: Energy harvesting methods and available energy by N. Garg, *et al* [1]

technique applies multiple energy harvesting techniques. In [2, 3], battery-less devices and rectifiers combine one or more of these harvesting techniques with the wireless power transfer techniques to acquire energy as needed. In this thesis, I focus on far field wireless power transfer technology that is relatively resistant to misalignment. Although they have a relatively low receiveable energy density of approximately 1 $\mu W/cm^2$, especially in urban areas, they can always receive energy from the towers and increase this receiveable energy density by installing new transmission sources. The evolution of wireless power transfer technology and trends in wireless power transfer technology for battery-less IoT devices are described in the subsequent sections.

1.1.1 Classifications of Wireless Power Transfer Method and Features

Wireless power transfer (WPT) method can be classified into two methods; coupled-based and radiated-based [4]. The former method is also known as near field WPT and can be fur-

ther classified according to whether it resonates between transmission and reception. One of the problem with regard to the couple-based WPT is that misalignment between the transmitter and the receiver sides causes severe performance degradation. Furthermore, because the system performance relay on the coupling state, it has been vulnerable to the change of the distances between the transmitter and receiver sides. However, when resonance based near field WPT has been explored from Massachusetts Institute of Technology (MIT) in 2007, these problems are mitigate to some extent and the couple-based WPT has gained attentions not only in the research field, but also industrial perspectives [5, 6]. Nowadays, the area of applications expands not only from point to point wireless transmission, but also to 2-dimension as well as 3-dimension [7, 8]. One of the epoch making research with regard to couple-based WPT system is that it is possible to make a room-scale cavity where the nodes can receive power anywhere inside it [9, 10].

In contrast, radiated-based or far field WPT does not assume the coupling between the transmitter and the receivers. Therefore, the distance between the transmitter and receiver sides are assumed to be far. In this thesis, the distance between the both sides are assumed to be far more than $2D^2/\lambda$, where D is the antenna length and λ is the wave length of the transmitted waveforms. In far field WPT, the movement of the antennas at the receiver side does not affect to the behavior of transmitter unlike in near field WPT [11]. However, when the transmitted waveforms formed narrow beam to increase gain, the antenna placement also becomes problem in this method as well [12, 13].

1.1.2 History and the Transition of Microwave Power Transfer

Nicola Tesla firstly attempted the experiment with regard to radiated WPT in 1899. Because it had conducted with relatively low frequency (150 kHz), the received power was very small. One of the major works have been conducted by W. Brown where he wirelessly powered to the flying helicopter [14, 15]. In addition to this, he developed the WPT system that can achieve 54% DC to DC transfer efficiency, which has never been beaten by now [16]. At that time, the transmitter produces a narrow beam to concentrate on the microwave power and sent to the receiver. The structure of the receiver at that time consisted of the combinations of

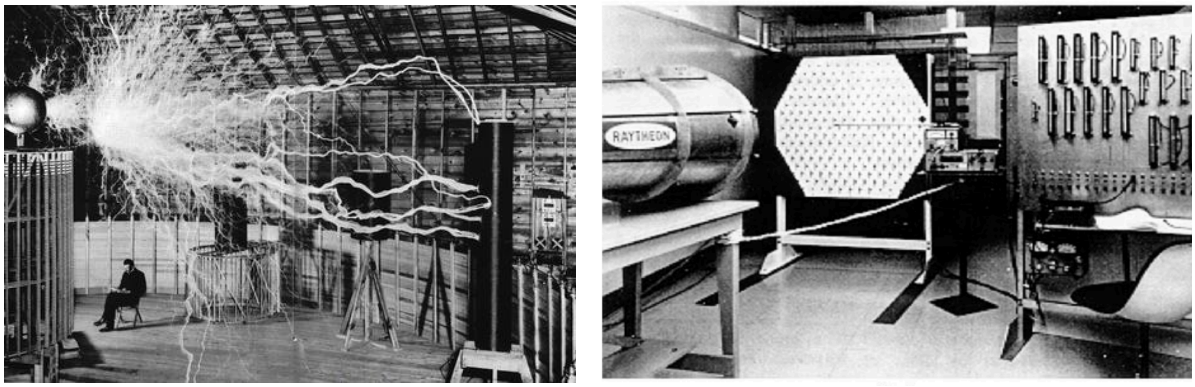

Fig. 1.2: (a). Nikola Tesla's experiment with radio waves in his Colorado Springs Laboratory by Brown *et al* [17]. (b). High efficient wireless power transmission achieved 54% DC to DC conversion efficiency by Brown *et al* [16].

the multiple rectennas in order to increase aperture of the antenna. As a results the wireless power is transferred in a Fresnel's region (in between the near field and far field) where the waveforms are treated as the spherical wave. These techniques resulted in having high RF–RF conversion efficiency which was assumed to be obtained more than 90% efficiency [13]. Also, space solar power systems (SSPS) have been advocated by Dr. Peter Glaser around this age (1968) [14, 15]. It has been said that SSPS needs to be accomplished using the Fresnel's region to efficiently deliver power from the space by increasing the antenna aperture areas [13].

However, thanks to the development of amplifiers or electric circuits, wireless signals can be obtained even with very small signal level [13]. This had resulted in the growth of wireless communication technology faster than the wireless transfer technology. Along with that the standards with regard to wireless communications had developed in order to handle interference. Because wireless power transfer signal deal with higher power than wireless communications, high power transmissions were gradually regulated to prevent wireless communications, which made the WPT system to develop harder from what it used be [17].

Nowadays, as the use of wireless communication such as the Internet connection through phones, e-mails, and TV broadcasts expands, electromagnetic waves ubiquitously spread

around our environment. Thus, energy harvesting techniques that receives the electromagnetic waves and extracts electric power from these technologies from them has emerged [18, 19]. Although typical receiving power can be approximately μW power level, simple sensing systems that are consisted of low power microcontrollers and sensors can be operated around several 100 μW nowadays, so the level of the power reception and the operation power of sensing systems become closer [13]. Because of this, microwave power transfer has been regaining its attention for the sake of enabling IoT. In contrast to the circuit system so far where the receiver needs to embed a lot of rectennas to have wider antenna aperture area with high power reception [17], the power receiving circuit has become more simple; with only one receiving antenna is embedded to the system and the rectifiers are designed not only for the sake of increasing the RF–DC conversion, but also for having higher voltage acquisition at relatively low power range (-10 dBm input power or smaller) [20]. For the former single shunt-type rectifiers are gaining attracted as well as voltage doubler-type rectifiers that are seen in the commercial devices [21, 22, 23, 24]. For the latter, multi-stage rectifiers have been developed, which helps operating the DC–DC converter by applying higher voltage to the system with low receiving power [25, 2, 26]. In this thesis, relevantly used voltage doubler-type rectifiers are used. However still in practical use of the sensors, operation power exceeds 1 mW of power, which is hard to collect from ambient electronic waves [27]. Therefore, possible solution still requires dedicated RF power sources in order to give the sensors to have necessary power for operations.

Based on these transitions, the recent research areas of wireless power transfer technology for the battery-less IoT can be broadly classified into the development of circuit elements, innovations in radio wave transmission technology, optimization in the upper layer, and application studies [28]. The following is an overview of research trends in these areas.

1.1.3 Research Overview on Low Power Devices for Wireless Power Transmission

Circuit Level Explorations

Typical circuit structure is consisted of antennas, matching networks, rectifiers, storage, and loads including DC–DC or boost converter. At each component, extensive researches have

been conducted. Recent explorations of the antenna techniques can receive multiple frequencies by printing different length of antenna in a patch [29]. Other work produced the rectenna without having matching network by placing the feeding point in an asymmetric manner in such a way that the antenna impedance should match to the subsequent circuit components [30]. The antennas and the rectifier designs are some times developed at the same time as rectenna [2, 31].

Usually, impedance matching is conducted to align the impedances between the antenna and the subsequent circuit system. Therefore, the network fulfills the impedance transformer [32, 33]. When the impedance of the subsequent circuit system is significantly higher than the antenna impedance, higher voltage can be induced to the system. In [34], sensitivity increase can be achieved by utilizing this technique. In its implementation, transformer was used, which was connected to the amplifier. Transformer enabled matching network was often implemented on-chip circuits [35, 36, 37]. One of the difficulties of using transformer impedance matching is that the number of coil turns are determined by the input impedance of the subsequent circuit system, which means that turning many times does not lead to yielding higher voltage. Therefore, for usual rectifier design, LC circuits are utilized, which also can filter out the unnecessary frequency bands.

One of the important element in developing a rectifier is diodes. Schottky diodes have been utilized due to the low forward voltage drop and fast switching speed. The diodes' efficiency comparisons are shown in Fig. 1.3. As it can be seen from the figure, the trends show that diodes have been used for relatively higher power (0 dBm input power) in order to achieve higher RF–DC conversion efficiencies. After SMS7630 or HSMS285 series have been manufactured, higher RF–DC conversion efficiency can be achieved with lower input power (-20 dBm) [20, 39]. In order to further increase the RF–DC conversion efficiency within the same input power X. Gu *et al* gave attention to the nature of the diode in that when the temperature is low, the efficiency becomes better [38]. In addition the same group achieved a higher efficiency by adding current flowing to the diode by using different energy harvesting source such as solar power [40].

In contrast, recently, the use of the tunnel diodes have been attracted [41, 42]. One of the

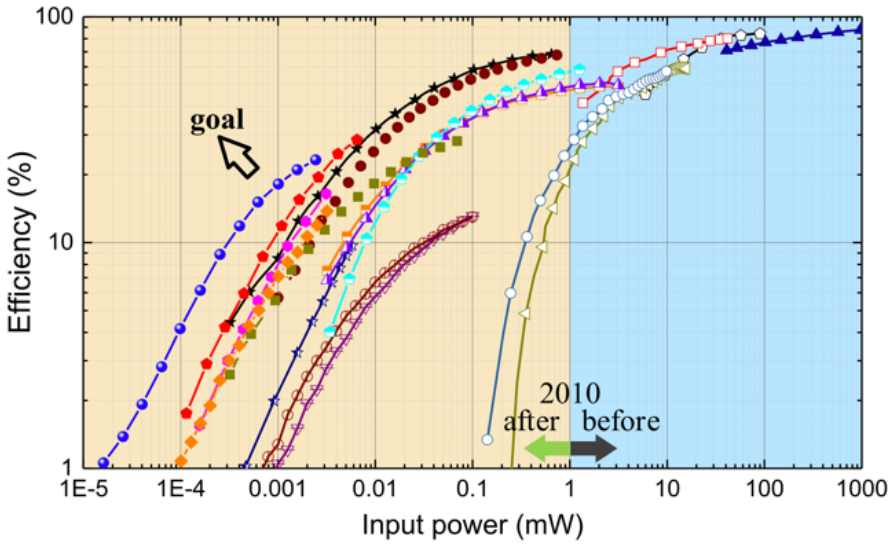

Fig. 1.3: Diode RF–DC conversion comparison by X. Gu *et al* [38]

features of them is that the Zener effect occurs even with near around the zero biased point. Therefore, if the tunnel diodes are oppositely placed and negatively biased to the diode, the rectification can be achieved with very small input power level (-40 dBm). The state of the art rectifier can achieve RF–DC efficiency more than 10% with -30 dBm input power [3]. Another effect of the use of the tunnel diode is the existence of the negative resistance where at some voltage range, when the applied voltage is increased the amount of the current that goes through the diode decreases. Some works have used these techniques to amplify the backscatter signal radiated from radio frequency identification (RFID) tag, or even amplify the transmitter signal by reflecting the already sent signal that has been backscattered by the tag around it [43, 44, 45, 46]. Because the operated power is very small the tunnel diodes are useful in such scenario to increase the backscatter signal range or wireless communication without using amplifiers, so they will become one of the most important devices in the future. However at this moment, the tunnel diodes are not commercially available and it is required to be biased. Therefore it is harder to utilized them as a way to increase the power conversion rate with the rage of -20 to 0 dBm input power whose power is required to drive battery-less IoT devices [38].

System Level Exploration In terms of system level explorations, a lot of studies focused on developing devices with low-power operations; wake-up circuit, backscatter communications, compressed sensing, and so forth. The implementation of a wake-up circuit that keeps the system in deep sleep except when sensing is needed to achieve low-power operation can extend the devices operational distances [47]. A low-power circuit waits for the wake-up signal to come in, where they embed low-power comparators so that even the wake-up signal is weak, they can detect the signal and starts its operation. Although it consume some amount of power during the sleep state read range became -32 dBm, which is a significant increase compared to other devices that does not require active elements for wake-ups [48]. However, This receiver circuit consumes 152 nW in standby mode and requires 600 μW to operate the reading circuit. Along with wake-up methods, Duty-Cycling methods are also reported where the devices cyclically wakes up by themselves instead of waiting until others forces to [49, 50, 51, 52].

Recently, the application spaces of battery-less devices are growing. One of the epoch making devices are the wireless identification sensing platforms (WISPs), which are implemented at the University of Washington [26]. Unlike the conventional RFID systems where the RFID tags are hidden to the manufacturers, WISPs added the functionalities of computational resources to the sensors thereby users can implement sensing devices by their needs. WISPs do not require batteries; instead they collect energy from RF energies or other energy harvesting devices such as solar power. So far these devices can probe not only temperatures, but also taking photos, streaming videos, making calls through Skypes [2, 53]. However, the more people demand for such devices to do expensive operations, the more energy they require for operation. For example, capturing per frame image consumes 10.4 mJ, so increasing frame rate requires more energy for operation, and there is a trade off between level of operations and working range [54]. In [55], an RF source is obtained from a TV tower to enable inter-tag communication without the need for an RF source of its own. Because ambient radio waves in the environment does not power enough to drive sensors that can perform expensive process when combined with peripheral circuits there have been enormous contributions to be investigated. Firstly, a power-saving method for information retrieval has been

proposed in a way to smooth the received radio wave without using a high power-consuming oscillator or AD converter, which has been used in conventional tags. Secondly, the Analog Digital Converter (ADC) and Digital Analog Converter (DAC), which were essential for conventional communication, were eliminated and the power consumption of communication is reduced to 3.48 μW by communicating directly with backscatter. It has been reduced to the lowest possible level [2]. A method of using the power radiated from the Wi-Fi access point to drive sensors attached to the tag side has also been investigated, where dummy packets, called power packets, are radiated to Wi-Fi while no communication is taking place to compensate for the lack of power at the receiver side [54].

Transmission Techniques for WPT Transmitted waveform designs have been designs in order to increase the received power or to send both power and information simultaneously. For the former case, beamforming methods are one of the common methods to increase the higher power at the receiver side from multiple sources or antennas. This enables to reduce output power from transmitter side but increase the received power at the receiver side [56, 57]. Instead of stearing beam to a specific receiver, distributed beamforming enables to deliver waveform to have wide area coverage. However these techniques require synchronizations between the transmit antennas or require to have channel state information (CSI) in order to stear specific point [58, 59].

In contrast, these days other type of waveform has been investigated, which enables to design it using a single antenna. Therefore, it does not require to have synchronizations. The method focuses on designing waveforms such that they produce higher peak to average power ratios thereby increasing the power conversion efficiency due to the use of the nonlinearity in the diodes. This results in having better efficiency than using the continuous wave that has been assumed to be utilized usually as a way to convey power.

The technology for transmitting power and information has been studied in various fields. Power Line Communication (PLC) is an well known techniques to achieve through wire transmission [60]. In wireless communication field, it is generally granted as Simultaneous Wireless Information and Power Transfer (SWIPT). Although the transmission of information and the transmission of electric power are technologies that use the same electromagnetic waves,

they have been evolved as two separate fields [61]. Because digital communication is commonly used in wireless communications, it is difficult to combine wireless power transmission that requires analog processing with the same circuit structure. Therefore, SWIPT in wireless communication field mainly focuses on the trade-off between power allocation and communication capacity, such as how to distribute the required power resources between wireless communication and wireless power transmission, or when to switch the transmission lines between power rectifier or information decoder depending on the battery status of the receiving devices [57, 62, 63, 64]. Therefore, the waveform design for wireless transfer in such field assumes continuous wave and there are few papers that discuss how to realize power transmission in practice. In addition, SWIPT in devices that are predicated on digital communication is impractical because the power obtained by receiver devices is limited to about -10 dBm, which is very small compared to the power consumed by wireless communication. In contrast, for SWIPT system in wireless power transmission, the method of superimposing information on the power transmission waveform has been investigated in recent years [65, 66, 67, 68]. Since this technique often demodulates information in an analog fashion, it can exchange information with low power consumption without the need to use modern digital wireless communication technologies. True that in such case, the communication rate cannot be as fast as what is achieved in the state of the art wireless communication techniques. However, in battery-less IoT devices, the communication rate relatively small is enough for most of the applications. As battery-independent IoT devices become more widespread in the future, this kind of technology that can transmit information while reducing power consumption will be very attractive.

Trends in Standardization The standardization of WPT systems began in 1978 at the Comité consultatif international pour la radio (CCIR), the predecessor of the International Telecommunication Union Radiocommunication Sector (ITU-R). After that, due to the technological development of the coupled radio power transfer, the coupled WPT and the radiated WPT were discussed separately as NON BEAM WPT and BEAM WPT, respectively, at the SG1 meeting of ITU-R in 2013 [69, 70]. Particularly for BEAM WPT, Report ITU-R SM.2392 was published in 2016, which envisages detailed target applications and wireless power trans-

mission in the frequency domain [71]. In addition, the recent ITU-R SM.[WPT.BEAM.FRQ] recommendations for BEAM WPT applications are (1). Wireless Charging of Mobile/Portable Devices and (2). The frequencies to be used for each are (1). The frequencies to be used are (1) 915 MHz band (902 MHz–928 MHz), 2.4 GHz band (2400 MHz–2500 MHz), and 5.7 GHz band (5725 MHz–5875 MHz) for (2) 920 MHz band (915 MHz–930 MHz), and 5 GHz band (Sub-GHz wireless power supply [72, 73].

Based on the above, the Wireless Power Transmission Working Group (WPT-WG) of the Broadband Wireless Forum (BWF) has proposed milestones for practical applications. Especially, in sub GHz band, WPT system assumes to power IoT sensors in factories and mobile devices in indoor/outdoor [74]. The waveform designs of sub GHz band is allowed to have flexibilities so that the power and information can be transmitted depending on the designs of the waveforms, which is different from other frequency band where the information is transmitted through other communication modules like Bluetooth. On the other hand, due to gain limitations, the transmit power is relatively small compared to other systems (50 W equivalent isotropically radiated power EIRP at most) [74]. Although it is difficult to narrow down the beam and increase gain compared to high frequency, sub GHz band can spread the electromagnetic wave dispersively to power many sensors and devices, which is essential for enabling the sustainable IoT where the devices are located ubiquitly. Thus it plays crucial roles, and investigating this band is important. These propositions are established with the help of wireless power transfer consortium for Practical Applications (WiPoT), which is a Japanese organization established in 2013 for the purpose of standardization, safety, and discovery of needs for the practical use of microwave wireless power supply, and proposes possible applications and power requirements based on the frequencies used [75].

On the other hand, the handling of radio waves needs to be established as soon as possible. In Japan, NON BEAM WPT can be used as a high-frequency application facility as long as it is not used for communication, while radiated BEAM WPT has no system in place at this time, and it is basically necessary to apply to the Ministry of Internal Affairs and Communications as a radio facility and conduct experiments. The system for BEAM WPT is not yet in place. These systems are being developed and are expected to become internationally advanced.

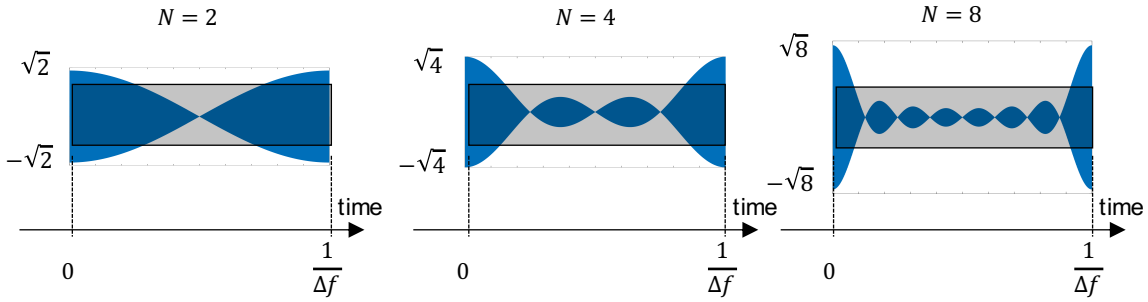

Fig. 1.4: Example multitone waveform in the time domain. The number of tones is 2, 4, and 8. Blue colored waveform is the multitone waveform and the gray colored waveform is the continuous wave. As increasing the number of tones, the peak amplitude increases to $\sqrt{N}$ times larger than the continuous waveform.

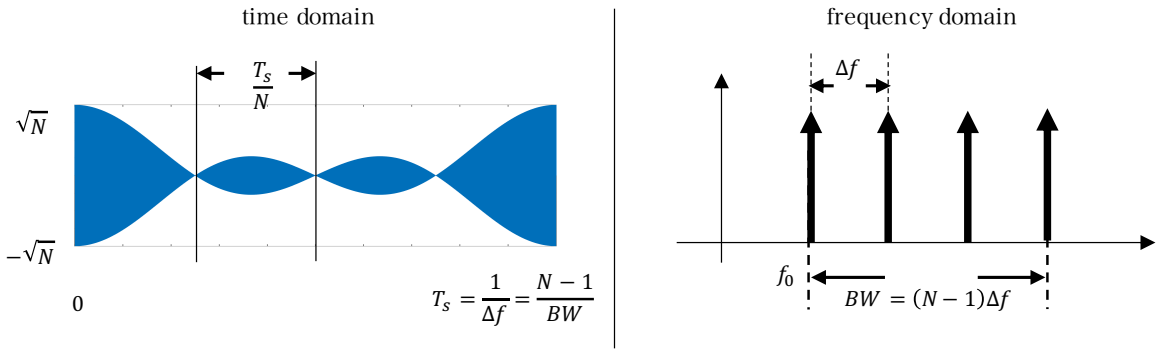

Fig. 1.5: Multitone waveform in the time domain vs in the frequency domain. Left hand side of the waveform is time domain multitone waveform and the right hand side shows the frequency spectrum of the corresponding multitone waveform.

1.1.4 Multitone Waveform Descriptions and Related Works

Multitone Waveform Characterizations

The multitone waveforms are made by the summations of the tones whose carrier frequencies are slightly different from each other. The designed waveforms can be expressed as follows;

$$X(t) = \mathrm{Re}\left\{ \sum_{m=0}^{N-1} a_m \exp(2\pi(f_c + \Delta f_m)t) \right\}, \tag{1.1}$$

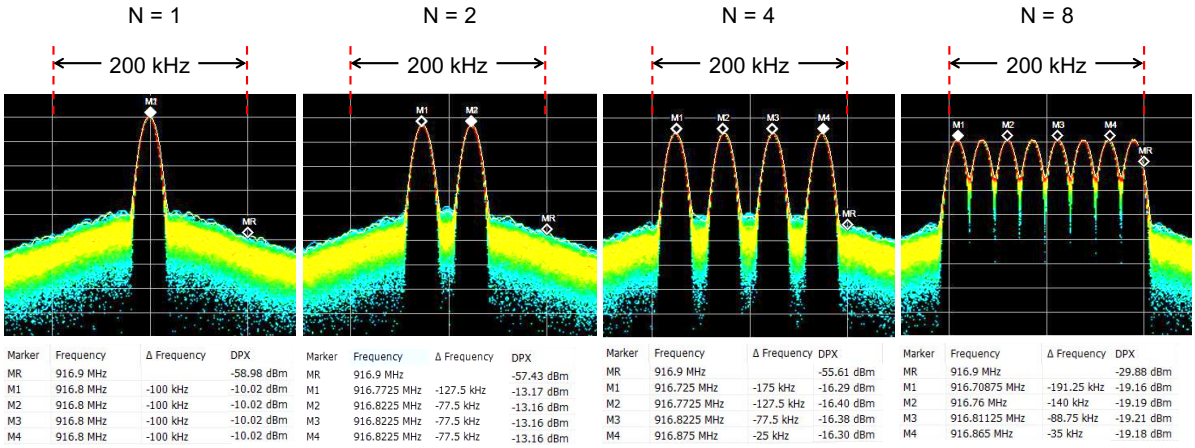

Marker	Frequency	Δ Frequency	DPX
MR	916.9 MHz		-58.98 dBm
M1	916.8 MHz	-100 kHz	-10.02 dBm
M2	916.8 MHz	-100 kHz	-10.02 dBm
M3	916.8 MHz	-100 kHz	-10.02 dBm
M4	916.8 MHz	-100 kHz	-10.02 dBm

Marker	Frequency	Δ Frequency	DPX
MR	916.9 MHz		-57.43 dBm
M1	916.7725 MHz	-127.5 kHz	-13.17 dBm
M2	916.8225 MHz	-77.5 kHz	-13.16 dBm
M3	916.8225 MHz	-77.5 kHz	-13.16 dBm
M4	916.8225 MHz	-77.5 kHz	-13.16 dBm

Marker	Frequency	Δ Frequency	DPX
MR	916.9 MHz		-55.61 dBm
M1	916.725 MHz	-175 kHz	-16.29 dBm
M2	916.7725 MHz	-127.5 kHz	-16.40 dBm
M3	916.8225 MHz	-77.5 kHz	-16.38 dBm
M4	916.875 MHz	-25 kHz	-16.30 dBm

Marker	Frequency	Δ Frequency	DPX
MR	916.9 MHz		-29.88 dBm
M1	916.70875 MHz	-191.25 kHz	-19.16 dBm
M2	916.76 MHz	-140 kHz	-19.19 dBm
M3	916.81125 MHz	-88.75 kHz	-19.21 dBm
M4	916.865 MHz	-35 kHz	-19.18 dBm

Fig. 1.6: Example Multitone waveforms in the frequency domain that are captured by a spectrum analyzer. The number of tones is 1, 2, 4, and 8. Total bandwidth is 200 kHz and the total power is set to −10 dBm. Increasing the number of tones by 2 times results in having 3 dB smaller power in each tone.

where X(t) is the time domain designed waveform, N is the number of tones, a_m is the amplitude of the mth tone, f_c is the carrier frequency, and Δf_m is the frequency spacing of the mth tone from the 0th tone. When the tones are evenly distributed in the frequency domain, Δf_m becomes $m \times \Delta f$, where Δf is the spacing between the adjacent tones. In order to set the total power to be the same for any number of tones, the amplitudes of the waveform must be normalized. As an example, when each tone has the same amplitude, a_m becomes $1/N$. The example time domain multitone waveforms of $N = 2$, 4, and 8 are shown in Fig. 1.4. The blue colored waveforms for each figure corresponds to the multitone waveforms and grey box corresponds to the single tone as a reference. When the frequency spacings are set to Δf, the period becomes $1/\Delta f$. This period can be determined based on the smallest spacing between neighboring tones. Also, the relationship between the time domain and the frequency domain of the multitone waveforms is shown in Fig. 1.5, where the number of tones is 4, but the notation is generalized to N. The total bandwidth BW can be expressed as $(N-1)\Delta f$ as the number of spacings is $N-1$. In the time domain, the nodes are coming at every T_s/N, where $T_s = 1/\Delta f$. The characteristic of this waveform is that the peak amplitude becomes $\sqrt{N}$ times larger than the single tone, which results in having a higher PAPR. Also, the multitone

waveforms of $N = 1$, $N = 2$, $N = 4$, and $N = 8$ that are captured by a real time spectrum analyzer (RSA306) is shown in Fig. 1.6. The spacing for each tone is that 100 kHz, 50 kHz, and 25 kHz for $N = 2$, $N = 4$, and $N = 8$ respectively. When increasing the tones by 2 times, the power of each tone decreases by 3 dB. The center frequency is set to 916.8 MHz, which is one of the channel band that has been conformed to the RFID standard in Japan (ARIB STD-T106) [76, 77, 78]. Along with 916.8 MHz, 918 MHz, 919.2 MHz, and 3 consecutive bands (920.4 MHz, 920.6 MHz, and 920.8 MHz) are allowed to transmit 1 W transmit power. Under this restrictions, the total transmit waveform bandwidth is 200 kHz, 400 kHz, or 600 kHz [76, 77, 78].

Research Trends

These waveforms have been firstly introduced in the context of microwave power transfer by M. S. Trotter *et al* as power optimized waveforms (POWs) [79] where they showed that the minimum power that the tag can be turned on using POWs decreased by 1.9 dB compared with continuous wave when the number of tones are added up to 8. From then on, enormous contributions in terms of designing waveforms have been conducted. Aside from multitone based waveforms, various waveforms have been investigated in terms of having higher PAPR values, such as orthogonal frequency division multiplexing (OFDM) signal, chaotic signal, pulse width modulation (PWM) signals [80, 81, 82]. It has shown that chaotic wave has got higher peat to average power ratio (PAPR) generation [80, 81]. However, one of the problems for these waveforms is that it is challenging to design the specific waveforms that can yield better efficiencies due to the fact that the waveforms are needed to be consider various parameters such as channel distortion while traversing in the air, transceivers' nonlinear effect not just at receiver rectifier, but also amplifier at the transmitters, antennas, matching circuit and so forth. In addition, most of the studies have been conducted experimental and simulation verification when the load is optimal. However, when looked at the recent IoT prototypes the load is not always optimal. Usually, these devices embed DC–DC converters after the rectifiers and the DC–DC converters are supposed to set rectifier load to be optimal. However, when it comes to low power operation where the rectified voltage is too small for DC–DC

converters to work continuously, they fail to set the rectifier load to be optimal. Therefore, designing waveforms when the rectifier load does not always optimal should be considered as well. For these reasons, vast majorities of the works have been investigated using multitone based waveforms. By using multitone waveforms,

Optimal waveforms for multitone based signals have long been sought in the past years, analyzing performance through circuit simulation, measurement, or modeling analytically [83, 84, 85, 86, 87, 88]. The research trends in terms of waveform optimizations have three folds; power allocations to each of the tones, bandwidth effects, and voltage transitions in a rectifiers. The researches related to the first content have discussed how to allocate the power to each tones in the waveforms under the conditions with wireless channels. The frequency selectivity in wireless channels causes the waveform distortions, so the proper power allocation should be taken into consideration. In addition, the frequency dependencies also have effects on the waveforms inside the receiver circuit since these circuits have high Q factor elements that prevents the widespread tones in the frequency domain to enter into the circuit elements. This comes into the second contents in that the what how the bandwidths are required to be when considering the circuit conditions. Lastly, there has been a lot of researches in terms of interpreting the voltages inside the circuit. Since there are multiple tones in a multitone waveforms, the voltage transitions are very challenging when considering the nonlinear effects.

In [84], time domain analysis has been conducted. Based on the conditions between the incident waveforms and closed-form equations of the diode, the authors determined the applied voltage across the diodes into three states. However, since the voltage transitions are made without considering the nonlinear effects, the efficiency performances are poor when the incident power is small. Frequency domain analysis has also conducted in such a way that receiver circuit has modeled as transfer functions [83], which becomes one of the mile stones for multitone waveforms that the amplitudes and phases are needs to be the same amount in order to have better performances. The difficulties of the modeling of voltage transition inside the receiver circuit is that the existences of the nonlinear elements, which results in having the same variables at both sides of the equations. To deal with this problem, approximation methods have been investigated, where the Taylor expansions have been conducted to the volt-

ages across the diodes [86]. In addition, the authors reveal that the optimal waveforms were obtained by applying the geometric programming methods in terms of having better power conversion efficiencies for the use of the multitone waveforms.

Furthermore, the same group achieved the optimal transmitting waveforms under the conditions where the frequency selectivity has existed. The results have claimed that for the fast fading channels, the multitone waveforms whose tones are evenly distributed in the frequency domain or the single tone becomes the best performances. On the other hand, when the channel has frequency selectivity the power allocation needs to be so that more power should be allocated to the tones whose frequency responses are good [86, 87, 88]. However one of the problems reside in this method is that it is required to calculate channel state information (CSIs), which is an expensive process for battery-less devices to conduct.

Applications: The application of multitone waveforms can be localization, power harvest to in-body sensors or farther places, and increase the read range of the wake-up sensors [89, 90, 91, 92, 93, 94]. Especially in the biomedical field, the multitone waveforms have been applied for the use of the electrical impedance spectroscopy (EIS) which is one of the methods for inspecting the characterization of the target structure, level of the batteries, and so forth from the spectrum of the reflected waveforms from the source [95, 96, 97]. Aside from that, the waveform designs are desired as a means for localizing in-body sensors so that the backscatter tag avoids the interference that otherwise causes the transmitter side to read the reflected signals from the in-body sensor tag [92]. Biomedical field does not the only field to be applied. In terms of increasing the read range of RFID tags, multitone waveforms have been investigated [91]. Also in [89], waveforms have been tuned for the wake-up receiver. Recent years have seen the use of multitone waveforms in order to achieve SWIPT [98, 90, 67, 66, 65]. In the SWIPT concept, multitone signals are sent as a usual manner to deliver power; however, the trick is that waveforms are modulated by changing frequency spacing, or PAPR ratio so that at the receiver, it is possible to acquire information based on the outputs produced by the nonlinear elements [99, 66, 68, 100, 101].

1.2 Research Challenges for Powering Battery-less Devices

The first challenge for the recent battery-less device is that the operating range of the devices is very small. At present, granted that transmit power can be approximately 4 W equivalent isotropically radiated power (EIRP), and that the antenna gain of the receiver device is at most approximately 7 dBi. In order to receive more than 100 μW of power, the devices needs to be placed closer than 12 m away from the sources. Although recently, there exists the movement for easing the regulation with regard to transmit power, the operation range still be suffered. Therefore, it is required to maximizing the ranges of which the battery-less devices can be operated, and designing waveforms are noteworthy approaches to meat these requirements. There are two main methods to be achieved: increasing the power conversion efficiency and increasing the reception sensitivity. The former is how the power received during operation can be received with high efficiency, and the latter is the key to delivering the voltage necessary for the device to recover from a power-off state (cold start). More specifically, PCEs are measured in terms of how much power can be delivered to the load. If the more power can be delivered to the system, the system can keep working even when the transmitter and the receiver is away from each other. On the other hand, the sensitivities are measured in terms of knowing how much power is required for the system to start their process. Since most of the case, the system embeds the boost converter, system starts working their process when the boost converter starts working. Most of the time, a boost converter has the threshold voltage to start its operation, so in such case, it is important to apply the voltage with smaller input power. Goal of obtaining higher voltage and delivering power is different in that the former can be realized by using very high impedance at the load whereas for the latter case, the relatively low resistance the system can obtain more power (roughly voltage times current).

The next step is to establish a method for transferring information and power. So far, how to send signals with low power consumption has been investigated with respect to the uplink communication technology for IoT devices such as backscatter communications. However, few efforts have been made for signal reception. Most of the studies assume to communicate using a simple signal system such as ASK is used. One of the problem of these methods is that

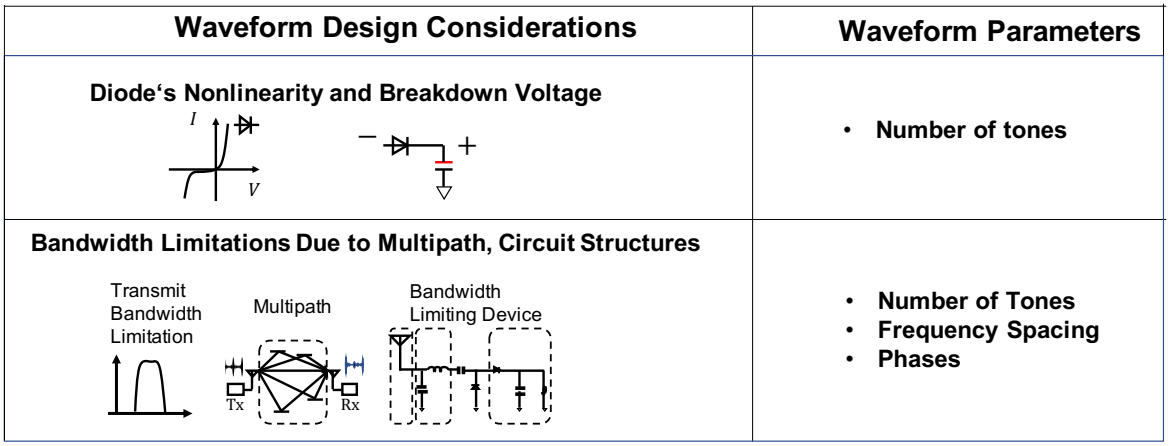

Fig. 1.7: Design considerations for multitone waveforms. The left hand side of the figure shows the challenges encountered when designing waveforms, and the right hand side of the figure shows the parameters to be concerned when designing the waveforms.

the power supply capacity is reduced during signal reception, which becomes crucial matter for battery-less devices. Therefore, it is necessary to design waveforms that can transmit information and power simultaneously and receive continuous power supply even when the IoT device is receiving information. For these reasons, it is important to design waveforms that can transfer both information and power simultaneously whose waveforms yields better performances (PCE or sensitivity). However, designing such waveforms does not simple since there are multiple factors to be considered.

1.2.1 Waveform Design Challenges

When designing multitone waveforms for RF harvesting to the devices, it is required to consider the effects of diode nonlinearity and the bandwidth tradeoffs. The effects to be considered and the waveform parameter considerations are listed in Fig. 1.7.

Diodes' Nonlinearities and Breakdown Voltage Limitations

Increasing the number of tones leads to applying a higher voltage to the diodes, which results in having a larger output current, but excessive voltage over the breakdown voltage of the

diode results in performance degradation. Thus, a suitable number of tones needs to be selected. In terms of bandwidth tradeoffs, there are mainly two kinds of effects to be considered, as discussed in the introduction; over the air effect and internal circuit effects.

Over the Air Effect on Bandwidth

While the transmitted waveforms are traversing in the air, they would get reflections around the surrounding objects, which is called multipath effect. Because these reflected waveforms are mixed at the receiver side, the received waveforms are distorted. If the bandwidth of the waveforms is large, the distortions will be more severe. In particular, the different arrival times of signals could cause the phase changes between them by $2\pi f_{\mathrm{BW}} T_{\mathrm{d}}$, where f_{BW} is a frequency difference of assigned bandwidth, and T_{d} is the delay based on multipath. Typically, T_{d} is 1 μs for the outside condition and dozens of nano seconds for the inside conditions, but these parameters are primarily determined by the surrounding environment [102, 103]. When the bandwidth is large this phase difference also becomes large, which results in a misalignment between the tones, and this severely deteriorates the quality to deliver power in a multipath scenario [83, 102]. The coherent bandwidth which is determined by $\frac{1}{2T_{\mathrm{d}}}$ is one of the indicators that can regard the wireless channel as flat [102]. Typically, the coherent bandwidth becomes 500 kHz in outdoor environment and 50 MHz in the indoor environment. [102, 103]. In addition, assigning large bandwidth occupies a lot of available bandwidth, which could cause interference. For example, in the UHF band which is one of the ISM band, total bandwidth could be assigned at a maximum of 26 MHz. The transmitted signal that has bandwidth close to 26 MHz might interfere with other signals from different signals within the same band. Thus, the bandwidth assignment should be small enough to suppress this effect.

Internal Circuit Effect

For the internal circuit effect, because the receiver devices are supposed to have high Q factors, antennas and matching networks are all meant to be narrowband. For this reason, the bandwidth of the multitone waveforms needs to be small. In contrast, the diode's internal resistance and the storage capacitor forms a low-pass filter (LPF). Therefore, if the frequency

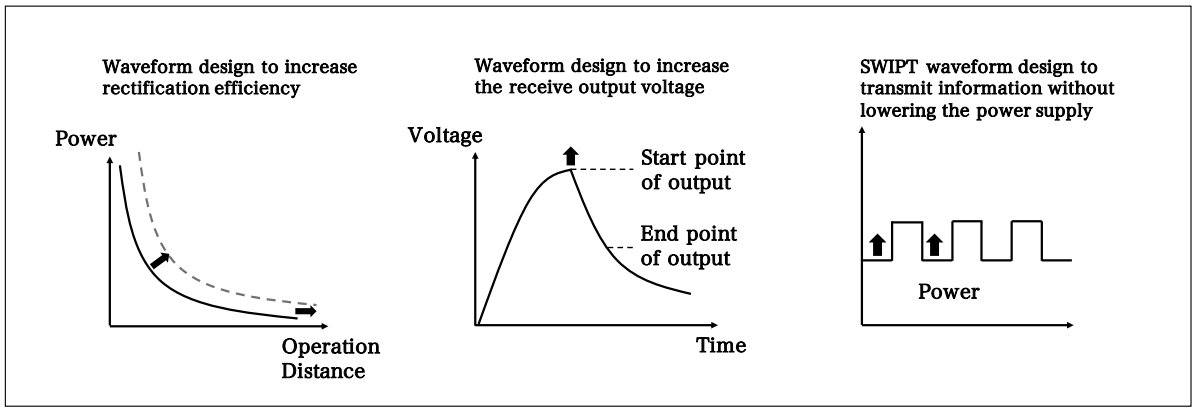

Fig. 1.8: Waveform design considerations. On the left, designing multitone waveform properly results in having better PCEs and longer operational distances. In the middle of the figure, proper multitone waveforms results in having higher voltage acquisitions and improving the sensitivity performances. On the right, designing SWIPT waveform using multitone waveforms results in having better WPT performances while sending information.

spacing is small, the LPF allows the alternative current (AC) component to go through the load resistor. This results in deteriorating the system efficiency but obtaining a higher peak voltage at the load [20]. In addition, total bandwidth for transmission is usually determined by the government. For example, in the UHF band, FCC limits the available bandwidth to be at most 26 MHz. Because multitone waveforms utilize multiple tones, the frequency spacings and the number of tones need to be carefully considered under the bandwidth effect.

1.2.2 Thesis Goal of this thesis

The research goal for this thesis is to design the multitone waveforms that can transmit both power and information simultaneously so that the design waveforms can improve operation range of the battery-less devices, or increase the sensitivity read ranges as shown in Fig. 1.8. Especially, for my thesis, I am interested in designing multitone waveforms with narrow bandwidth, since the sub GHz band requires limited bandwidth (under 1 MHz) for transmission. Such narrowband multitone waveforms have not been studied thoroughly in other researches to best of our knowledge. In order to properly design multitone waveforms, it is required to characterize the performances of the waveforms for different rectifier parameters under lim-

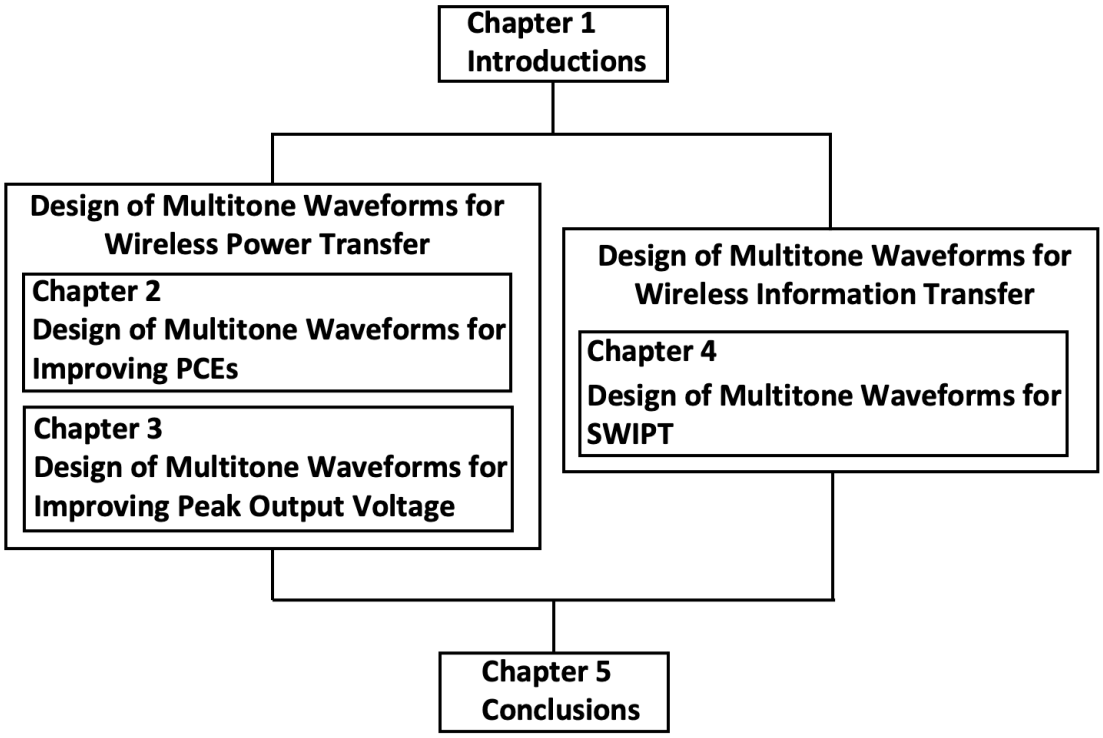

Fig. 1.9: Chapter relations.

ited bandwidth conditions. Therefore, in this thesis I have conducted investigations of the performance characterizations of the narrowband multitone waveforms in terms of PCEs or higher peak output voltage through experiments. Prior to the experiments, based on the excising studies with regard to multitone waveforms, I assume that the rectifier performance can be determined by the number of tones, frequency spacing between the tones, the storage capacitances and the load resistances when considering the bandwidth tradeoffs. The input power may also affect the performance, but for simplicity, I decide to fix them to -10 dBm. Then, I formulate the design formula for improving better PCEs or having higher peak output voltage according to the rectifier parameters. Because analytically deriving them requires nonlinear behaviors, it is extremely challenging. Thus, I rely on the experiments for characterizing the narrowband multitone waveforms. Finally, I design the multitone SWIPT waveforms that can transmit power and information simultaneously. The design waveform utilizes the nature of

nonlinear devices, thereby generating varieties of output by shifting the tone configurations of the waveforms. These varieties of outputs can be classified in the groups depending on the configurations of the tones separations. I reveal such relationships and verified with simulation and experiments. Based on this, I proposed the modulation method to send information that is superimposed on the multitone waveforms. Overall, I propose the waveform designs for WPT as well as SWIPT. The former is utilized when the devices needs to be harvested and the latter is utilized for sending information.

Based on the above, this thesis is organized as follows. Chapter 2 discuss the waveform design for improving PCEs depending on the rectifier characteristics. Element by element experiments are conducted to see which circuit component has the dominant effects on multitone WPT. Then the design instructions for improving PCEs are introduced. Chapter 3 discuss the waveform design for improving peak voltage acquisitions. Similar to the previous chapter, the waveform characteristics are investigated in order to have higher peak voltages. Also the characteristic differences between the waveform design for higher PCEs and higher peak voltage acquisitions are discussed. Finally, the sensitivity analyses are experimented using real IoT devices to see the impact of using multitone waveforms and pros and cons of using them. Chapter 4 introduces the waveform design for sending both power and information simultaneously by using frequency shifted multitone waveforms. Prior to the proposed waveform design, the mechanism of how frequency shifted waveforms can achieve varieties of outputs through nonlinear devices. The manufactured SWIPT circuits are utilized for the verification of the proposed method. Finally, Chapter 5 concludes my thesis including the summary as well as the future works of this topic. The waveform optimization methods for the future works are introduced for giving insights for the future works.

Chapter 2

Multitone Waveform Design for Improving Power Conversion Efficiencies

2.1 Introduction

Recently, a growing number of devices have been connected to wireless networks in order to make the quality of lives better. By contrast, these devices generally embed batteries for their operation; thus, they are bulky and heavy, and consequently, incompatible with the circuits, which are relatively small. Eliminating batteries would make these devices light-weight and ubiquitous, and thus, maintenance-free. This elimination could potentially be realized via wireless via wireless power transfer. Particularly in an outdoor environment, microwave power transfer is utilized to have wide area coverage. However, unlike battery enabled devices where wake-up modules could sense incoming signals with high sensitivity, battery-free

Table 2.1: Related Works of Bandwidth Effect on Microwave Waveforms

work	carrier frequency	type of effect	noise effect	modeling based on	waveform type	PCE (input power)	tested devices
[86]	5.18 GHz	Over the air effect	No	Analytical / Measurement	Multitone	30% (-20 dBm)	rectifier
[104]	1.6 GHz	Internal circuit effective	No	Measurement	Multitone	39% (-10 dBm)	rectifier
[105]	2.45 GHz	Internal circuit effective	No	Analytical / Measurement	Pulse Width Modulated	50–70% (0 dBm)	rectifier
This work	915 MHz	Internal circuit effective	Yes	Measurement	Multitone	39% (-10 dBm)	rectifier and receiver devices

devices suffer from limited operation range. Increasing transmit power could be one of the solutions; however, the transmit power is regulated by the government [106]. Therefore, transmitting signals beyond the limit would not be appropriate.

Multitone waveforms, also known as power-optimized waveforms (POWs), can be considered as they exhibit the potential to overcome this problem [107, 79, 108]. They comprise multiple sine waves that are summed with each other and generate a high peak to average power ratio (PAPR) [109, 110, 111, 112]. This technique boosts the efficiency of a diode-based rectifier due to the nonlinear behavior of the diode without increasing the transmit power [113, 20, 21]. Aside from multitone based waveforms, various waveforms have been investigated, such as orthogonal frequency division multiplexing (OFDM) signal, chaotic signal, and pulse-width modulation (PWM) signals [80, 81, 82, 114, 115, 105]. In this chapter, I focus on multitone based waveforms.

Optimal waveforms for multitone based signals have been sought in the past years, analyzing performance through circuit simulation, measurement, or modeling analytically [83, 84, 85, 86, 87, 88]. In [84], closed-form equations of the diode modeling have been presented so that the voltage that is applied to the diode has been characterized as three states based on the behaviors of the diode and the waveform. In [86, 87, 88], both transmitter and receiver sides were modeled, and waveforms have been optimized based on the channel state information (CSI). In its implementation, the transmitter and receiver first communicate with each other using OFDM to obtain CSI and based on that, the waveforms are optimized.

While the advantages of using multitone waveforms have been proven in theory, some papers have also addressed their limitations. In [116], the limitation of using multitone waveforms have been investigated for the case of voltage-doubler rectifiers. The claim was that

during the negative half cycle of the waveforms, the voltage did not seem to be stored in the clamp capacitor, resulting in a relatively small peak voltage at the load, and PCE performance is negatively affected [116]. However, our investigations show that depending on the load resistance, the PCE performance can be improved over the single tone [117]. Thus, it is important to design proper multitone waveforms depending on the rectifier properties.

When designing multitone waveforms, it is also important to consider the bandwidth of the waveforms. There are two types of effects towards performance with regard to bandwidths of waveforms: over-the-air effect and internal circuit effects. The first is primarily due to waveform distortions resulting from multipath [86, 56, 118]. In [86], algorithms to optimize waveforms have been proposed to account for multipath effects. It has concluded that the proposed algorithm allocates more power to subcarriers whose channels are better than others, which is similar to the idea of a water-filling algorithm. In [56, 118], further investigations have been conducted to meet the requirements of such scenarios using large-scale multiple-transmit antennas or backscatter communication.

For the second case, narrowband circuitry systems for radio frequency (RF) energy harvesting (an antenna, a matching circuit, or RC filter of rectifier) cause a frequency selectivity, which degrades the system performance as some frequency band could not pass through the circuit system [119, 104]. In terms of bandwidth effects on the receiver circuit, there is a trade-off between the frequency spacing of each tone and cut-off RC filter of a rectifier at 1.6 GHz [119, 104]. These authors argue that setting an index of frequency spacing over cut-off frequency to be 100 would be suitable in terms of the power conversion efficiency (PCE).

Although bandwidth effects on the performances have been discussed recently, most of the researches have dealt with relatively large bandwidth assignment (over 1 MHz), which may not be beneficial at ultra-high frequency band (UHF) [87, 104]. This is because allocating such bandwidth causes signal distortions resulting from frequency selectivity, particularly in multipath scenarios [119]. In addition, bandwidth occupation causes severe interference against other wireless communication systems that run in the same frequency band.

This chapter is extended from the preliminary results obtained in [117] with the follow-

ing contributions. I characterize the PCE and the peak output voltage acquisition based on the configurations of rectifiers through experiments. Based on them, I introduce the design instructions of multitone waveforms to improve the PCEs or the sensitivities at UHF. Further, I characterize the sensitivity performances of two types of receiver devices with an embedded boost converter and discuss analyses based on the waveform instruction. The key findings are summarized as follows;

- There exist specific points (saturation points) for frequency spacing that multitone waveforms have to assign to improve the PCEs, and the saturation points can be controlled or strongly affected by the value of storage capacitance (C_{L}) at the receiver.
- In terms of having better PCEs, the multitone waveform has to assign more frequency spacing than the saturation points of PCEs. I characterize how much spacing needs to be assigned in order to improve the PCE performances depending on the rectifier designs.

The comparison between my work and the related researches are listed in Table 2.1. In contrast to [104], I consider narrow bandwidth because the industry, science, and medical (ISM) band can only have a total bandwidth of 26 MHz, and less than 1 MHz when considering transmitting information as well. The bandwidth effect smaller than 1 MHz has not been considered in the paper. In addition I have tested not only rectifiers but also the receiver devices that can be obtained commercially. I also tested the wireless transmission under noise effect.

The remainder of this chapter is structured as follows. In Section 2.2, I describe the behaviors of the multitone waveforms at the transmitter and receiver side. Then, I analyze the waveform characterizations of the multitone waveforms and suggest the waveform design to obtain higher efficiency of the receiver device based on the rectifiers' parameters in Section 2.3. Finally, I will summarize this chapter in Section 2.4.

2.2 System Model

Based on the discussions from the existing papers, I set the condition for designing multitone waveforms so that the tones are equally distributed in the frequency domain [83, 120, 104].

Also, because I aim to design waveform to be suitable for narrow bandwidth, the wireless channel effect can be regarded as flat. In such a case, the amplitude and phase of each tone needs to be the same for having better performances [86, 83].

2.2.1 Waveform Generation

Let us assume that the multitone based waveform is modeled as a summation of sine waves of size N whose bandwidth is determined by BW. The waveform is first generated as a baseband signal, expressed as;

$$x_{\mathrm{b}}(t) = \sum_{m=0}^{N-1} S e^{j2\pi \Delta f m t}, \tag{2.1}$$

where $S = \sqrt{P_{\mathrm{out}}/N}$ represents a normalized amplitude of output power (P_{out}) at a transmitter side to maintain the same average power, and $\Delta f = BW/(N-1)$ is a frequency spacing between the tones. An mth tone could be expressed as, $x_{\mathrm{b}_m}(t) = S e^{j2\pi \Delta f m t}$, where $m = 0, 1, ..., N-1$. Then, the passband signal is generated by shifting its frequency in such a way that the center frequency is fixed to f_{c}, which is expressed as follows;

$$x(t) = \Re\Big\{ \sum_{m=0}^{N-1} x_{\mathrm{b}_m}(t) e^{j2\pi (f_{\mathrm{c}} - \frac{BW}{2})t} \Big\}. \tag{2.2}$$

PAPR can be employed to comprehend how high the signal power goes, based on average power. It can be expressed as;

$$\frac{\mathrm{Max}\Big\{x(t)^2\Big\}}{E\Big\{x(t)^2\Big\}}. \tag{2.3}$$

2.2.2 Receiver Side Behavior

A system model of the receiver circuit is presented in Fig. 2.1. First, a voltage is induced at the antenna port (v_{ant}), and then it goes through a matching circuit consisting of an inductor (L_{m}) and a capacitor (C_{m}). Thus, the signal is rectified. The rectifier circuit is composed of a clamp capacitor (C_{c}) and, two series diodes (D_1 and D_2). Finally, it is stored in the storage capacitor (C_{L}) with the load (R_{L}). Granted that the received power is determined by $P_{\mathrm{in}} = P_{\mathrm{out}} h$, where

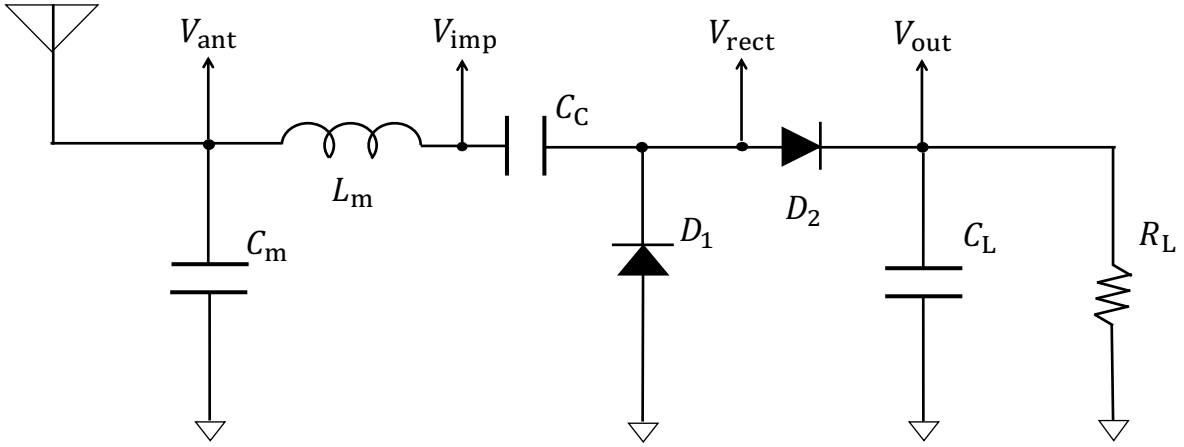

Fig. 2.1: System model of a voltage doubler type rectifier. It consists of a matching network (C_{m}, L_{m}), a voltage doubler rectifier (C_{c}, D_1, D_2), a storage capacitor (C_{L}), and a load resistor (R_{L}). In our experiment, a signal is injected through a signal generator.

h is an attenuation coefficient. If the impedance of the antenna and the matching network are the same, then the receiver circuit consumes P_{in} [121]. Therefore, $v_{\text{ant}}(t)$ can be expressed as;

$$v_{\text{ant}}(t) = \sum_{m=0}^{N-1} V_{\text{ant}} \cos(w_m t + \phi_m), \tag{2.4}$$

where $V_{\text{ant}} = \sqrt{\frac{P_{\text{in}} R_{\text{ant}}}{N}}$ is an amplitude of the induced voltage at the receiver's antenna, w_m is $2\pi(\Delta f m + f_{\text{c}} - BW/2)$, and ϕ_m is a phase rotation factor at the mth tones [86]. In addition, R_{ant} is the impedance of the antenna.

As discussed in the prior works, a matching network serves as a transformer. The voltage at an input of the matching network would be enhanced as the relatively high impedance of circuitry structure after the impedance matching is transformed to 50 Ω [116, 104]. Because the impedance of the rectifier changes depending on the voltage applied across the diode, the input impedance after the matching network also changes. Therefore, the voltage enhancement factor would not be the same all the time. This makes modeling hard to establish. After the impedance transformation, the signal is rectified.

Based on the discussions which relate to the voltage-doubler circuits, the voltage at the first stage of the rectifier ($v_{\text{rect}}(t)$), and the instantaneous output voltage at time t ($v_{\text{out}}(t)$) could

be expressed as follows [116];

$$C_{\mathrm{c}}\frac{\mathrm{d}(v_{\mathrm{imp}}(t)-v_{\mathrm{rect}}(t))}{\mathrm{d}t}=-I_{\mathrm{s}}\left\{\exp\left(\frac{-v_{\mathrm{rect}}(t)}{nV_{\mathrm{T}}}\right)-1\right\}, \tag{2.5}$$

$$C_{\mathrm{L}}\frac{\mathrm{d}v_{\mathrm{out}}(t)}{\mathrm{d}t}=I_{\mathrm{s}}\left\{\exp\left(\frac{v_{\mathrm{rect}}(t)-v_{\mathrm{out}}(t)}{nV_{\mathrm{T}}}\right)-1\right\}-\frac{v_{\mathrm{out}}(t)}{R_{\mathrm{L}}}. \tag{2.6}$$

Output voltage, $V_{\mathrm{out}}(t)$ which is the average voltage applied at a resistor or a capacitor could be expressed as follows;

$$V_{\mathrm{out}}=E\Big\{v_{\mathrm{out}}(t)\Big\}. \tag{2.7}$$

Overall, the PCE is obtained based on the following expressions;

$$PCE=\frac{V_{\mathrm{out}}^2}{R_{\mathrm{L}}}. \tag{2.8}$$

2.3 PCE Performance Analysis of Rectifier for Narrowband Multitone Signal

To see the effects of frequency spacing and the number of tones of the multitone waveforms on the performance of efficiencies, I conducted experiments using rectifiers. Most of the parameters of the rectifiers, including clamp capacitance (C_{c}), types of diodes, storage capacitance (C_{L}), and load resistance (R_{L}) were tested in order to see the characteristics against transmitting waveforms.

2.3.1 Experimental Setup

The experimental setup is shown in Fig. 2.2. I have conducted experiments under both wired and wireless conditions. In experiments under wire transmission, I connected a signal generator (SG) to a rectifier through a cable. For the case of experiments under wireless transmission, I connected antennas to both the SG and the tested rectifiers and they were separated for 50 cm away from each other in an anechoic chamber. Since the both antennas have antenna length of 16.4 cm, antenna distance away from 16.4 cm can be regarded as far field. Therefore,

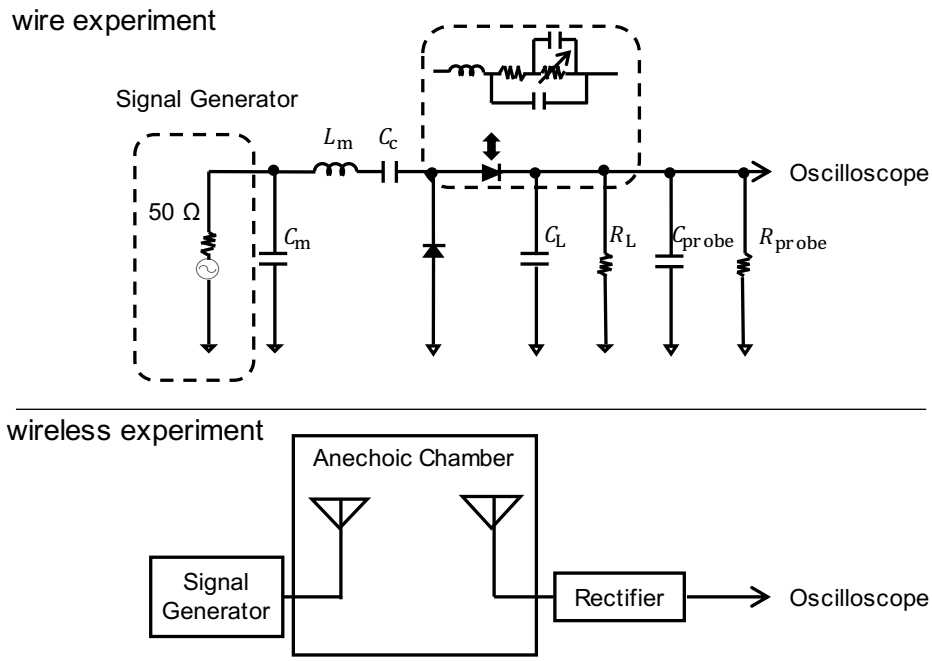

Fig. 2.2: Experimental setting for the wire transmission on the top and for the wireless transmission on the bottom.The waveforms are generated using a signal generator (SMBV100A) and transmitted through media. Various types of the diodes, storage capacitors, or load resistances to see how these parameters and designed waveforms affect PCEs.

this experiment can be regarded as far field transmission. To measure the induced voltage at the rectifiers, I used an oscilloscope. The input impedance from the probe to the oscilloscope consisted of R_{probe} and C_{probe}. I monitored the performance of PCEs by changing the conditions of multitone waveforms excited from the SG. All the instruments were connected to a monitor computer through LAN cables and all the experiments have conducted through automated processes. In the following section, I explain the experimental setups in detail. All the parameters for the experiments are listed in Table 2.2.

Transmit Signal Generation

For signal transmission, I used a Rohde & Schwarzs SMBV100A vector signal generator (SG). Multitone waveforms were excited using arbitrary (ARB) waveform mode in the instru-

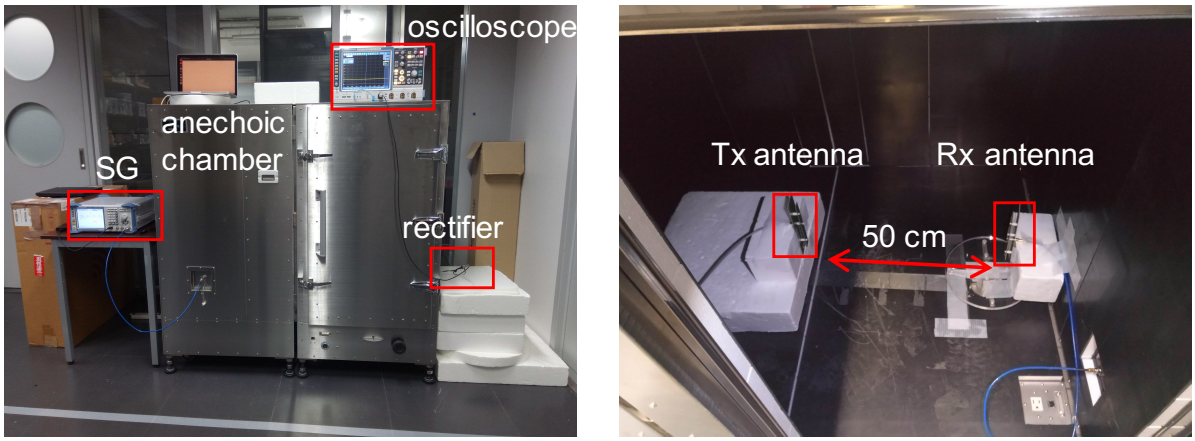

Fig. 2.3: Actual experimental setup for wireless transmission. (a). overview and (b). inside the anechoic chamber.

ment. waveforms were generated by setting the multicarrier tab in the ARB subsystem.The number of tones was 1, 2, 4, 8, and 16, and the frequency spacing was varied from 1 kHz up to 5 MHz. The center frequency was set to 915 MHz. In addition, before start experiment, the input power is measured by power meter (R&S NRP-Z Power Sensor) so that the input power is maintained with different number of tones or different frequency spacing.

Rectifier Design

I tested voltage-doubler type rectifiers. Diodes to be used were mostly SMS7630-005LF (Skyworks), but I also tested PCC110 (Powercast) and HSMS285C (Avego) in order to see the performance differences when using different diodes. C_L was 100 pF, 1 nF, or 10 nF, and the resistance of R_L was varied from 10 kΩ to 1 MΩ. The manufactured rectifiers were all follow the same circuit layout as shown in Fig. 2.4 (a) and one of the manufactured rectifier for the experiments is shown in Fig. 2.4 (b).

For matching networks, an input impedance of a rectifier was tuned to 50 Ω by trial and error. The input power was set to −10 dBm when I perform impedance matching. I matched the network by observing the S11 using Rohde & Schwarzs vector network analyzer (ZNB20).

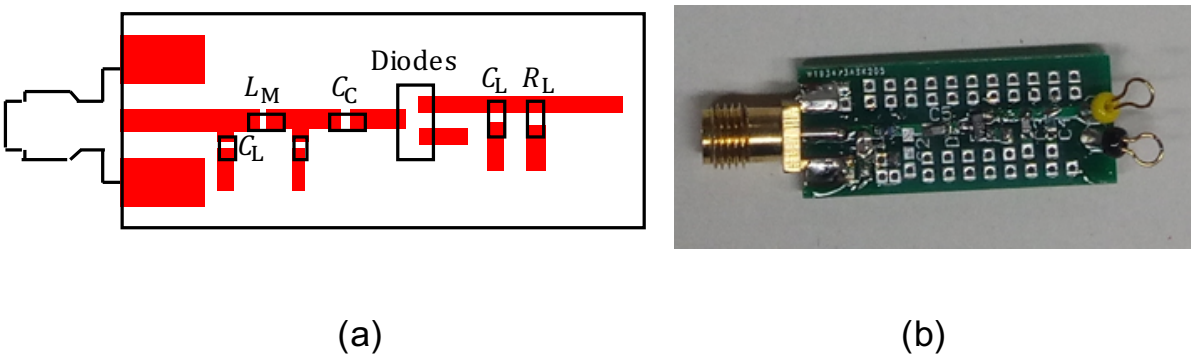

Fig. 2.4: (a). Layout of the rectifier for the experiment. All the tested rectifiers are implemented using this layout. (b). One of the manufactured circuit.

Note that here I produced different rectifiers according to the value of the R_L and C_L and for each rectifier, I matched the impedance matching network. The tested S11 parameters of one of the manufactured rectifiers (C_L of 100 pF and R_L of 100 kΩ) was shown in Fig. 2.5. The result showed that manufactured rectifier achieved up to −23 dB return loss, and at least −10 dB return loss for the tested bandwidth (900 MHz–930 MHz) at −10 dBm input power. In addition, even when the input power ranged S11 maintained −10 dB return loss for varieties of tested frequency with different input powers. Note that at each input power, I calibrated the VNA.

Voltage Measurements

Rectified voltages were measured using Rohde & Schwarzs RTO2014 oscilloscope. I obtained the mean value of the voltages from RTO2014 and calculated the PCE using Equation (2.8). The input impedance of the probe was 10 MΩ and 9.5 pF.

2.3.2 Measurement Result

The measurement results of the PCE performance of the rectifiers when using multitone waveforms are shown in Figs. 2.6 - 2.14. Based on the results, I summarized the results as the following;

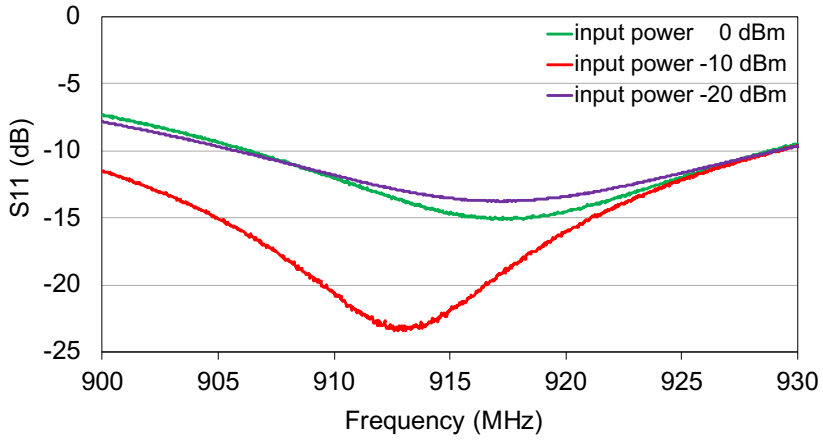

Fig. 2.5: Measured S parameters (S11) using VNA. The tested rectifier had parameter C_{L} of 100pF and R_{L} of 100kΩ

Table 2.2: Measurement parameters

Variable	Values
Number of tones (N)	1, 2, 4, 8, and 16
Center frequency	915 MHz
Transmit power	from -30 to 0 dBm
Diodes	SMS7630-005LF, PCC110, HSMS285C
Storage Capacitance (C_L)	100 pF, 1 nF, 10 nF, 100 nF
Load Resistance (R_L)	1 kΩ – 1 MΩ
Frequency spacing (Δf)	from 1 kHz to 5 MHz
Device placement (wire transmission)	On the table in the shield room
Device placement (wireless transmission)	On the table in the anechoic chamber

1. The PCE increases according to the frequency spacing, and it does not increase beyond a certain point, which I call the saturation point.

2. The saturation points move in the frequency domain according to the C_{L}, R_{L}, and P_{in}, but C_{L} primarily dominates the behavior. Increasing the C_{L} can reduce the frequency

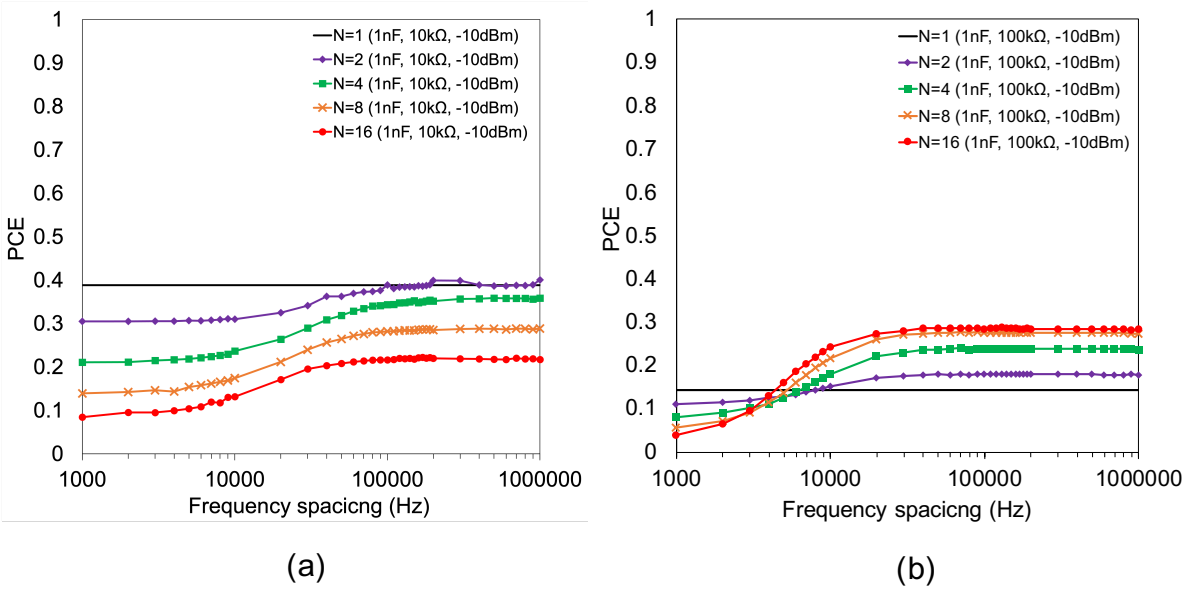

Fig. 2.6: PCE performances comparison against the different number of tones (1, 2, 4, 8, and 16) through wire transmission. The input power is set to −10 dBm. The tested rectifiers had parameters, (a). C_{L} of 1 nF and R_{L} of 10 kΩ, and (b). C_{L} of 1 nF and R_{L} of 100 kΩ.

spacing required to saturate the PCE performance.

3. The performance of PCE depends on the R_{L}; increasing R_{L} causes PCE to be smaller. However, when R_{L} is bigger, I see the advantage of using a large number of tones.

I discuss these closures in detail in the following sections.

PCE Characteristics against Load Resistance

I measured the PCEs of rectifiers with the different R_{L} in order to see the impact of frequency characterization, which is shown in Figs. 2.6 (a), (b). I tested rectifiers with the same capacitance 1 nF but different R_{L}s (10 kΩ and 100 kΩ). Based on these results, I determine two observations: there exists frequency selectivity for both tested rectifiers, and the PCE performance of multitone waveforms gives opposite characteristics depending on the value of R_{L}.

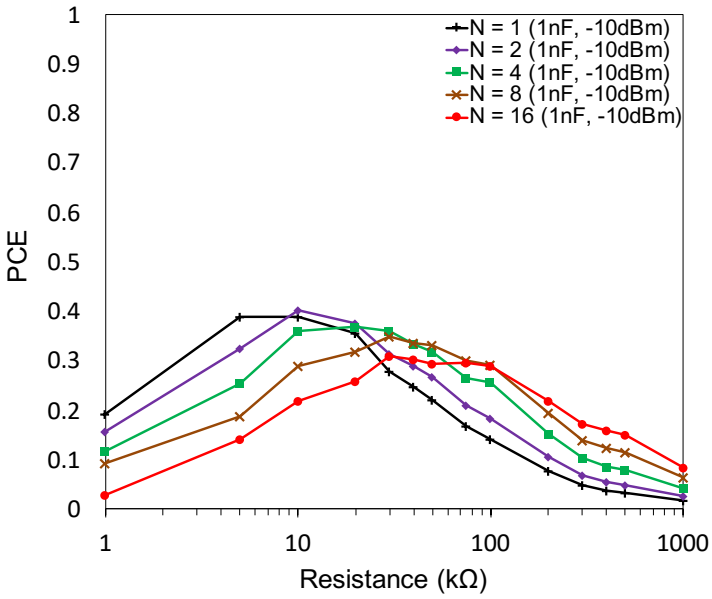

Fig. 2.7: PCE performance comparison versus the different number of tones (1, 2, 4, 8, and 16). I tested various rectifiers whose R_Ls were varied from 1 kΩ to 1 MΩ. C_L was set to 1 nF, and input power was set to −10 dBm.

As for the first observation, I find that assigning more frequency spacing gives better PCE performance for multitone waveforms. However, after a certain point, the PCE performance does not improve. I define this point as the saturation point. The saturation points occur at approximately 100 kHz for these results. I analyze these points in the following section.

Next, it is found that for the rectifier with low load-resistance, the PCEs using multitone signals are inferior to the continuous wave (CW), or single tone case ($N = 1$) as shown in Fig. 2.6 (a). In addition, increasing the number of tones deteriorates the PCEs. Therefore, in this case, using a single tone gives the best PCE performance. In contrast, if the rectifier has high load-resistance, the situation becomes the opposite. In this case, increasing the number of tones gives better performance in terms of PCEs, and multitone signals give better performance against a single tone, as shown in Fig. 2.6 (b). Therefore, when using multitone waveforms, rectifiers should embed higher load-resistances.

I also tested various rectifiers with different load-resistances to see whether the aforementioned contrasting characteristics occur. The results are shown in Fig. 2.7. The PCEs were

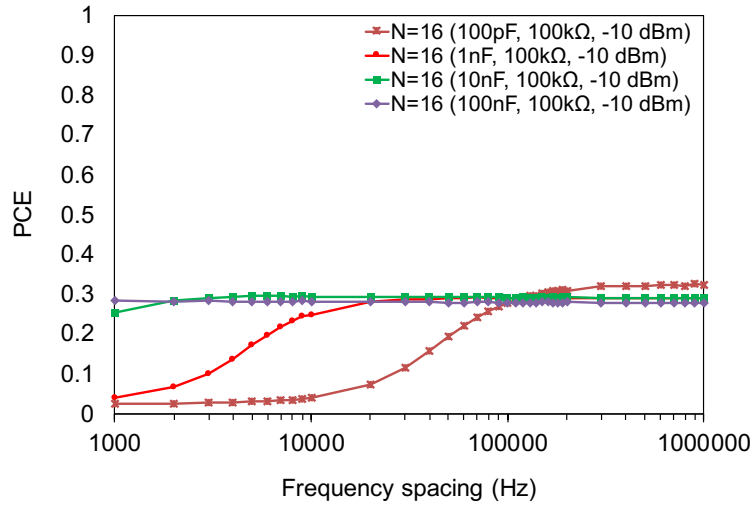

Fig. 2.8: PCE performances comparison against different capacitance (100 pF, 1 nF, 10 nF, and 100 nF). The number of tones was 16. R_L of tested rectifiers was the same (100 kΩ), and input power was set to −10 dBm.

taken from the saturated point (1 MHz), and the capacitance was 1 nF for these results. Input power P_{in} was set to −10 dBm. Based on the results, I find that there is a transition region where the highest PCE performances differ depending on the number of tones in the following manner. When R_L is smaller than around 10 kΩ, the PCE performance of a single tone is the highest. In contrast, when the R_L reaches above 10 kΩ, the performance of multitone waveforms becomes superior to the single tone. Within the transition region, during R_L = 10 kΩ − 100 kΩ, and as the R_L increases, the required number of tones that can yield the highest PCE increases. When R_L reaches more than 100 kΩ, the highest PCE is obtained when the number of tones is 16. During the transition region, the highest PCEs obtained for the number of tones is 2 from 10 kΩ to 20 kΩ, 4 from 20 kΩ to 40 kΩ, 8 from 40 kΩ to 100 kΩ, and 16 after 100 kΩ as shown in Table 2.3.

Frequency Spacing Characteristics against Storage Capacitance

Next, I tested rectifiers with different C_L to see how the saturation points correspond to this parameter. I compared the result with different capacitance 100 pF, 1 nF, 10 nF, and 100 nF. The load resistance was fixed to 100 kΩ. The measurement result is shown in Fig. 2.8. Based

on the result, the saturate points move depending on the capacitance. Moreover, when the value of C_L becomes 10 times, the saturate points become $1/10$ in the frequency domain. This means that by determining C_L, I am able to assign the amount of the frequency spacing. For example, if a rectifier embeds 100 pF storage capacitor, the frequency spacing of the multitone signal should assign more than 1 MHz in order to get maximum PCE, whereas when 10 nF is chosen for C_L, assigning 10 kHz for spacing is enough for multitone signals to obtain the best performance.

Frequency Spacing Characteristics against Load Resistance

I also tested the frequency spacing characteristics against different resistances. I compared with different load resistances: 10 kΩ, 100 kΩ, and 1 MΩ. C_L was fixed to 1 nF for this experiment, and the input power was -10 dBm. In addition, the number of tones was set to 16. The measurement result is shown in Fig. 2.9. I could not clearly find the tendency between the value of R_L versus frequency spacing except, the saturation points for the rectifier with 10 kΩ require more spacing than the other cases. One of the reasons is that when R_L is small the output voltage drops faster than the case when the R_L is high. This leads to requiring larger frequency spacing. I choose to set the saturation point to 100 kHz in order to agree with all the cases.

In terms of PCEs, the performance is the best when R_L is 100 kΩ. This is because the PCE of the waveform with 16 numbers of tones has its maximum at approximately 100kΩ as shown in Fig. 2.7.

Frequency Spacing Characteristics against Input Power Level

Further, I tested with different input power levels (0 dBm, -10 dBm, and -20 dBm) to see how it impacts on the frequency dependence. C_L and the load resistance of the tested rectifier were 1 nF and 100 kΩ. The measurement result is shown in Fig. 2.10. As it can be seen, when the input power increases, the required saturation points need more spacing. This is because when the power level increases, the internal resistance of the diode decreases due to the self-bias. Because this resistor and C_L form a low-pass filter (LPF), the cut-off frequency of

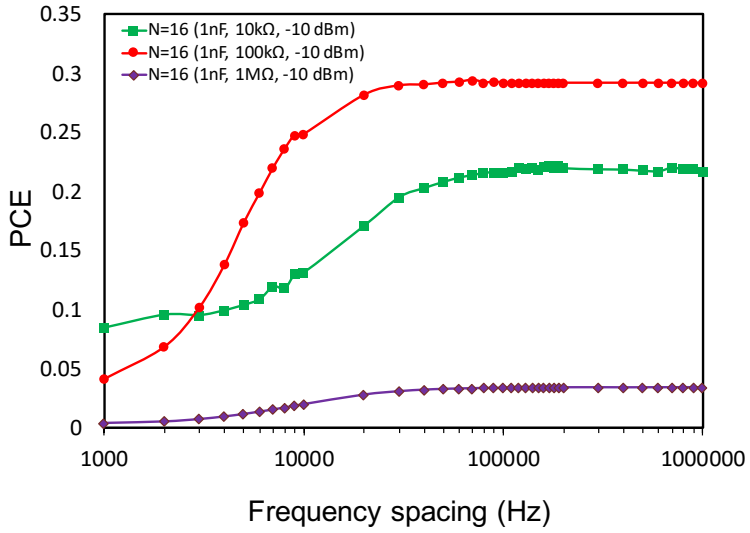

Fig. 2.9: PCE performances comparison against different load resistances (10 kΩ, 100 kΩ, and 1 MΩ). The number of tones was 16. C_{L} of tested rectifiers were all the same (1 nF), and input power was set to −10 dBm.

this LPF becomes larger, which means that the output voltage fluctuates even with higher frequency. However, because I matched the network for −10 dBm, I choose to use the threshold of setting saturation point from −10 dBm case.

Note that referring to Fig. 9, the highest PCE for −20 dBm input is approximately 0.1, and it is improved to 0.3 for −10 dBm input, and goes back down to approximately 0.23 for 0 dBm input. This is due to several reasons. First, the matching network of the measured rectifier circuit is optimized to −10 dBm input power. Therefore, a higher or a lower power than −10 dBm may cause impedance mismatch, which results in absorption of smaller power than the actual received power and deterioration of the PCE performance. Another reason is that the diodes I used is assumed to be low power usage. Here, low power is assumed to be approximately −30 dBm to −10 dBm. When the received power is relatively high (0 dBm input power), the diode cannot handle the high amplitude voltage, which causes current leakage from rectifier output to the matching network reversely, leading to performance degradation. The similar tendency can be observed in different paper as well [20]. The optimal input power for different number of tones is the future work.

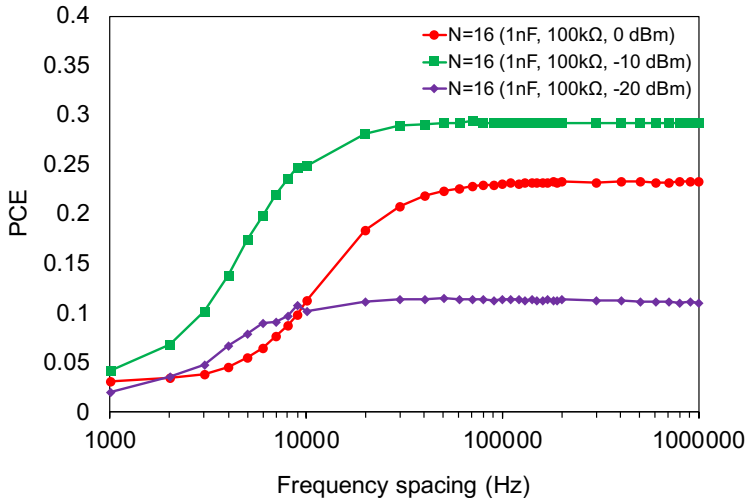

Fig. 2.10: PCE performance comparison against different input power levels (0 dBm, −10 dBm, and −20 dBm). The number of tones was 16. R_L and C_L of tested rectifiers were all the same (100 kΩ and 1 nF, respectively).

Frequency Spacing Characteristics against Different Diode Types

In addition, I tested rectifiers with different diode types to determine if I have the same tendency regardless of the types of the diodes. I used SMS7630–005LF, HSMS285C, and PCC110. The manufactured rectifiers are all voltage doubler type, and the parameters of the rectifier of C_L is 1 nF, and R_L is 100 kΩ for this experiment. The measurement result is shown in Fig. 2.11. Based on these results, I find a similar tendency in terms of frequency spacing characteristics, even with different diode types.

2.3.3 Simulation and Experimentation Comparison

In this section I discuss how the simulation can align to the experimental results. I have conducted simulation using Advanced Design System (ADS). The circuit diagram is the same as in Fig. 2.2. Impedance matching was conducted with Large-Signal S-Parameter Simulation (LSSP) at 915 MHz and manually tuned so that I obtained S11 to be smaller than −10 dB for 10 MHz bandwidth. The Q factor of the inductor in the matching circuit was set to 70 [122]. I have simulated using Harmonic Balance simulation to see the PCE performances

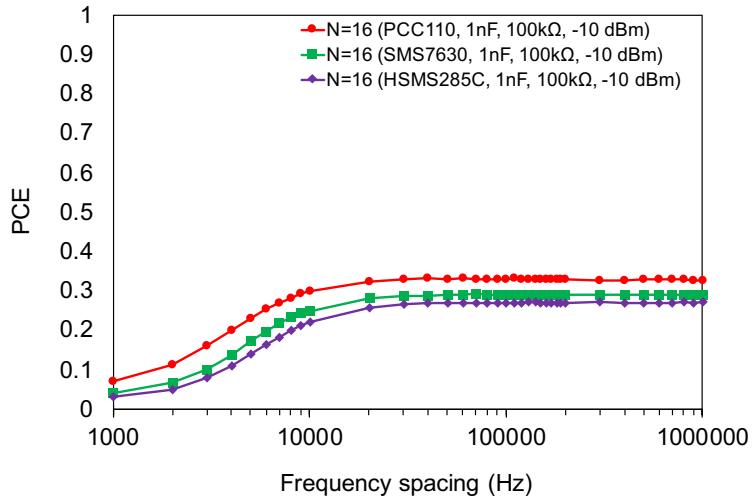

Fig. 2.11: PCE performances comparison against different types of diodes (SMS7630-005LF, HSMS285C, PCC110). The number of tones was 16. R_L and C_L of tested rectifiers were all the same (100 kΩ and 1 nF, respectively), and input power was set to −10 dBm.

when varying the frequency spacings between the tones. The R_L was set to 100 kΩ and different C_L were used, which is 100 pF, 1 nF, and 10 nF. Owing to the limitations of computational resources, The tested using the number of tones was set to 8.

The experimental and simulated results are shown in Fig. 2.12. Based on the results, the simulation results and experimental results have the same tendency in that increasing C_L by 10 times results in requiring larger frequency spacing by 10 times. However, in terms of the alignment with simulations and experiments, it shows that the simulation results show that it requires more frequency spacing than the experiment. For example, when $R_L = 100$ kΩ and $C_L = 1$ nF, the experimental result show that the saturation point occur at 100 kHz, but when it comes to simulation the point moves to approximately 300 kHz. One of the reasons to this misalignment may come from the stray elements in the actual circuits. Stray resistor causes the LPF formed based on the diode and load resistances to be changed so that the cutoff frequency becomes smaller than the simulation case.

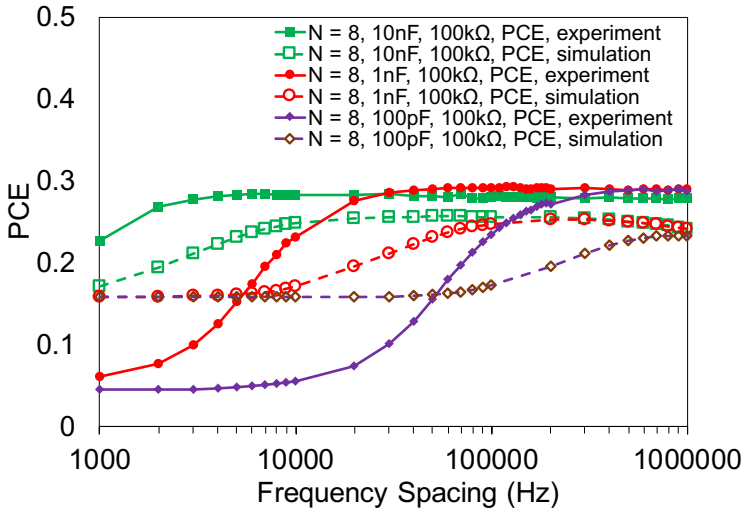

Fig. 2.12: PCE performances comparison against measurement and ADS simulations. Different capacitance (100 pF, 1 nF, and 10 nF) were used. The number of tones was 8. R_{L}s of tested rectifiers were all the same (100 kΩ). The input power was −10 dBm.

PCE Characteristics Under Wireless Channel Conditions

In this section I discuss how the PCE characterizations are affected by a wireless channel condition. The experimental conditions are the following: Both transmitter and receiver used 6.1 dBi patch antennas and were separated by 50 cm in an anechoic chamber (MY5310 from MICRONIX [123]). I tested with and without noise conditions in order to see the impact of noise channel. Because the SG does not support option for noise generation through ARB tool, I generated arbitrary signals using a Python library called RSWaveformGenerator [124] and feed them to SG in order to obtain signals with additive noise. I defined the multitone waveforms as symbols and varied the symbol-to-noise ratio $E_{\mathrm{s}}/N0$ from 40 dB to 10 dB. Here, $E_{\mathrm{s}}/N0$ is defined as follows [125];

$$E_{\mathrm{s}}/N0 = 10\log_{10}\frac{T_{\mathrm{symbol}}}{T_{\mathrm{sampling}}} + SNR, \tag{2.9}$$

where $T_{\mathrm{symbol}} = \frac{1}{\Delta f}$, and T_{sampling} is the sampling cycle, and SNR is the signal-to-noise ratio. I set the sampling frequency to 30 times larger than the Δf. Noise was assumed to be a white Gaussian noise. When generating signal using a Python library, the generated waveforms

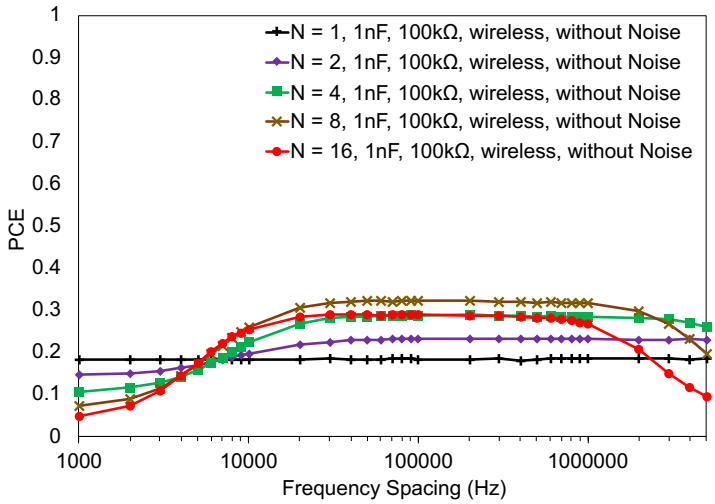

Fig. 2.13: PCE performances comparison against the different number of tones (1, 2, 4, 8, and 16) for the case of wireless transmission without noise condition. The tested rectifier had C_{L} of 1 nF and R_{L} of 100 kΩ. The received power was set to −10 dBm.

should not exceed amplitude over 1. This means that the generated waveforms have different power levels depending on the number of tones and the noise level. Therefore, the transmitted power must be tuned for each tested waveform in such ways that the received power has to reach −10 dBm. The tested rectifier has the parameters, R_{L} = 10 kΩ, and 100 kΩ, and C_{L} = 1 nF. The frequency spacings are varied from 1 kHz to 5 MHz.

The experimental results for wireless transmission without noise effects is shown in Fig. 2.13. I compared the number of tones from 1 to 16 for the case of (R_{L} = 100 kΩ, and C_{L} = 1 nF). The result demonstrate that the bandwidth limitation of the tested antenna can be observed when the total bandwidth becomes more than 32 MHz. Because increasing the number of tones results in having larger total bandwidth for a fixed Δf. Note that by changing or designing the antennas that can handle larger bandwidths, the PCE performance can be improve even with larger bandwidth. Considering that the bandwidth can be allocated up to 26 MHz at UHF, the working range of the antennas are proper.

I also tested how the noise affects the PCE characterizations. I show the results of the PCE performance when varying the $E_{\mathrm{s}}/N0$ from 40 dB to 10 dB in Fig. 2.14 (a) and (b),

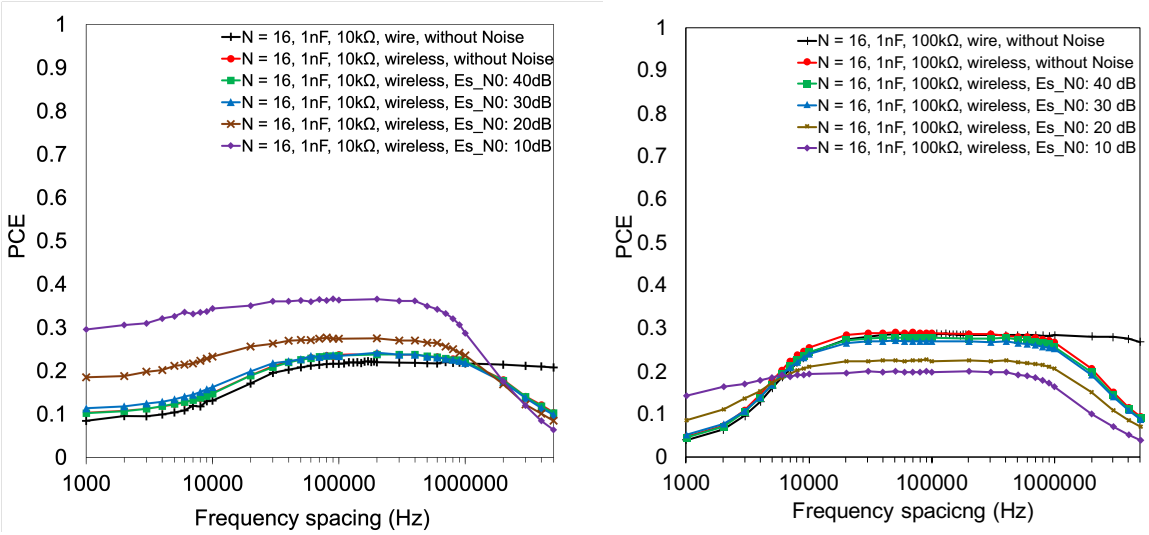

Fig. 2.14: PCE performances comparison against noise level for the case of wireless transmission with noise condition. The number of tones was set to 16. The received power was set to −10 dBm. The tested rectifier had parameters, (a). C_L of 1 nF and R_L of 10 kΩ, and (b). C_L of 1 nF and R_L of 100 kΩ.

respectively. The tested rectifiers have the following parameters; R_L = 10 kΩ and 100 kΩ, and C_L = 1 nF. The number of tones was set to 16 for these cases. I noticed that when R_L is low, addition of noise results in better PCE performances. In contrast, when R_L is high, the PCEs becomes inferior to the case without nose conditions. These results partially agree with the results from previous research that chaos wave which can be regarded as noise signal yield better PCE performances [80]. Based on the results, noise like waveforms are better when R_Ls are low.

2.3.4 Necessary Bandwidth Allocation

To summarize the results, the frequency spacing has to be large enough so that the PCE of the rectifier needs to be saturated for UHF narrowband multitone waveforms (from Section 2.3.2). The necessary frequency spacing (Δf) for C_L is experimentally obtained as follows

Table 2.3: The best number of tones (N_{best}) depending on R_{L} when the input power Pin was -10 dBm.

The best number of tones (N_{best})	suitable R_{L} range
1	< 10 kΩ
2	10 kΩ – 20 kΩ
4	20 kΩ – 40 kΩ
8	40 kΩ – 100 kΩ
16	> 100 kΩ

(from Section 2.3.2);

$$\Delta f \geq \frac{1}{10^4 \times C_{\text{L}}}, \tag{2.10}$$

In addition, the necessary number of tones is determined based on R_{L} to have better PCEs (from Section 2.3.2), which is listed in Table 2.3. For example, if R_{L} is more than 100 kΩ, then assigning 16 number of tones for the waveform gives the best PCE performance. From the table, I am able to obtain suitable multitone waveforms in order to obtain better PCE performances. The total bandwidth (BW) for the best scenario is as follows;

$$\frac{N_{\text{best}} - 1}{10^4 \times C_{\text{L}}} \leq BW \leq BW_{\text{circuit}}, \tag{2.11}$$

, where N_{best} is defined based on Table 2.3, and BW_{circuit} is the bandwidth limit that internal circuit can handle. In this case, $BW_{\text{circuit}} = 32$ MHz from previous results. Now, given that $C_{\text{L}} = 10$ nF, the suitable bandwidth should be more than 150 kHz in order to employ the advantage of the multitone waveform. Note that if the total bandwidth exceeds the available bandwidth at UHF, it is required to use a smaller number of tones or smaller frequency spacing.

2.4 Summary

In this chapter, the impact of multitone was characterized in terms of PCE performances with different parameters of rectifiers as well as the parameters of multitone waveforms in the UHF band. Based on the experiments, the existences of the saturation points have been revealed at

which the performance of PCE was maximised. The indication of the saturation point is that it is required to allocate sufficient frequency spacing to have the best PCE performance. In addition, by changing the parameters of each rectifier component, the most important element with regard to the saturation point was obtained, which is the storage capacitor. Based on the results obtained by the thorough experiments of both wire and wireless transmissions, the suitable waveforms for the specific rectifier parameters have been revealed. Finally, to observed a more practical channel, the experiments through wireless transmission under noise conditions have been tested.

Chapter 3

Multitone Waveform Design for Improving Sensitivities

3.1 Introduction

Application spaces of low power devices have expanded with the help of using wireless power transfer technologies. Wireless identification sensing platform (WISP) is one of such devices, which not only sense simple thing like temperature, but also take photos using camera, convey vocal information through Skype without battery [2, 53]. It contains energy harvesting module as well as communication module connecting to micro controller. The platform accepts various types of sensors. The reason that these devices can operate rich tasks without the use of battery is that they have done varieties of techniques with regard to the low power operations. For example, in order to do communications, they use backscatter communication

which does not require devices to actively radiate wireless signal. In addition, some devices do not embed analog to digital converters (ADCs), which enables them to do tasks like taking photos and receiving vocal information [2, 55, 27].

However, the more people demand for such devices to do expensive operations, the more energy they require for operation. For example, capturing per frame image consumes 10.4 mJ, so increasing frame rate requires more energy for operation [54]. In addition, the operation range of the WISPcam is only 2 m even with the 4 W EIRP [27]. Therefore, there is a trade off between level of operations and the working range. One of the obstacles that prevents these devices are limited to very short range is that it is required relatively large power to power them up. The Wispcam requires -12.1 dBm to start from the cold state, but once they powered up, they require only -15 dBm power for its operation. This indicates that it is required to charge twice as much as power in order to start from the cold states. In order to increase their operation range, it is important to apply higher voltage or increase the sensitivity to the rectifier since the rectified voltage or boost converted to the rectified voltage is watched by the voltage monitor modules [126].

Since there is a limitation of transmit power by Federal Communication Commissions (FCC), increasing its working range within the same average power is a critical problem. It is this reason that multitone based waveforms are assumed to be attractive to increase the sensitivity of these devices. As in regulation, FCC limits total power for transmission, however it does not specify the waveforms which means that as long as one keep the average power within the limits, it would be possible to transmit signal which has high peak to average ratio [127]. In the past years, many kinds of high PAPR signals have been explored, but I take into account the multitone waveforms [109].

In this chapter, I characterize the sensitivity performances based on the configurations of rectifiers and introduce the design instructions of multitone waveforms to improve the sensitivity based on rigorous experiments at UHF. In addition, I have conducted experiments not only through wired transmission, but also through wireless transmissions with noise effects in order to observe the impact of the performance in terms of the waveform distortions. Furthermore, I have tested the sensitivity characterizations with the real receiver circuits that are

commercially available to see the feasibility of using multitone waveforms as well as suggesting the design instructions of the devices in order to improve the sensitivities under multitone waveforms. The contributions of this chapter is summarized as follows;

- I have confirmed that the saturation point for the sensitivity (saturation point of peak voltage acquisition) exist similar to the PCE case, and the saturation points can be controlled or strongly affected by the value of storage capacitance (C_{L}) at the receiver. However, in contrast to the saturation point of PCEs, the saturation point of peak voltage acquisition comes approximately 100 times smaller than the saturation point of PCEs. In addition, the multitone waveform should assign less frequency spacing than the saturation points of the peak voltage acquisition, in order to obtain better sensitivity.

- The characterizations of the sensitivities of receiver devices depend on the DC–DC converters' roles. First, if the types of the receiver devices are such that the rectified voltage goes directly to DC-DC converter and stored in a tank capacitor with boosted voltage, then the characterizations of sensitivities have to consider both the storage capacitance before the DC–DC converter and the tank capacitance after the converter. Further, the input impedance of the DC–DC converter should be considered as well. Second, if the types of the receiver devices are such that the rectified current first stores in a storage capacitor and the DC–DC converter boost the voltage until the voltage in the storage capacitor exceeds the threshold value, then the characterizations of the receiver are the same as the rectifiers with high input impedance.

This chapter is structured as follows. In section. 3.2 the sensitivity characteristics of different types of rectifiers have been analyzed. The design guideline for having higher peak voltage or sensitivity can be modeled as well. In Section 3.3, the characteristics of commercially available receiver devices for multitone waveforms have been analyzed. The design nature of DC–DC converter that is included along with rectifier decides the characteristics of the performance when using multitone waveforms. These characteristics have been experimented through wireless transmissions. Finally, the summary of this chapter is discussed in Section 3.4.

3.2 Sensitivity Characterizations of Rectifiers

As having better PCEs is important, it is also vital to have better sensitivity in some applications such as wake-up devices from deep sleep [89, 27]. Typically, such devices equip a power management unit after the rectifier circuit, watching the voltage at the storage capacitor to see if the voltage goes beyond the threshold. The sensitivity is defined as the minimum input power when the voltage at the storage capacitor goes beyond the threshold voltage. Because achieving a higher voltage at the storage capacitor is different from obtaining higher PCEs, the waveform design for having better sensitivities should be different from what is required to improve PCEs. To formulate the waveform design instructions, I first characterize the output voltage (both peak and mean) of the various rectifiers. Then, I characterize the sensitivities of the two rectifier circuits that contain DC–DC converters, each of which has different circuit designs in the following sections. All the experiments are conducted with the same instruments and conditions as the previous section.

3.2.1 Frequency Spacing Characteristics against load resistances and The Number of Tones

I evaluated the output mean and peak voltages of two rectifiers whose parameters were (C_{L} = 1 nF and R_{L} = 10 kΩ, and C_{L} = 1 nF and R_{L} = 100 kΩ). The experimental results are shown in Fig. 3.1 and two distinct trends are observed.

First, in terms of frequency spacing response versus the mean voltages, the performance of mean voltages is similar to that obtained for the PCE cases. However, in contrast to the PCE cases, higher mean voltages are obtained when higher resistances are used. The mean voltage is saturated when the frequency spacing reaches the saturation point of PCE cases, and when it reaches this region, the mean voltage and the peak voltage converge to the same value.

Second, for the case of the peak voltage acquisition, the responses behave differently from what I observed in PCE cases, meaning that if the frequency spacing is small, the peak voltage becomes large. This is why the voltage ripple becomes large when the frequency spacing is

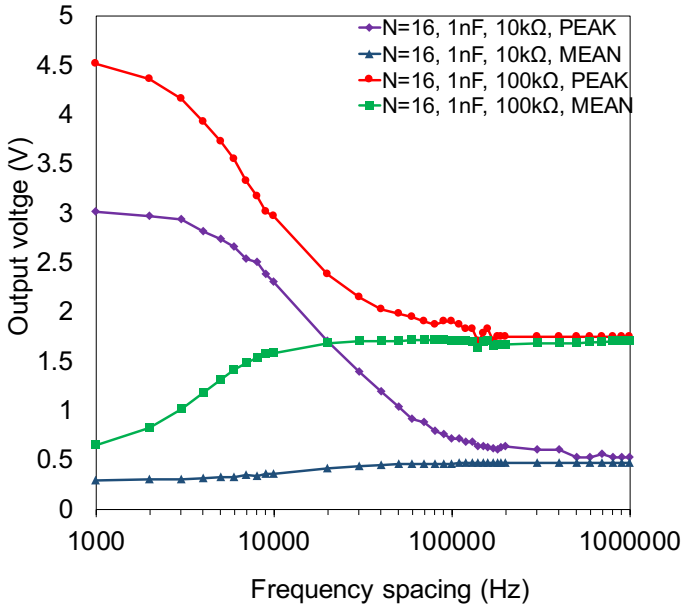

Fig. 3.1: Frequency spacing characteristics of rectifiers in terms of output voltage acquisition (both peak and mean voltages). The number of tones was 16. R_{L}s were 10 kΩ and 100 kΩ and C_{L} was 1 nF. The input power was set to −10 dBm.

small [128]. When the frequency spacing of the multitone waveforms is small, LPF formed by a diode and a storage capacitor cannot cut off the AC component. Thus, the outputs have ripples.

I also experimented the peak voltage acquisition of a rectifier (C_{L} = 1 nF and R_{L} = 100 kΩ) with a different number of tones. The result of the relationship between the number of tones and the frequency spacing is shown in Fig. 3.2. As can be seen, increasing the number of tones results an increment in the peak voltage. In addition, when the frequency spacing reaches the saturation point of PCE, the highest peak voltage depends on R_{L}. In this case, the load resistance is 100 kΩ; thus the highest peak voltage is yielded when setting the number of tones to be 16 based on Table 2.3. This concludes that when the frequency spacing is smaller or equal to $\frac{1}{10^4 \times C_{\mathrm{L}}}$, increasing the number of tones yields better performance in terms of obtaining higher peak output voltage. In contrast, when the frequency spacing is larger than that, selecting number of tones is required to refer to Table 2.3.

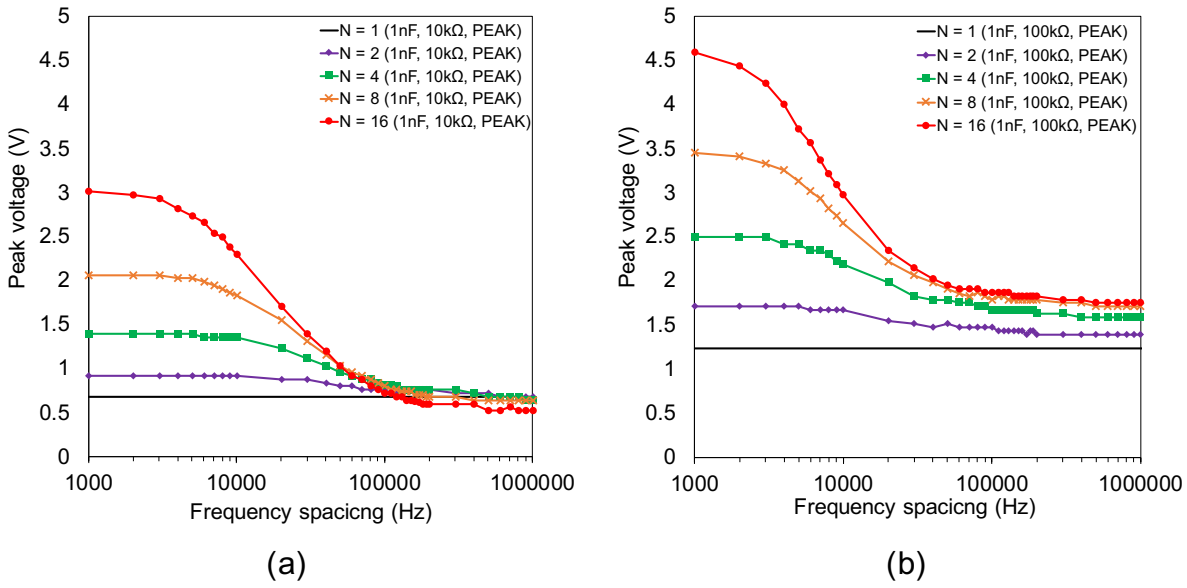

Fig. 3.2: Frequency spacing characteristics of rectifiers in terms of peak output voltage acquisition though wire transmission under ideal condition (without noise). The number of tones was varied from 1 to 16. The input power was set to −10 dBm. The rectifier parameter had, (a). R_L of 10 kΩ and C_L of 1 nF, and (b). R_L of 100 kΩ and C_L of 1 nF.

Finally, I tested how high the peak voltage can be available depending on R_L and the number of tones (Fig. 3.3). The frequency spacings are taken from the saturated points of peak voltage acquisition. For this case, 1 nF is used for C_L, so the saturation point comes at 1 kHz. As it can be seen, increasing the load resistance as well as the number of tone lead to obtaining higher peak voltages.

3.2.2 Frequency Spacing Characteristics against Storage Capacitance

To see the impact of C_L versus frequency spacing, I tested rectifiers with different C_L (100 pF, 1 nF, 10 nF) whose result is shown in Fig. 3.4. R_L was set to 100 kΩ. Based on the result, a strong relationship between C_L and the frequency spacing exists, similar to the PCE case, indicating that increasing the capacitance 10 times reduces the frequency spacing by a factor of 10 to obtain a saturation point of the peak voltage acquisition. Therefore, by varying the

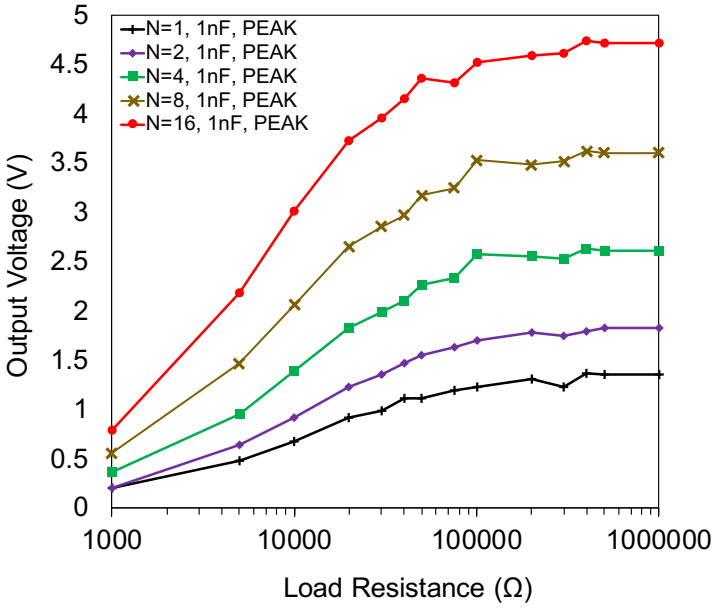

Fig. 3.3: The characterizations of peak voltage at the saturation point of output voltage acquisition (Δf = 1 kHz the rectifiers whose for C_{L} had 1 nF) versus different load resistances. The number of tones was varied from 1 to 16. R_{L} was varied from 1 kΩ to 1 MΩ. C_{L} was 1 nF. The input power was set to −10 dBm.

capacitance, it is possible to control the saturation points of peak voltage acquisitions. In addition, the saturation point of peak voltage acquisition is 10 kHz when C_{L} = 100 pF, which means that the saturation points of the peak voltage acquisition need around 100th times smaller frequency spacing than the saturation points of PCE, because from Section 2.3.2, the saturation point of PCE requires 1 MHz when C_{L} = 100 pF. Thus, in contrast to the characterization of the saturation point of PCE (Equation 2.10), the saturation points of peak voltage acquisition for the multitone waveforms can be obtained from the following equation;

$$\Delta f \leq \frac{1}{10^6 \times C_{\mathrm{L}}}. \tag{3.1}$$

3.2.3 Peak Voltage Characterization with Noise Conditions

I tested the sensitivity performances under the noise condition with wireless transmissions. The wireless transmission conditions are the same as explained in Section 2.3.3. I show

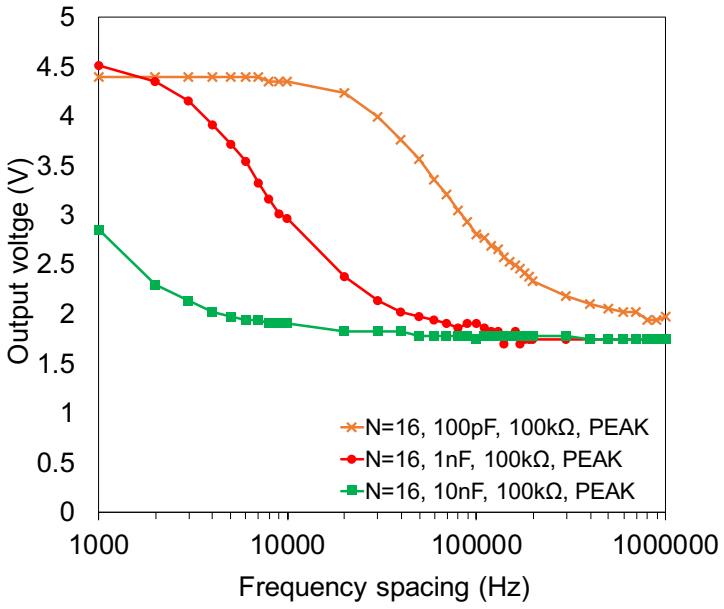

Fig. 3.4: Frequency spacing characteristics of rectifiers in terms of peak output voltage acquisition. The number of tones was 16. R_L was 100 kΩ, and C_L was 100 pF, 1 nF, or 10 nF. The input power was set to −10 dBm.

the results of the sensitivity performance when varying the $E_s/N0$ from 40 dB to 10 dB in Fig. 3.6 (a) and (b). The tested rectifiers have the following parameters; R_L = 10 kΩ and 100 kΩ and C_L = 1 nF. The number of tones is set to 16 for these cases. The results show that when R_L is small, the adding noise for small frequency spacing result in deteriorating to obtain higher peak voltage slightly. However, when the frequency spacing becomes more than 200 kHz, adding noise signals yield better output voltage acquisition. In contrast, when R_L is large, addition of noise resulted in deterioration of the performances.

3.2.4 Waveform Design Instruction for Obtaining High Peak Voltage

Based on the previously discussed rectifier characteristics in terms of output voltage, I can design instruction for the multitone waveforms. I divided into three regions (a, b, and c).

a. During the region ($\Delta f \leq \frac{1}{10^6 \times C_L}$), the obtained peak voltage is increased by adding the number of tones or increasing R_L. This region is a saturation region of peak voltage,

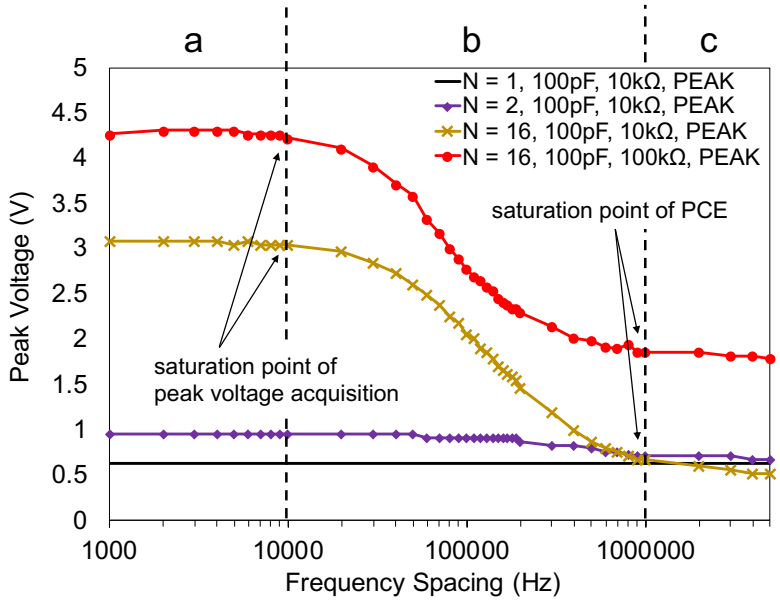

Fig. 3.5: The region explanation of peak voltage using the rectifiers that had $C_L = 100$ pF, $R_L = 100$ kΩ. The input power was -10 dBm.

and thus the peak voltage becomes the highest.

b. During the region, $(\frac{1}{10^6 \times C_L} < \Delta f \leq \frac{1}{10^4 \times C_L})$ a higher peak voltage is obtained by the same rule in (a). The difference between (a) and (b) is whether the region is in the saturation region. In this region, as the Δf increases, the peak voltage becomes smaller.

c. During the region $(\Delta f > \frac{1}{10^4 \times C_L})$, a higher peak voltage is maximized depending on the load resistance. Therefore, it is required to refer to the Table 2.3. Note that if the rectifier can change R_L, then having a higher resistance results in yielding a higher peak voltage.

As an example, for the case of a rectifier whose $C_L = 100$ pF and $R_L = 10$ kΩ as in Fig. 3.5, from 1 kHz to 10 kHz (saturation region), the peak voltage of the rectifier yields the highest when the number of tones is 16 (region a). During the region from 10 kHz to 1 MHz (region b), the peak voltage for the case when the number of tones can still be obtained by increasing the number of tones, but the peak voltage decreases as the frequency spacing increases.

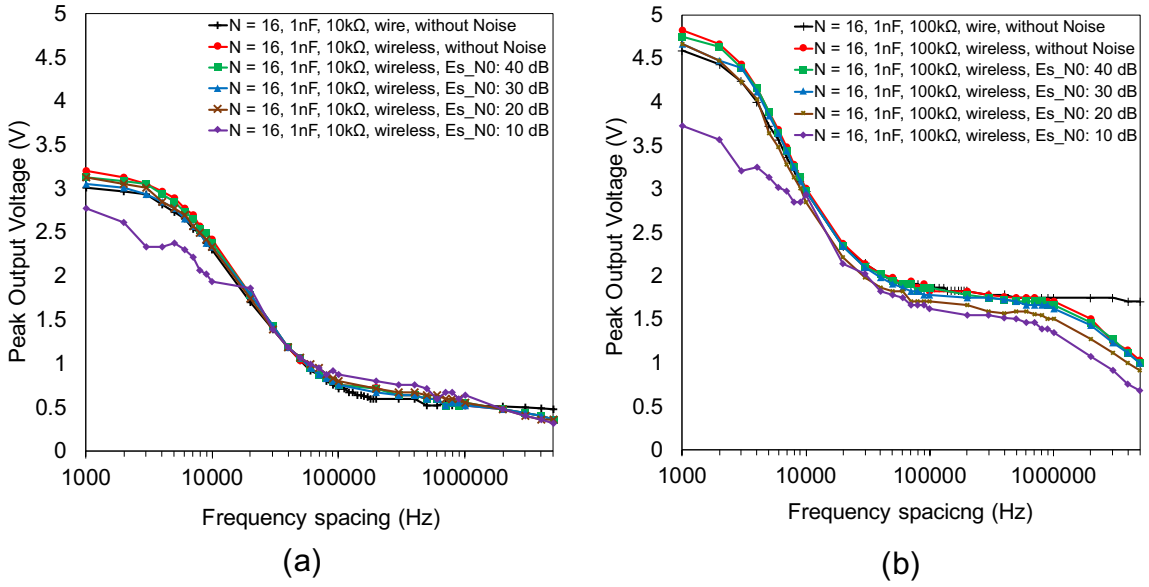

Fig. 3.6: Peak voltage characterizations under noise condition through wireless transmissions. The number of tones was set to 16. Frequency spacing was varied from 1 kHz to 5 MHz. The received power was set to −10 dBm. The circuit parameter had (a). R_{L} of 10 kΩ and C_{L} of 1 nF, and (b). R_{L} of 100 kΩ and C_{L} of 1 nF.

Finally, if the spacing becomes larger than 1 MHz, the peak voltage can be achieved when the number of tones is 2. In this region, the output voltage is saturated because it corresponds to the saturation point of PCE. In such case, the peak and mean voltages correspond to each other. Because the PCEs are relative to output mean voltage, the peak voltage acquisition performances correspond to the PCE performances. The PCE performance when saturated depends on the Table 2.3. This indicates that the number of tones is selected based on Table 2.3 in the region c. The number of tones in this case must be 2 from the table. I also plot the case when R_{L} is 100 kΩ and the capacitance is 100 pF. I observe that the frequency response becomes similar to the case where R_{L} is 100 kΩ and the capacitance is 100 pF, where the frequency response becomes similar irrespective of R_{L}. In this case, $N = 16$ yielded the highest voltage based on Table 2.3.

Table 3.1: input impedance analysis of Seiko charge pump (S882Z)

state	current (μA)	voltage (mV)	impedance (kΩ)
output ends	32.2	300	10.3
output starts	19.5	300	15.4

3.3 Sensitivity Characterizations of Rectifiers with DC–DC Converters

3.3.1 Circuit Structure Differences

On the one hand, the rectified voltage goes to the DC–DC converter before being stored in a large capacitor for the WISP 5.1 case. In such a case, the DC–DC converter continuously absorbs rectified current, so it is necessary to consider the input impedance of the DC-DC converter. Based on the result of measuring the input impedance of the Seiko charge pump (Table 3.1), it is found that the input impedance is approximately 10 kΩ, so in this case, the rectifier is modeled as a low resistance model.

On the other hand, for the case of P2110B, the rectified voltage goes to the storage capacitor before the DC-DC converter. Therefore, while it is required to consider the input impedance of the DC-DC converter for WISP 5.1, P2110B can be modeled as a rectifier without load because the voltage monitor disconnect the path between the capacitor and boost converter until the voltage across the capacitor reaches a threshold value. In the next subsection, I observe the sensitivities of each receiver device with respect to the frequency spacing.

3.3.2 Sensitivity Analysis of WISP 5.1

Previously, the output voltage performance of the rectifiers has been characterized. The trends show that for lower frequency spacing, large voltage ripple occurs, which is useful in terms of sensitivities of receiver circuits as the higher voltage overcomes the voltage threshold to wake-up devices. To observe these effects, I conducted sensitivity experiments using rectifiers with DC–DC converters; one is WISP 5.1, and the other is P2110B. The differences between these stem from the circuit designs [126, 129].

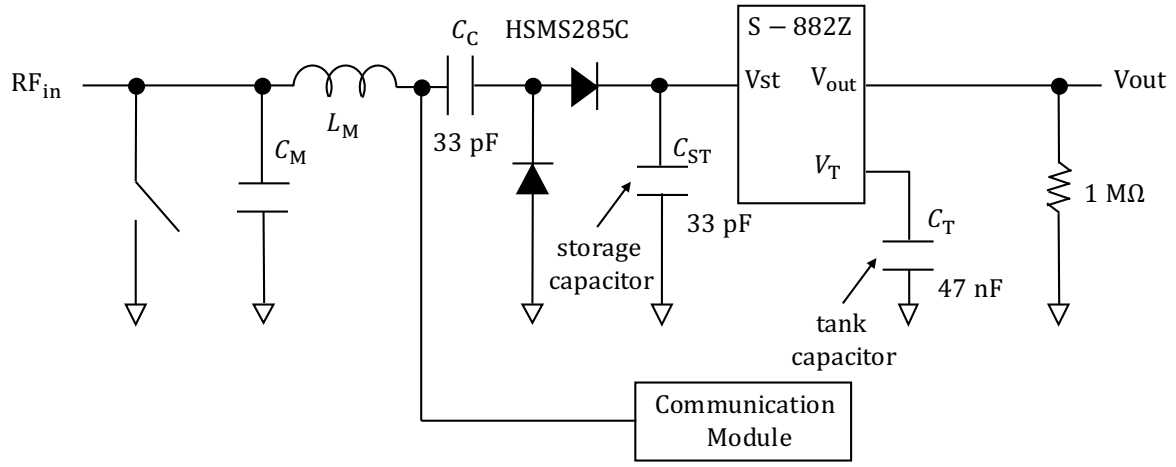

Fig. 3.7: Brief schematic of WISP 5.1

(a) (b)

Fig. 3.8: WISP 5.1 actual circuit. (a): manufactured WISP unmodified. (b). modified WISP 5.1 for experiments. Antenna was cut and SMA connector was connected. In addition, matching networks were modified.

WISP 5.1 Schematics and Modification for Experiments

Part of its schematic is shown in Fig. 3.8. 33 pF was used for both a DC blocking capacitor (C_c) and a storage capacitor (C_{ST}). HSMS285C was utilized for rectifications. For the boost converter, Seiko's charge pump (S-882Z) was used. This charge pump stores in a tank capacitor (C_T = 47 nF) until it reaches a certain voltage threshold. I skipped the detailed schematics of the communication module. 1 MΩ, was placed on the load resistor. Because the internal power management unit of the charge pump determines the start of output from the tank capacitor and the input impedance of S882Z is approximately 10 kΩ from Table 3.1, the suitable rectifier model is 47 nF capacitor with 10 kΩ.

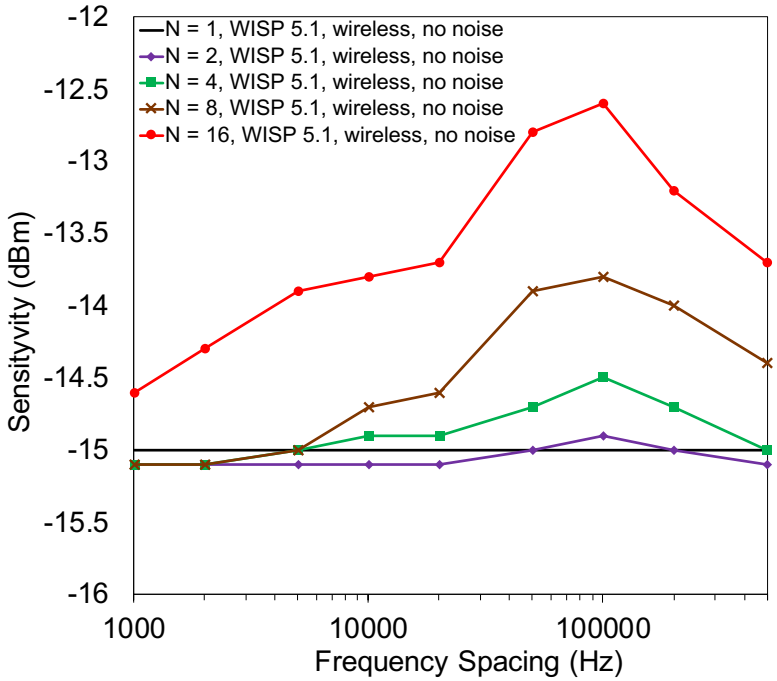

Fig. 3.9: Sensitivity comparison against various tones and bandwidth were measured using the WISP 5.1. The number of tones was varied from 1 to 16, and the frequency spacing was varied from 1 kHz to 1 MHz. The experiments have done through wireless transmission.

To perform the measurements, some part of WISP 5.1 should be modified because it embeds an antenna to a printed circuit board (PCB), and could not receive the signal from SG through cable originally. First, I cut out an antenna part and placed a SubMiniature version A (SMA) connector to a port. Then, I reconfigured the matching network so that the impedance is matched to 50 Ω. I redo the impedance matching from old configurations to the new ones (20 nH (Coilcraft 0603CT), and 6 pF). I evaluated the sensitivity of the WISP 5.1 device against multitone signals and a single tone signal under the noise condition through wireless transmission. The experimental setups for wireless transmissions are the same as before. The sensitivity of the device is obtained based on minimum input power when a boost converter triggers its output (V_{out}).

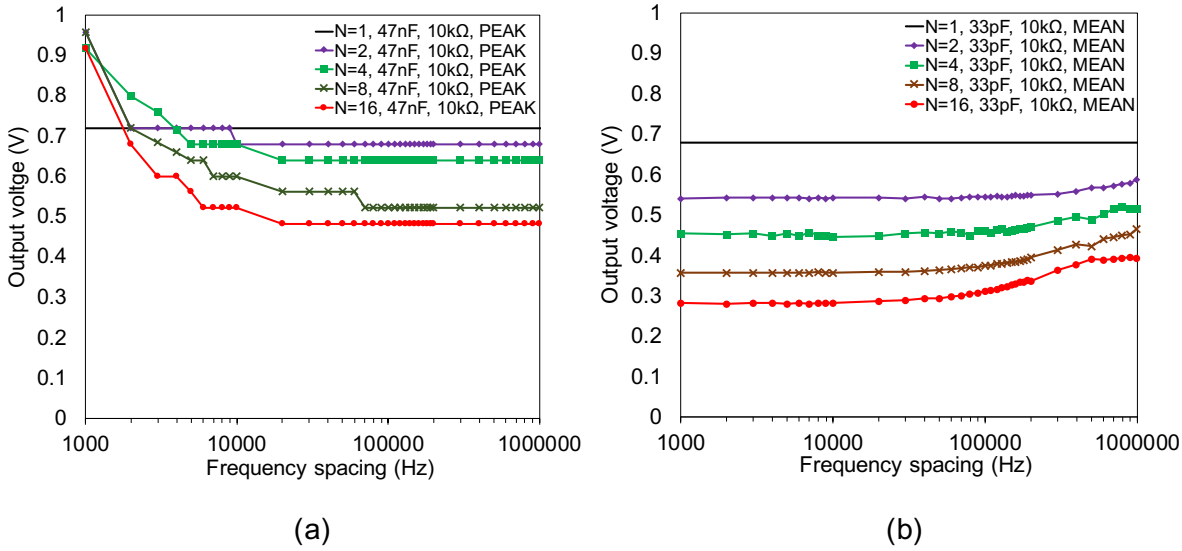

Fig. 3.10: Frequency spacing characteristics of a rectifier (model: Fig. 2.2) in terms of voltage acquisition. The number of tones was varied from 1 to 16 with wire transmission under ideal condition (without noise). The input power was set to −10 dBm. The rectifier's parameter was (a). $R_L = 10$ kΩ, and $C_L = 47$ nF measuring peak voltage, and (a). $R_L = 10$ kΩ, and $C_L = 33$ pF measuring mean voltage.

Sensitivity Characterization of WISP 5.1 through Wireless Channel

The measurement results of WISP 5.1's sensitivity with different frequency spacing through wireless transmissions is shown in Fig. 3.9. Different number of tones were tested under noiseless conditions. There are three things to be noticed in this experiment. First, the sensitivity of using multitone waveforms are deteriorated as the number of tones is added. Because the boost converter (S-882Z) has relatively low input impedance (10 kΩ from Table 3.1), adding the number of tones degrades the sensitivity.

Second, when the assigned frequency spacing is up to 100 kHz the sensitivity of the WISP 5.1 increases, or deteriorates, as the frequency spacing increases. This behavior is similar to the frequency spacing response of a rectifier that has $C_L = 47$ nF and $R_L = 10$ kΩ. As shown in Fig. 3.10 (a), the peak voltage of a rectifier that has $C_L = 47$ nF and $R_L = 10$ kΩ decreases as the frequency spacing is decreased up to 100 kHz. This partially confirms that the WISP 5.1 can be modeled as the rectifier with $C_L = 47$ nF and $R_L = 10$ kΩ. This also clarifies the

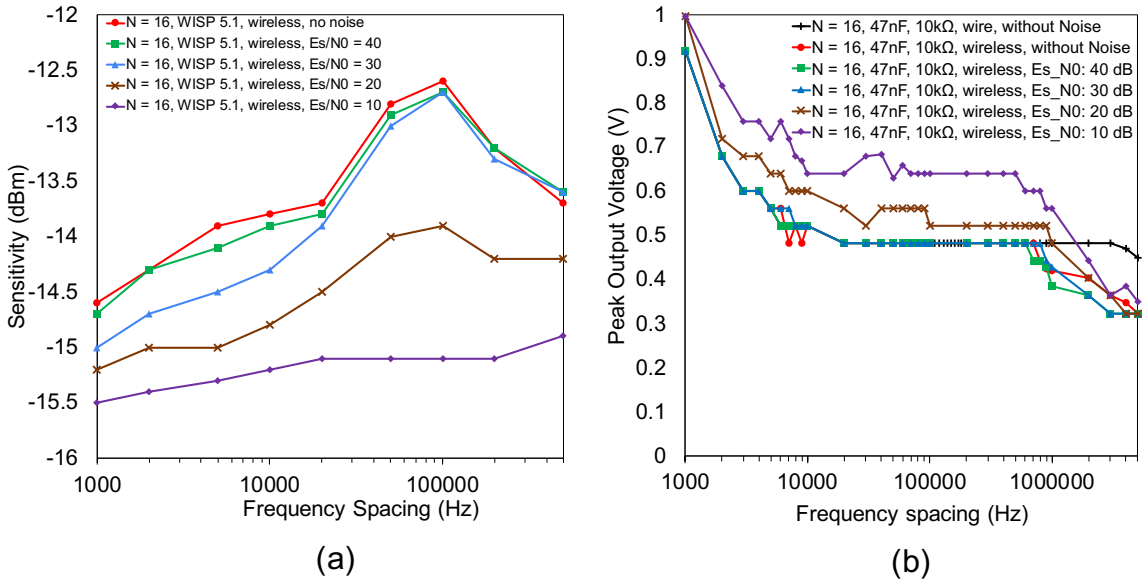

Fig. 3.11: Sensitivity comparison against different noise level were measured using WISP 5.1. The number of tones was set to 16 and the frequency spacing was varied from 1 kHz to 5 MHz. The experiments have done through wireless transmission with noise condition.

fact that adding the number of tones deteriorates the sensitivity performance as mentioned in the previous paragraph. However, when the frequency spacing is greater than 100 kHz, the sensitivity of the WISP 5.1 improves while the performance of the modeled rectifier is stable. Therefore, additional modeling is required to explain the sensitivity behavior of the WISP 5.1.

Third, when the frequency spacing becomes more than 100 kHz the sensitivity of WISP 5.1 increases, as shown in Fig. 3.9. This behavior is because the storage capacitor (33 pF) of the WISP 5.1 improves the charging capability after 100 kHz. That is to say, the mean voltage applied to the storage capacitor increases as the frequency spacing increases, and the amount of the current that goes into the charge pump increases. To check this, I conducted an experiment using a rectifier that has $C_{\mathrm{L}} = 33$ pF and $R_{\mathrm{L}} = 10$ kΩ (Fig. 3.10 (b)). The result shows that when the frequency spacing becomes more than 100 kHz, the mean voltage of the output gradually increases. This is why the sensitivity of WISP 5.1 improves in the region.

I tested the sensitivity performances under the noise conditions whose number of tones

are set to 16, as shown in Fig. 3.11 (a). Increasing the noise level results in having better sensitivity performances. This tendency corresponded to the results of peak voltage acquisitions obtained from the rectifier whose parameters are (C_L = 47 nF and R_L = 10 kΩ) in Fig. 3.11 (b).

Discussions

Overall, to understand the sensitivity of the receiver device that has boost converter embedded, it is required to consider both the storage and tank capacitors that are located before and after the converter, respectively. In particular, it is important to have a stable high mean voltage at the input of the converter and to have a high peak voltage at the output stage. For these observations, to obtain the best performance in terms of sensitivity, the storage capacitance should be large enough to saturate the mean voltage with smaller frequency spacing, and relatively smaller value for the tank capacitor so that higher peak voltage can be obtained. For example, if one want to have the best sensitivity performance, I can choose storage capacitance to be 1 nF and the tank capacitance to be 100 pF. Then multitone waveforms with 10 kHz frequency spacing yield the best performance in terms of sensitivities.

However, the values of storage and the tank capacitance of the original WISP 5.1 are fixed at the factory; thus, it is not generally possible to arrange after being manufactured. Thus, to maximize the sensitivity within this configuration (original WISP 5.1), the waveform has to be set so that the frequency spacing is 21 Hz or smaller, based on the discussion of the previous section (section 3.2.4, closure a). However, due to the measurement equipment's limitation, I could not confirm the sensitivity behavior with frequency spacing smaller than 1 kHz.

3.3.3 Sensitivity Characterizations of P2110B

Next, I conducted a sensitivity experiment using P2110B. This module consists of matching networks, rectifier circuits, and boost converter, as shown in Fig. 3.12. The rectified current is stored in the storage capacitor, and this current does not enter into the boost converter until it starts to output. The output process starts when the voltage across the capacitor goes over the threshold value determined by the voltage monitor. Therefore, this type of rectifier

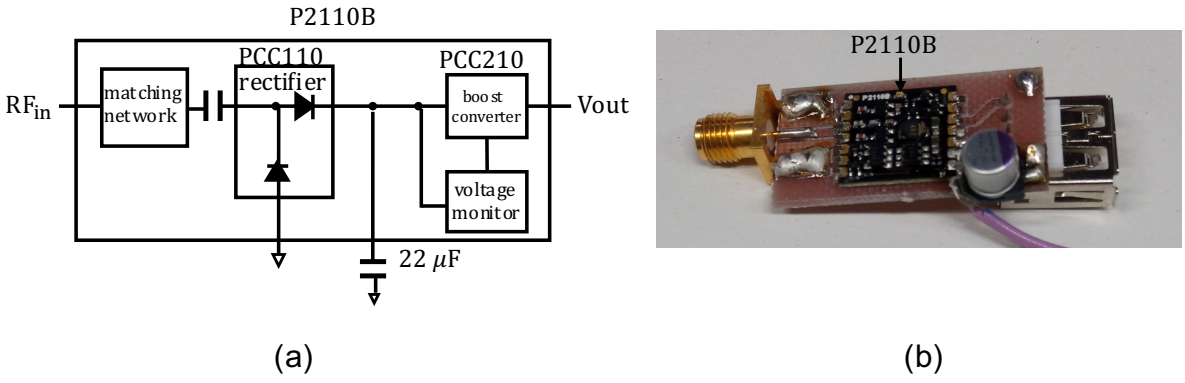

Fig. 3.12: Brief schematic of P2110B and a photo of the manufactured circuit.

could be modeled as a high load-resistance type, and thus, adding the number of tones may improve the sensitivities. Here, the sensitivity defined as the input power when the output voltage is induced from the storage capacitor. As for the capacitance, I used 22 μF aluminum electrolysis. Because this module is matched already, I did not modify the matching network. The experiments were conducted through wireless transmission.

The measurement result through wireless transmission without noise interference is shown in Fig. 3.13 (a). As expected, the sensitivity of the P2110B-type receiver improves as the number of tones is increased. As shown in Fig. 3.2 (b), when R_L is large, increasing the number of tones yields better PCEs. Because PCEs are measured based on mean voltage and when the frequency spacing is in the saturation point of PCE, the peak voltage and mean voltage converge, increasing the number of tones results in obtaining larger peak voltage. Because the tested device uses 22 μF capacitor, the saturation point of PCE is approximately 4.5 Hz. These facts confirm that sensitivity behavior is reasonable in this case. In addition, because the saturation point of PCE already occurs at approximately 4.5 Hz, the sensitivity performance does not improve depending on the frequency spacing in the experiment. Here, note that the capacitance does not affect to the PCE performance. This is confirmed from Fig. 3.4. When the frequency spacing has more than saturation point of PCE, the peak output voltage converges to the same value regardless of capacitance.

The sensitivity characterizations through wireless transmissions under the noise conditions

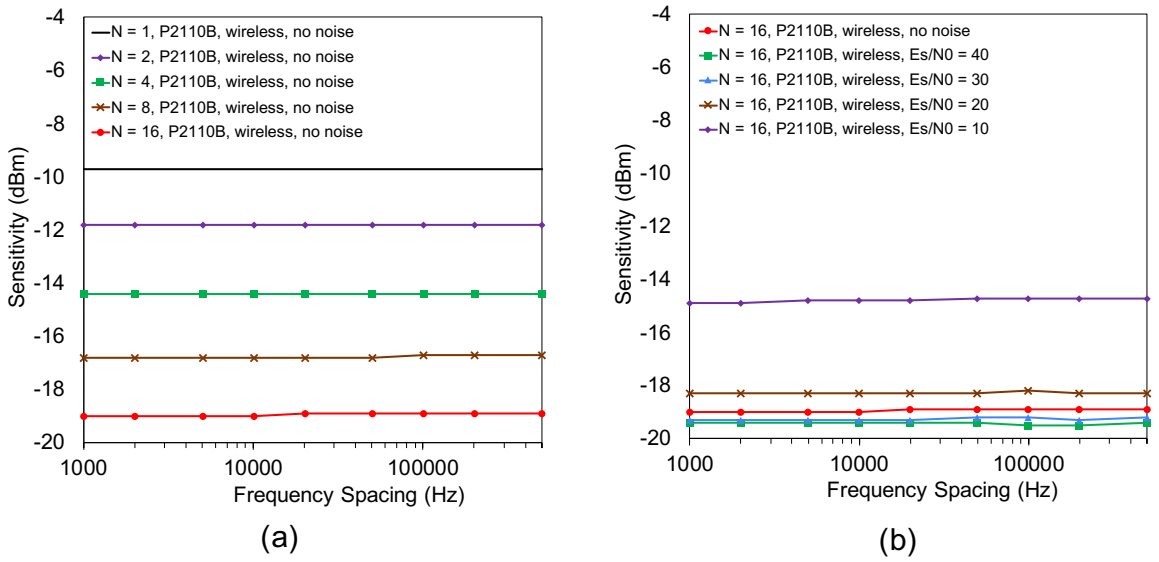

Fig. 3.13: Sensitivity comparison against various tones and bandwidth using the P2110B. The frequency spacing was varied from 1 kHz to 5 MHz. The experiment was conducted through wireless transmission; (a). under ideal condition (without noise), and the number of tones was varied from 1 to 16, (b). under noise condition whose $E_s/N0$ was varied from 40 dB to 10 dB, and the number of tones was set to 16. Different number of tones also yielded the same trend. The received power to -10 dBm for both experiments

are shown in Fig. 3.13 (b). The number of tones was set to 16, and the received power was set to -10 dBm. In this case, adding noise level deteriorates the sensitivity performances, which is different from the trends for the case of sensitivity characterization of WISP 5.1. As discussed in Section 3.2.3, when R_L is low, addition of noise contributes to positive effect in term of sensitivity and vice versa. Because P2110B can be modeled as high-load resistance, addition of noise deteriorates the sensitivity performance.

3.4 Summary

In this chapter, I characterized the effect of the frequency spacing of multitone waveforms in terms of rectifiers' sensitivities for voltage-doubler type rectifiers in the UHF band. The experiments conducted help demonstrate that that rectifiers exhibit frequency selectivity; thus,

a suitable frequency spacing (saturation point) of multitone waveforms is required to have better sensitivities. In addition, I have revealed that the saturation points and storage capacitance have strong relationships. Further, the advantages of using multitone waveforms depend primarily on R_{L}. Therefore, by observing C_{L} and R_{L}, I could design suitable multitone waveforms in order to obtain better PCE performances or sensitivities. These characterizations are similar to those of PCEs. However, the saturation point movements are different from each other. Specifically, the required frequency spacing needs to be as short as possible in order to have higher peak voltage in contrast to the PCE cases where the frequency spacing has to be assigned adequately large enough. In addition, the relationship between PCE saturation points and the sensitivity ones approximately are revealed. Based on the experiments through wire and wireless transmissions, the PCE saturation points comes 100 times larger spacing than the saturation point of peak voltage acquisitions.

Furthermore, I tested the sensitivities of practical receiver devices that have a DC–DC converter when using multitone waveforms. I have found that for the devices where the tank capacitor stores the voltage after the DC–DC converter boosts the rectified voltage, the sensitivities with respect to the frequency spacing are affected by input impedance, storage capacitance at the rectifier, and the tank capacitance after the DC-DC converter. In contrast, for the devices where the rectified voltage is stored in a storage capacitor and boosted after the voltage of the capacitor reaches a certain value, the input impedance of DC-DC converter is negligible so that the behavior of the performances resembles the rectifier with a high load resistance.

Despite the fact that I modeled using individual parameters, it is challenging to model the suitable waveforms using different parameters such as load resistances and capacitances, which is the future work.

CHAPTER 4

WAVEFORM DESIGN FOR FREQUENCY-SHIFTED SWIPT USING MULTITONE WAVEFORM

4.1 Introduction

The Internet of Things (IoT) has gained much attention as billions of devices can be connected through networks capturing information and influencing our decisions in our daily lives [59]. However, as numerous devices are installed everywhere, battery management is becoming cumbersome, as most of them require batteries or wired power sources. Eliminating batteries would ease the recharging processes; devices would sustainably exist ubiquitously and seamlessly around us [130]. These devices need external power sources for the substitution of batteries, and among the emerging energy harvesting methods, wireless power transmission is attractive. This is because devices can obtain RF transmitted power based on their needs

instead of harvesting occasionally from solar power, vibration, or other harvesting technologies. Among the wireless power transmission methods, I aim to utilize the radio frequency (RF) power harvesting method instead of coupling based methods so that the devices can be operated without being in close proximity to the transmitter [131].

It has been revealed that using the same waveforms, not only power but also information can be delivered, known as simultaneous wireless and information power transfer (SWIPT). In such context, the information is superimposed on wireless power transferred waveforms [58, 68, 132, 133, 62]. In addition, it is possible to share the antennas for information and power reception, which is attractive in terms of reducing additional costs for embedding extra antennas and meeting the requirements for a small form factor of IoT devices.

However, realizing the SWIPT system with high speed and high power efficiency is challenging for battery-less IoT nodes since its low power operation restricts the conventional communication method, which uses power-hungry RF front end (power amplifiers, local oscillators, etc) [131, 134]. Recently, a method for optimizing power allocation for communication and power harvesting for a nonlinear circuit has been proposed [135]. However, designing SWIPT waveforms based on conventional communication modules is still a challenging task. In specific, it is necessary to design transmit waveforms such that IoT nodes can handle wireless information without using active devices that would reduce the power efficiency.

Recently, a multitone RF harvesting method has been proposed in order to produce higher power conversion efficiency with the same transmit power compared with continuous wave (CW) power harvesting waveforms [66, 68, 136]. This waveform consists of summations of multiple sine waves and produces high peak-to-average power ratios. This nature gives a higher power conversion efficiency (PCE) at the receiver node due to the nonlinearity effects of diodes in the rectifiers. Therefore, using these waveforms has more advantages than continuous wave (CW) [79, 108, 137].

In addition, this multitone waveform can also be used for conveying information without the need for power-hungry elements; this is called multitone SWIPT. Since nonlinear elements output intermodulation products of the input waveform, it is possible to generate varieties of

outputs using multitone waveforms. Therefore, differently designed input waveforms can be distinguishable by measuring the rectified outputs.

Multitone SWIPT can be realized by arranging the amplitudes, frequencies, phases of each tone or by varying the number of tones [101, 138, 98, 66, 98, 139]. Among these methods, modulation based on the number of tones is one of the attractive approaches in that it uses peak to average power ratio (PAPR) fluctuations by varying the number of tones in the transmitted waveform [99, 140]. These authors revealed the tradeoff between the communication rate and the DC supply capability. While an increased number of tones results in larger rectified voltage, the communication rate becomes poor. This is due to the fact that increasing the number of tones in a fixed bandwidth results in shortening the frequency spacing. Since the communication rate severely depends on the frequency spacing, shortening frequency spacing leads to having poor communication rate. On the other hand, if the number of tones is minimized, the communication rate can be maximized. However, DC rectified voltage cannot be improved so much. Therefore, it is important to design the waveforms based on the requirements of the SWIPT devices, which is also discussed in [67].

Frequency shift-type SWIPT has been considered as one of the solutions to increase the modulation orders within the same number of tones [67]. In this method, the spacing of the frequency tones is varied in order to perform modulation. They employ the intermodulation products of the harmonic signal generated by the diodes in the rectifiers to retrieve information. Since different frequency tone configurations generate different intermodulation products, the receiver could solve the inverse problem by evaluating the spectrum of the waveform in the frequency domain. This enables the use of higher-order modulation within the same number of tones. However, in most cases, fast Fourier transfer (FFT) is applied to acquire the variations of frequency spacing in this scheme, which is more challenging for battery-less devices to implement in terms of calculating cost. Therefore, achieving high-performance communication while maintaining high PCE with simple receiver hardware is a challenging task. It is true that a passive bandpass filter bank can be used for frequency separation instead of calculating FFTs. However, especially when the communication bandwidth is small, designing a passband passive filter becomes challenging due to the requirement of a high Q

factor. For example, at UHF, the passive bandpass filter needs to have a bandwidth of at least 1.5 MHz, which means that tones that reside within 1.5 MHz cannot be differentiated through the filter. Therefore, at UHF, where communication is typically suppressed under 1 MHz, conventional multitone FSK SWIPT needs to rely on the FFT calculation.

In this chapter, I applied a PAPR based signal detection method to the frequency shift-type multitone SWIPT scheme. Based on our analysis, different tone configurations in the frequency domain yield varieties of nonlinear outputs from a rectifier. In addition, specific nonlinear output patterns depend on the tone configurations. Due to this feature, it is possible to demodulate a signal at the receiver side in the time domain instead of in the frequency domain by introducing PAPR based measurements. This makes it possible to demodulate frequency shift-type SWIPT with a simple circuit structure. Our contributions are the following;

- I showed the principles of how frequency shift tones change the PAPRs at the receiver side and demonstrate the validity of the scheme through simulation and experiments.
- I estimated and verified how many PAPRs could be produced with the same number of tones and investigated the communication rate with the optimal tone configurations.
- I verified that our introduced receiver circuit can differentiate all the possible PAPRs generated by the same number of tones through circuit simulation as well as experiments.

This chapter is structured as follows. In Section 4.2, I show the relationship between the configuration of tones and the PAPR values of the outputs at the receiver side. In Section 4.3, I categorize the tone configurations based on the PAPRs, and estimate how many different PAPRs could be generated within the same number of tones. In addition, I estimate the maximal communication rate. Then, in Section 4.4, I introduce the receiver circuit that can realize this idea and show the feasibility of the PAPR based method. I compared the with the most related method in Section. 4.5. Finally, I summarize this chapter in Section 4.6.

4.2 PAPR based Signal Detection Principle

4.2.1 Signal Description

Multisine based waveforms $x_{\mathrm{T}}(t)$ at a transmitter are modeled as follows;

$$x_{\mathrm{T}}(t) = \mathrm{Re}\Big\{ \sum_{i=1}^{N} \sqrt{\frac{P_{\mathrm{T}} R_{\mathrm{TxAnt}}}{N}} \exp\big(j(\omega_i t + \phi_i)\big) \Big\}, \tag{4.1}$$

where N, P_{T}, R_{TxAnt}, ω_i, and ϕ_i represent the number of tones, the transmit power, the impedance of the transmitter antenna, the angular frequency of the ith tone that is equal to $2\pi f_i$, and the phase of the ith tone, respectively. Here, f_i is a carrier frequency of the ith tone. I assume that each fundamental tone has the condition;

$$f_i < f_j, \textit{ for } i < j \in N. \tag{4.2}$$

In addition, the bandwidth BW is fixed, so $f_N - f_1$ always becomes BW.

At the receiver side, when the impedance between the antenna and the input impedance seen from the antenna to the rest of the circuit (R_{in}) are matched, the received power (P_{R}) that is consumed at the impedance R_{in} can be derived using Friss's equation [11];

$$P_{\mathrm{R}} = P_{\mathrm{T}} G_{\mathrm{T}} G_{\mathrm{R}} \Big(\frac{\lambda}{4\pi d} \Big)^2, \tag{4.3}$$

where G_{T}, G_{R}, λ, and d are the transmitter gain, the receiver gain, the wavelength of the traversing signal, and the distance between the transmitter and the receiver, respectively. Therefore, the received signal $y_{\mathrm{R}}(t)$ can be expressed as;

$$y_{\mathrm{R}}(t) = \sqrt{P_{\mathrm{T}} G_{\mathrm{T}} G_{\mathrm{R}} \Big(\frac{\lambda}{4\pi d} \Big)^2 R_{\mathrm{in}}}. \tag{4.4}$$

Here, I assume that the antenna impedance of the receiver and transmitter sides are the same. In addition, I assume that the antenna impedance and the impedance of the following circuit system are the same at the receiver side. In such condition, the excited voltage at the receiver circuit ($v_{\mathrm{in}}(t)$) is the same as $y_{\mathrm{R}}(t)$. Since $P_{\mathrm{T}} = \mathrm{E}\{x_{\mathrm{T}}^2(t)/R_{\mathrm{in}}\}$, the excited voltage is expressed as $v_{\mathrm{in}}(t) = h x_{\mathrm{T}}(t)$, where h is the degradation factor.

4.2.2 Harmonic Signal Generation and Rectification

During the process of the rectification, diodes in the receiver circuit generate harmonic signals, and they modulate with each other due to the diodes' nonlinearity [33]. As a result, the signals are downconverted to the baseband (BB) region. The harmonic signals ($v_{\mathrm{in_h}}(t)$) become the following;

$$\begin{aligned} v_{\mathrm{in_h}}(t) &= h\{C_1 x_{\mathrm{T}}(t) + (C_2 x_{\mathrm{T}}(t))^2 + (C_3 x_{\mathrm{T}}(t))^3 + \dots\} \\ &= C_1' x_{\mathrm{T}}(t) + (C_2' x_{\mathrm{T}}(t))^2 + (C_3' x_{\mathrm{T}}(t))^3 + \dots, \end{aligned} \tag{4.5}$$

where $C_1' = hC_1$, $C_2' = \sqrt[2]{h}C_2$, $C_3' = \sqrt[3]{h}C_3$. For example, if a 3-tone signal is transmitted, the transmitted and excited voltage at the receiver side would become following;

$$x_{\mathrm{T}}(t) = \sum_{i=1}^{N} a\cos(\omega_i t), \tag{4.6}$$

$$\begin{aligned} v_{\mathrm{in_h}}(t) &= \frac{3}{2}C_2'^2 a^2 \\ &+ C_2'^2 a^2 \sum_{i<j} \cos(\omega_i t - \omega_j t) \\ &+ \left\{C_1' a + \frac{15}{4}C_3'^3 a^3\right\} \sum_{i=1}^{3} \cos(\omega_i t) \\ &+ \frac{3}{4}C_3'^3 a^3 \left\{\sum_{i<j} \cos(2\omega_i t - \omega_j t)\right\} \\ &+ \frac{3}{2}C_3'^3 a^3 \left\{\sum_{i\neq j\neq k,\ i<j} \cos(\omega_i t + \omega_j t - \omega_k t)\right\} \\ &+ \mathit{higher-order\ terms}, \end{aligned} \tag{4.7}$$

where $a = \sqrt{\frac{P_{\mathrm{T}}}{N}}$, and I assume that up to a 3rd order signal would be generated through the diode, and the input waveform contains 3 tones in this case. Among the higher order terms in Eq. (4.7), the direct current (DC) term and the second order intermodulation products (IM2) terms dominate the output behaviors [33]. The latter terms in Eq. (4.7) consist of the frequency differences between the fundamental tones, which indicates that these tones are scattered around the baseband region, and the farthest tones are located as $f_N - f_1 = BW$. The waveforms of the output voltage change depending on the arrangement of the tones in the

frequency domain.

In addition, the output voltage behaviors are affected by the RC design of the rectifiers. According to the previous papers, the cutoff frequencies of the RC filter in the rectifiers can be determined by $F_{\text{cutoff}} = \frac{1}{2\pi R_{\text{L}} C_{\text{L}}}$ [104]. When the rectified signal contains the tones that have frequencies higher than the F_{cutoff}, these tones are ceased and the output waveform does not contain the ceased tones in the frequency domain. Therefore, a tradeoff exists between the arrangement of the IM2s and the cutoff frequencies. In order to discuss the tradeoff between the tone arrangement and the output waveform behavior, I bring the idea of F_{ratio}, which is determined by the ratio between the frequency difference (Δf) and the cutoff frequency, namely, $\Delta f / F_{\text{cutoff}}$ from the previous papers [67, 104]. In order to take the nonlinear effect of the diodes into account, it is required to compare the cutoff frequency with the IM2 tone that is the farthest, or $BW = f_N - f_1$, away from 0 Hz. In that context, Δf in this case needs to be BW. Therefore, F_{ratio} in this context is BW/F_{cutoff}.

PAPRs are utilized as a way to decode output symbols. Assuming that the output voltage is obtained as V_{out}, then the PAPRs are obtained based on the following;

$$PAPR = \left\{ \frac{\max(V_{\text{out}}(t))}{E(V_{\text{out}}(t))} \right\}^2. \tag{4.8}$$

Note that, usually for obtaining PAPR, it is required to calculate average powers and peak powers. However, since the output V_{out} is in the DC region, obtaining the verage voltage and peak voltage first and then calculating the square of peak voltage divided by the average voltage is enough. This may reduce the calculation cost. The behaviors of the voltage transitions from the rectification processes to the output are discussed in [104, 116, 56].

As an example, consider the case of $N = 3$, and each tone is located at f_1, f_2, and f_3, respectively in the frequency domain. As in Fig. 4.1 on the top, when the tones are evenly distributed, the frequency spacing between the adjacent tones are the same, namely $|f_2 - f_1| = |f_3 - f_2| = \Delta f$. In such a case, the frequency differences of the IM2 in the waveform become multiples of Δf, and the IM2 tones whose frequencies are Δf overlaps in the frequency domain as indicated at the top center in Fig. 4.1. On the other hand, if the frequency spacings are different from each other, namely $\Delta f(1,2) \neq \Delta f(2,3)$, then the IM2s scatter in the frequency domain. These differences enable the differentiation of the PAPR values, and hence allow the

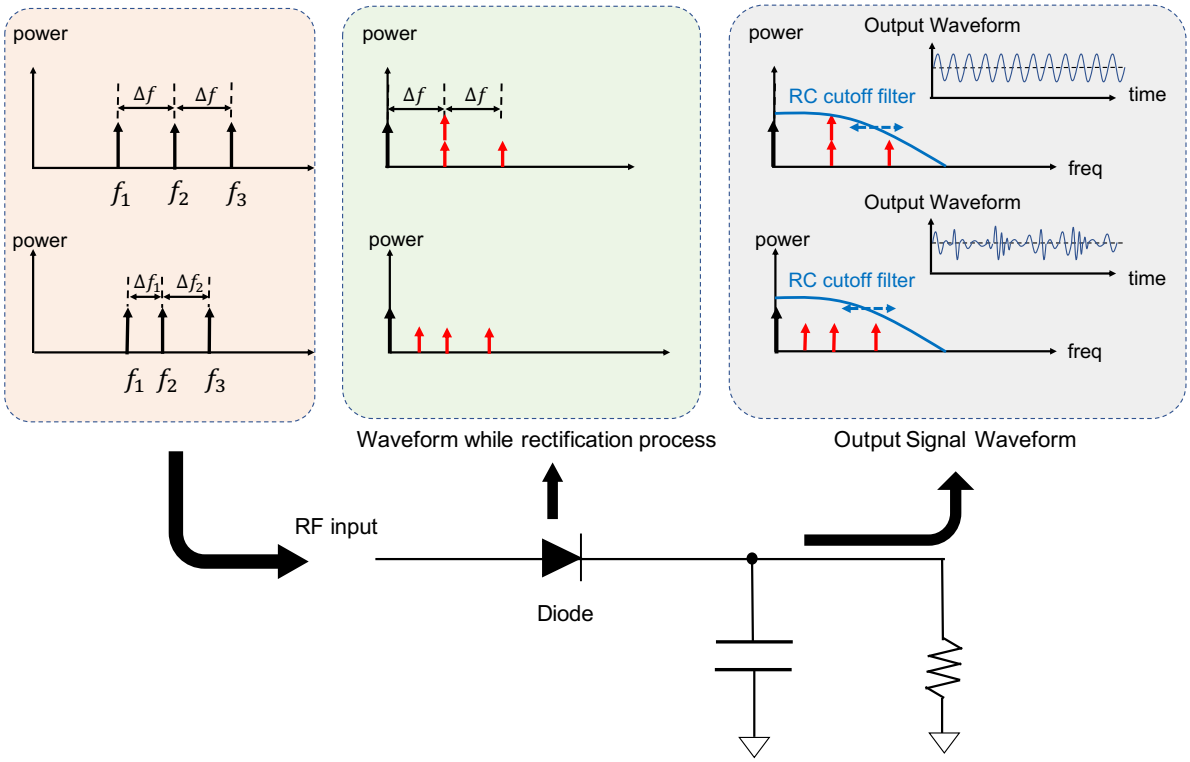

Fig. 4.1: Explanation of how output voltage changes depending on the tone configurations for the case of $N = 3$. Depending on the tone configurations of the input waveforms, intermodulation products of harmonic generated signals range through the process of rectification.

receiver devices to decode the signal. As it can be seen in Fig. 4.1 at the top right, when the IM2 tones are inside the RC cutoff frequency, all the tones can be seen at the outputs. This results in having varieties of output behaviors. However, when the RC cutoff frequency is too small, the output behaviors between the two examples do not differ with each other. Thus, it is required to properly design the RC filters in order to differentiate the tone configurations based on the outputs.

4.2.3 Simulation and Experimental Setup

In order to see the PAPR differences caused by changing the tone arrangements of the multitone waveforms and how they differ with the total bandwidth, I conducted simulations and

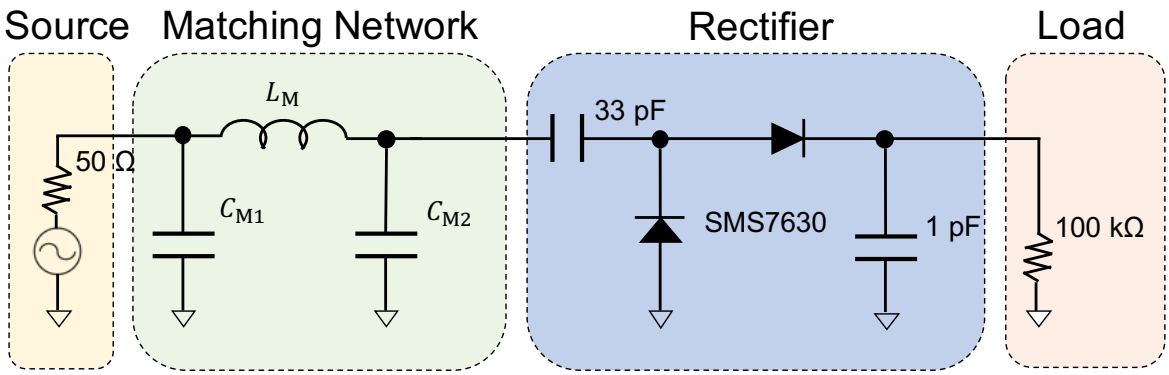

Fig. 4.2: The tested rectifier circuit for the experiment and simulation. Matching networks for hardware and software are different from each other.

Table 4.1: PAPR differences for even and uneven tone configurations for $P_{\text{in}} = -10$ dBm and $BW = 200$ kHz.

	even	uneven (averaged)	uneven (standard deviation)
simulation	2.00	1.83	0.01
experiment	4.69	3.48	0.38

experiments using the rectifier whose circuit diagram is shown in Fig. 4.2. As for the simulation, I used a harmonic balance simulations from an advanced design system (ADS) circuit simulator.

For the experiments, I implemented the rectifier and directly connected to a signal generator (SMB100A). I measured the output rectified voltage through an oscilloscope (RTO1024) and calculated the PAPR values based on Eq. 4.8. For the signal generation, the number of tones was set to 3, and the signal bandwidth was fixed to 200 kHz. The carrier frequency was set to 915 MHz. The tone arrangements were $f_c - \frac{BW}{2}$, $f_c - \frac{BW}{2} + xBW$, and $f_c + \frac{BW}{2}$ respectively, and x ranged from 0.1 to 0.9. Here, f_c is the carrier frequency. The rectifier consisted of a matching network, a voltage doubler rectifier, a storage capacitor, and a load resistor. I used this type of rectifier since it is popular among the RF power harvesting community [55]. The diode type was SMS7630-005LF. The capacitance and load resistance were set to 1 pF and 100 kΩ, respectively. I manually optimized the matching network for both simulation and

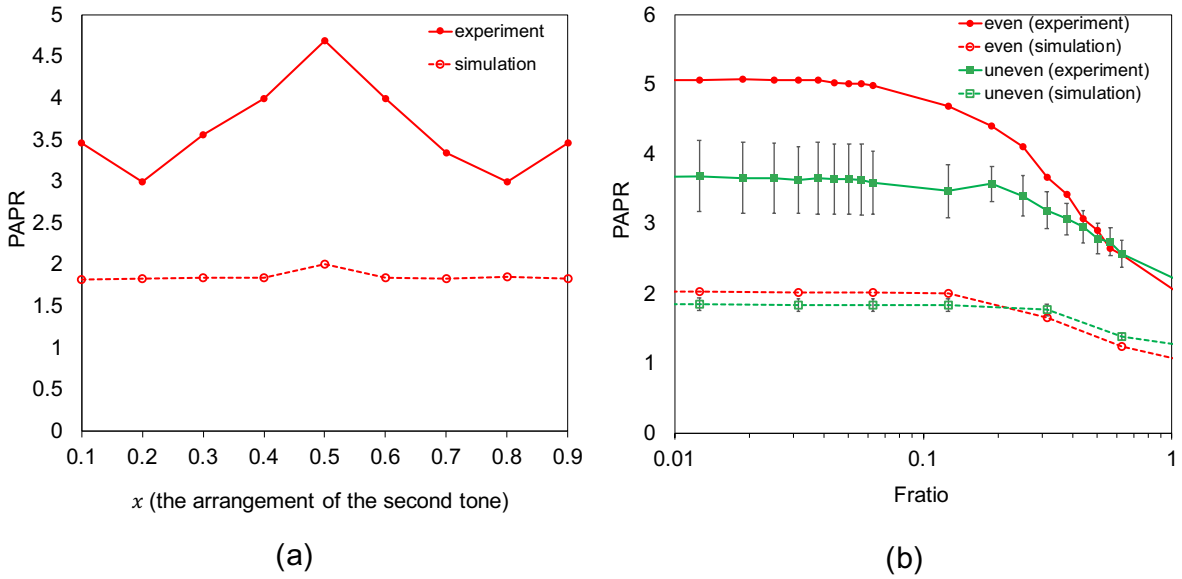

Fig. 4.3: Simulation and experimental result of PAPR variations using a single rectifier circuit. x represents the arrangement of the middle tone among the three tones. The number of tones of the multitone signal was 3, the total bandwidth was set to 200 kHz, and the input power was -10 dBm.

experiment. As for the simulation, I conducted Large-Signal S-Parameter Simulation (LSSP) at 915 MHz frequency and optimized for the input power of -10 dBm. For the real implementation, I used a Vector Network Analyzer (VNA) ZNB20 in order to perform impedance matching.

4.2.4 Preliminary Results

The simulation and experimental results when sweeping the middle tone in the frequency domain of the multitone waveforms were shown in Fig. 4.3 (a). When the tones are evenly distributed in the frequency domain ($x = 0.5$), the obtained output PAPR became the largest among the other cases for both simulation and experiment. I show the PAPR values for the evenly distributed case and the uneven case in Table 4.1 when $P_{\text{in}} = -10$ dBm and $BW = 200$ kHz. Note that I compare the evenly distributed case with the unevenly distributed case that are obtained by averaging the results of 8 cases (from $x = 0.1$ to $x = 0.9$, excluding $x =$

0.5) including the standard deviations. Although the PAPR difference was only 0.17 for the simulation result, that difference becomes larger in the experiment.

However, this tendency does not hold when the F_{ratio} becomes large. I plot the simulation and the experimental results of PAPR behavior differences against the F_{ratio} in Fig. 4.3 (b). It shows that when F_{ratio} is higher than 0.2, the PAPR differences for the even and the uneven cases become almost the same, and the relationship is reversed after that for the case of the simulation. The experimental result also shows the same trend, but the threshold value becomes 0.4 instead of 0.2. This shows the limitation of this method. However, in terms of using this method at UHF, where the communication bandwidth only requires 200 kHz, the system does not require a larger F_{ratio} [98].

Based on the aforementioned discussions, it is required to have the F_{ratio} to be at most 0.4. Considering that the communication bandwidth requires only up to 200 kHz, under the condition that $F_{\text{ratio}} \leq 0.4$, the cutoff frequency must be set according to:

$$F_{\text{cutoff}} \geq \frac{BW}{0.4}. \tag{4.9}$$

Therefore, the RC product ($R_{\text{L}}C_{\text{L}}$) needs to be satisfied as;

$$R_{\text{L}}C_{\text{L}} \leq \frac{0.4}{2\pi BW}. \tag{4.10}$$

When setting the load resistance to be 100 kΩ the capacitance must be smaller than 3.18 pF. In the experiment, the selected 1 pF and 100 kΩ met these criteria.

4.3 Information Encoding Method

From the previous section (4.2.2–4.2.4), I revealed that the differences in PAPRs depend on the number of equal values in the IM2s, which also correspond to how many overlaps occur at the output in the frequency domain. Based on this, I would reveal how many different PAPRs can be produced for a given number of tones and what kind of tone variations would yield specific PAPRs. The former is needed for estimating the modulation order, which is required to obtain the communication rate. The modulation order M is defined as the following;

$$M = \log_2\{N_{\text{categories}}\}, \tag{4.11}$$

where $N_{\text{categories}}$ is the number of possible different PAPRs to be generated based on the tone arrangements.

4.3.1 Modulation Order Estimation

Estimation of The Total Number of Frequency Spacings

When the number of tones are N, $N_{\text{TotalPairs}} = N(N-1)/2$ numbers of the IM2s are generated, each of which is expressed as $\Delta f(i,j), \forall i,j \in N, i < j$. As an example, when N is 4, the IM2 are $\Delta f(1,2)$, $\Delta f(1,3)$, $\Delta f(1,4)$, $\Delta f(2,3)$, $\Delta f(2,4)$, and $\Delta f(3,4)$. Therefore, there are 6 IM2s to be generated.

Categorizations

$N_{\text{TotalPairs}}$ number of IM2 tones generate the varieties of PAPRs depending on the arrangement of the tones in the waveforms. One of my goal is to categorize the tone configurations of the frequency tones according to PAPR values. This leads to revealing how many different symbols can be produced within the number of tones. In order to correctly formulate the categorizations, I start with an example case to get some insights.

4 tone case When $N = 4$, based on an exhaustive search, I can categorize the configurations of the input waveforms to a receiver into 4, as shown in Fig. 4.4. In Category A, the tone configurations are such that $\Delta f(1,2) = \Delta f(2,3) = \Delta f(3,4)$ and $\Delta f(1,3) = \Delta f(2,4)$. This case occurs when all the tones are evenly distributed. There are 3 equals that can be observed when one see the right hand side of Fig. 4.4, 3 overlaps occur at the output. In Category B, there are two pairs of IM2s corresponding to the two frequency differences. For example, one of the tone combinations is $\Delta f(1,2) = \Delta f(3,4)$ and $\Delta f(1,3) = \Delta f(2,4)$, but $\Delta f(1,3) \neq \Delta f(3,4)$. In this case, there are 2 overlaps at the output. In the same way, in Category C, there is only one pair of IM2s that has the same frequency differences, where only 1 overlap happens at the output. Finally, in Category D, each tone does not have the same frequency difference. At the output side, the IM2 tones are scattered around in the frequency domain.

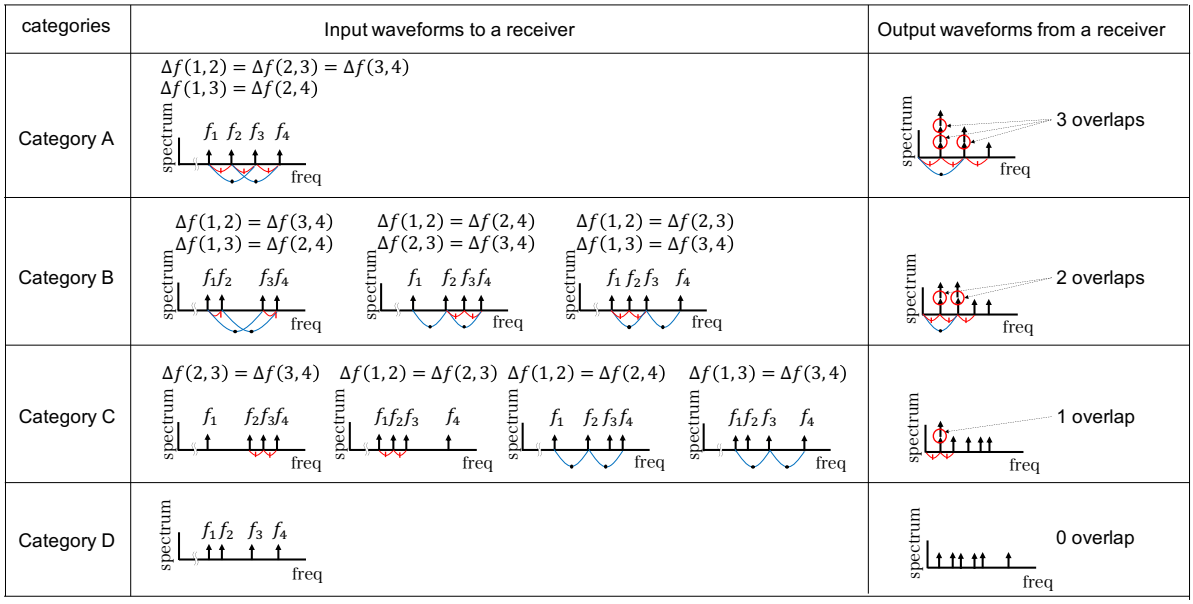

Fig. 4.4: The categories of the tone configurations based on the different PAPR values generated at the output.

The key findings are the following. First, the number of equals does not exceed 3 among the pairs of IM2s when $N = 4$. Moreover, this 3 consist of 2 equals coming from the adjacent tones ($\Delta f(1,2) = \Delta f(2,3) = \Delta f(3,4)$), and 1 from every other tone ($\Delta f(1,3) = \Delta f(2,4)$). No pair is more than two tones apart. In addition, at least on of the tone combinations exists for the case when the number of equals are 0, 1, 2, or 3. Therefore, in total, the number of categories obtained is 4 for $N = 4$.

General Case Based on the aforementioned discussions, in the general case, the number of categories can be counted for all the cases when the number of equal values in the IM2 is 0, 1, ..., $N_{\text{EqualNumbers}}$, where $N_{\text{EqualNumbers}}$ is the maximum number of equals that IM2 can produce, which can be achieved when the tones are evenly distributed. Therefore, $N_{\text{EqualNumbers}}$ consists of $(N-2)$ equals from the adjacent tones, $(N-3)$ equals from every other tone, ..., 1 equal. Therefore, I can derive $N_{\text{EqualNumbers}} = \frac{(N-1)(N-2)}{2}$. Overall, the number of categories ($N_{\text{categories}}$) is $N_{\text{EqualNumbers}} + 1$ since the number of equal values in the IM2s have either 0, 1, ...,

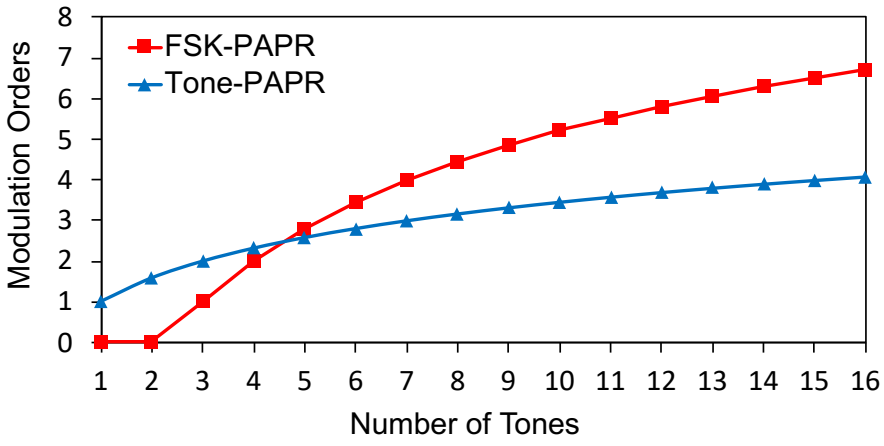

Fig. 4.5: The number of tones versus modulation orders; I compared my scheme with the conventional Tone-PAPR based modulation scheme.

$N_{\text{EqualNumbers}}$. As a result, the modulation order M can be obtained by the following equation;

$$M = \log_2\{(N-1)(N-2)/2 + 1\}. \tag{4.12}$$

The relationship between the modulation orders with regard to the given N is shown in Fig. 4.5. I compared with the conventional modulation scheme based on the number of tones, which is labeled as Tone-PAPR in this figure [99]. Based on this result, my method can reduce the number of tones in order to achieve a higher-order modulation scheme under the condition that $N \geq 5$. On the other hand, the previous FSK PAPR method only requires to have different IM2 tone arrangements for obtaining different symbols; the tone configurations can be considered almost infinitely by varying the size of the frequency spacings [67]. Therefore, in terms of modulation order, my scheme is inferior to the previous system.

4.3.2 Communication Rate

Next, I will estimate the communication rate in this section. The communication rate can be obtained by the minimum frequency spacing Δf_{min} among the tones and the modulation order M. Therefore, the communication rate can be expressed as follows;

$$R = \Delta f_{\text{min}} \times M. \tag{4.13}$$

However, revealing $\Delta f_{\min}$ is not trivial since it is required to arrange the tone configuration in the frequency domain, which results in having different frequency spacing among the symbols. In order to analyze $\Delta f_{\min}$, I introduce two parameters; *Scale* and *factor*. *Scale* constrains the minimum frequency spacing that adjacent tones can take. The adjacent tones have to be separated by a multiple of $\Delta f_{\text{scale}} = BW/Scale$. The parameter, *factor*, represents how many times the actual $\Delta f_{\min}$ is multiplied by Δf_{scale} among the transmitting symbols. Therefore, the minimum frequency spacing can be expressed as follows;

$$\Delta f_{\min} = \frac{factor \times BW}{Scale}. \tag{4.14}$$

Finally, the spectrum efficiency can be determined by the normalized throughput, which is expressed as;

$$S_{\text{E}} = \frac{R}{BW}. \tag{4.15}$$

In this section I will discuss how these parameters relate to each other and I will compare the spectrum efficiencies with the existing methods.

4.3.3 Parameter Selections

In this section, I will discuss the relation between the communication rate and the choice of *Scale*. If the *Scale* is large, the Δf_{scale} becomes small. Thus, many varieties of the combinations of the IM2s can be considered. However, this results in having a low communication rate as it is rate-limited by the Δf_{scale}. On the other hand, if *Scale* is small, the communication rate becomes faster, but the number of combinations becomes poor, and not all the types of combinations can be obtained. This may render the method unable to convey information in the extreme case.

4 tone case

I show the relationship between the *Scale* and the tone placement in Fig. 4.6 (a). As it can be seen from the figure, increasing the *Scale* results in having small Δf_{scale} and eventually having small $\Delta f_{\min}$. However, the number of tone arrangements increases since the number of indices that the second and the third tone can choose increases. Note that the 1st and the last tone are

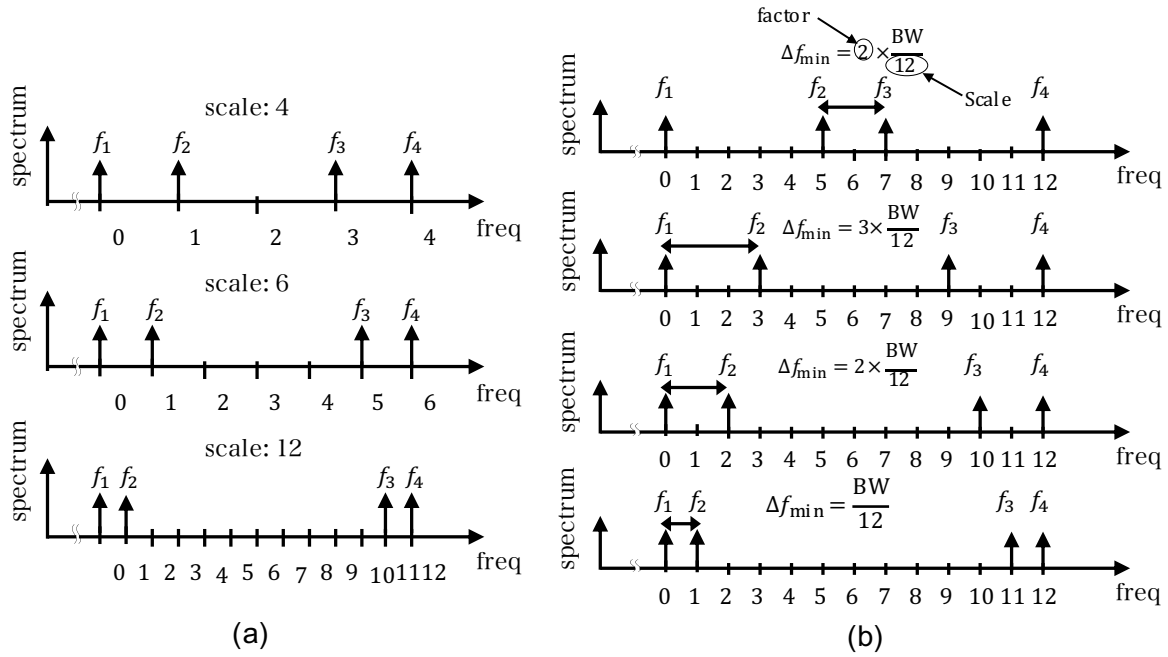

Fig. 4.6: Scale explanation. As the number of scale increases, the minimum frequency spacing between the adjacent tones decreases.

always placed at each end, separated by BW and cannot be arranged in other places. In Fig. 4.6, all the cases represent $\Delta f(1,2) = \Delta f(3,4) \wedge \Delta f(1,3) = \Delta f(2,4)$, for each *Scale* as an example.

When the *Scale* is 4, the f_{scale} becomes $BW/4$, so the communication rate is increased as the f_{min} increases. However, in such a case, all the possible candidate tone configurations are reduced to only 3: (0, 1, 3, 4), (0, 1, 2, 4), and (0, 2, 3, 4) whose types of the tone configurations are $\Delta f(1,2) = \Delta f(3,4) \wedge \Delta f(1,3) = \Delta f(2,4)$, $\Delta f(1,2) = \Delta f(2,3) \wedge \Delta f(1,3) = \Delta f(3,4)$, and $\Delta f(2,3) = \Delta f(3,4) \wedge \Delta f(1,2) = \Delta f(2,4)$, respectively. Note here that each element stands for the index in the frequency domain in Fig. 4.6. Since these types of the tone configurations all belong to Category B, it cannot send a bit of information in this case because all the outputs fall into the same value without being differentiated.

On the other hand, when the *Scale* is 12, Δf_{scale} becomes $BW/12$. Therefore, the tone combinations increase significantly. As it can be seen from Fig. 4.6 (a). at the bottom, there

Table 4.2: The number of types of the tone configurations which is shown in Fig. 4.4, and the number of possible candidate tone configurations for the case of $N = 4$ ($Scale = 12$).

categories	Number of Types of tone configurations	Number of possible tone configurations
Category A	1	34
Category B	4	14
Category C	3	6
Category D	1	1

are 11 places for the second and third tones to be arranged (indexes 1 to 11). Note that the 1st and the last tones are always placed at each end, separated by BW and cannot be arranged in other places. I show the number of tone configurations for each category in Table 4.2. From the table, there are 34, 14, 6, and 1 possible tone configurations of the frequency tones that belong to categories A, B, C, and D, respectively. The 14 possible tone configurations in the Category B yield the same PAPR values, and they are categorized into 4 types, as shown in Fig 4.4.

At the same time, the number of tone configurations that belong to the same types is also increased. These tone configurations include different *factor*. I show the example of the case of different tone arrangements whose types of tone configurations ($\Delta f(1,2) = \Delta f(3,4) \wedge \Delta f(2,4) = \Delta f(1,3)$) are all the same in Fig. 4.6 (b). As in Fig. 4.6 (b), there are 4 different tone configurations to be considered ((0, 5, 7, 12), (0, 3, 9, 12), (0, 2, 10, 12), and (0, 1, 11, 12)). Note that (0, 4, 8, 12) is in Category A because all the tones are evenly distributed, so this case is omitted. Any of these tones fall into the Category B. The differences are that they have different *factor*s, which are 2, 3, 2, and 1, respectively. In order to obtain a faster communication rate, $\Delta f_{\min}$ needs to be large. In that perspective, (0, 3, 9, 12) is the tone configuration whose minimum frequency spacing is the largest. The maximum value of *factor* differs from the categories. Based on the brute force search, I found the values of maximum *factor*s for each category as 4, 3, 2, and 3 from categories A to D respectively. Since the communication rate is rate-limited to the slowest $f_{\min}$, the communication rate for

Table 4.3: Relations of Δf_{scale}, *factor*, Δf_{min} for different N

N	3	4	5	6	7
# of possible PAPRs	2	4	7	11	16
Δf_{scale}	$\frac{BW}{4}$	$\frac{BW}{6}$	$\frac{BW}{12}$	$\frac{BW}{30}$	$\frac{BW}{48}$
factor	1	1	1	4	5
Δf_{min}	$\frac{BW}{4}$	$\frac{BW}{6}$	$\frac{BW}{12}$	$\frac{2BW}{15}$	$\frac{5BW}{48}$

the case of this example becomes, $R = \log_2(4) \times \frac{2\times BW}{12} = \frac{BW}{3}$. Here, since 4 categories exist for this example, the modulation order is obtained as $M = \log_2(4)$.

The optimal case can be defined as the minimum *Scale* that at least one candidate set exists for each category, which in this case, *Scale* = 6. In such a case, the number of types for each category is 1, 1, 6, and 2 from categories A to D respectively. By reducing the *Scale*, it is possible to find candidate tone configurations for symbols with smaller search space as well. The total candidate tone configurations are reduced to 10 from 55 when the scale is 12.

Larger Number of Tones

Obtaining a suitable *Scale* analytically for a given number of N is difficult. Therefore, I solved this by brute force search. I tested with a small value to see if the candidate tone configurations included all the categories. Based on the brute force search, I obtained the Δf_{scale}, Δf_{factor}, and Δf_{min} for different N from 3 up to 7, which is shown in Table 4.3. Since increasing the number of N requires a huge search space, I was unable to find a suitable *Scale* for $N > 7$ due to the limitation of computational resources. As can be seen, up to $N = 5$, *factor* becomes 1, which means that there exist at least one category whose factor is 1. On the other hand, for $N > 5$, the minimum scale becomes 4 for $N = 6$, and 5 for $N = 7$, which indicates that by carefully choosing the specific tone combinations, it is possible to have the tone combinations that can

Table 4.4: The tone features depending on the categories for $N = 3$ and $Scale = 4$.

	types of tone configurations	the number of equals	factors	number of configurations	candidate configurations
Category A	$\Delta f(1,2) = \Delta f(2,3)$	1	2	1	(0, 2, 4).
Category B	no features	0	1	2	(0, 1, 4), (0, 3, 4).

Table 4.5: The tone features depending on the categories for $N = 4$ and $Scale = 6$.

	types of tone configurations	the number of equals	factors	number of configurations	candidate configurations
Category A	$\Delta f(1,2) = \Delta f(2,3) = \Delta f(3,4) \wedge$ $\Delta f(1,3) = \Delta f(2,4)$	3	2	1	(0, 2, 4, 6).
Category B	$\Delta f(1,2) = \Delta f(3,4) \wedge \Delta f(1,3) = \Delta f(2,4)$	2	1	1	(0, 1, 5, 6).
Category C	$\Delta f(1,2) = \Delta f(2,3) \vee$ $\Delta f(1,2) = \Delta f(2,4) \vee$ $\Delta f(1,3) = \Delta f(3,4) \vee$ $\Delta f(2,3) = \Delta f(3,4)$	1	1	6	(0, 1, 2, 6), (0, 1, 3, 6), (0, 2, 3, 6), (0, 3, 4, 6), (0, 3, 5, 6), (0, 4, 5, 6).
Category D	No features	0	1	2	(0, 1, 4, 6), (0, 2, 5, 6).

increase the communication rate.

I show the detailed results for the case of $N = 3$, $N = 4$, and $N = 5$ in Table 4.4 – Table 4.6. In the tables, I show the types of tone configurations, the number of equals, the largest factor among the tone configurations, the number of combinations, and the actual candidate set examples that resulted the fastest for each category. These results were obtained by considering all the possible cases and categorizing them analytically. Note that for $N = 5$, there are a lot of types to be considered, so I show only part of the results. Each *factor* in Table 4.4 – Table 4.6 is the *factor* within the categories and the *factor* that is listed in Table 4.3 is the minimum value among categories. This is because the minimum value of the *factor* among the categories is rate-limited in terms of communication rate.

I compared the spectrum efficiency with the most related papers in Fig. 4.7, which shows that my case achieves the poorest performances. The spectrum efficiencies of the other schemes were calculated based on the results in their papers [99, 67]. The spectral efficiency becomes 4 times smaller than the conventional multitone FSK method. In addition, I see that there is a slight degradation against PAPR based multitone SWIPT as well when N is a small value. However, as the number of tones is increased, the efficiency improves and comes close to the multitone-PAPR method. In fact, as shown in Fig. 4.5, increasing the number of tones

Table 4.6: The tone features depending on the categories for $N = 5$ and $Scale = 12$.

	types of tone configurations	the number of equals	factors	number of configurations	candidate configurations
Category A	$\Delta f(1,2) = \Delta f(2,3) = \Delta f(3,4) = \Delta f(4,5) \wedge$ $\Delta f(1,3) = \Delta f(2,4) = \Delta f(3,5) \wedge$ $\Delta f(1,4) = \Delta f(2,5)$	6	3	1	(0, 3, 6, 9, 12).
Category B	$\Delta f(1,2) = \Delta f(2,4) = \Delta f(4,5) \wedge$ $\Delta f(1,3) = \Delta f(3,5) \wedge$ $\Delta f(1,4) = \Delta f(2,5) \wedge$ $\Delta f(2,3) = \Delta f(3,4)$	5	2	1	(0, 4, 6, 8, 12).
Category C	$\Delta f(1,2) = \Delta f(2,3) = \Delta f(3,4) \wedge$ $\Delta f(1,3) = \Delta f(2,4) \wedge$ $\Delta f(1,4) = \Delta f(4,5)$, ...	4	2	11	(0, 2, 4, 6, 12), (0, 4, 6, 10, 12), (0, 6, 8, 10, 12) ..., (8 more).
Category D	$\Delta f(1,2) = \Delta f(4,5) \wedge$ $\Delta f(1,4) = \Delta f(2,5) \wedge$ $\Delta f(1,3) = \Delta f(3,4)$, ...	3	2	6	(0, 2, 5, 10, 12), (0, 3, 5, 7, 12), (0, 5, 7, 9, 12), ... (3 more)
Category E	$\Delta f(1,2) = \Delta f(2,3) \wedge$ $\Delta f(2,4) = \Delta f(4,5)$, ...	2	2	12	(0, 2, 4, 7, 12), (0, 3, 5, 8, 12), ..., (10 more)
Category F	$\Delta f(1,2) = \Delta f(2,3) \vee$ $\Delta f(2,3) = \Delta f(3,4) \vee$ $\Delta f(3,4) = \Delta f(4,5) \vee$ $\Delta f(2,3) = \Delta f(3,4) \vee$	1	2	4	(0, 2, 4, 9, 12), (0, 2, 5, 8, 12), (0, 3, 8, 10, 12), (0, 4, 7, 10, 12).
Category G	no features	0	1	14	(0, 1, 3, 7, 12), ... (13 more).

results in having a larger modulation order than the multitone-PAPR case. Therefore, for a larger N, I could obtain a better performance against the multitone-PAPR method. Note that my scheme stands for the fastest configuration whose tone combinations are selected from Table 4.4 – 4.6.

Finally, I discuss the difference between the aforementioned tone selections and the previously published multitone FSK SWIPT method [67]. As opposed to the conventional method where the tones are selected so that each IM2 from the tone combinations are different, my method selects the combinations of tone configurations whose numbers of equal values in the IM2s generated from the combinations, are different. Borrowing the expressions from [67], the tone combinations include both uniform and nonuniform multitone FSK, which is also one of the differences. While the previous paper reports the possibility to consider more varieties of selections, I constrained the total bandwidth to be the same in order to make the choice of

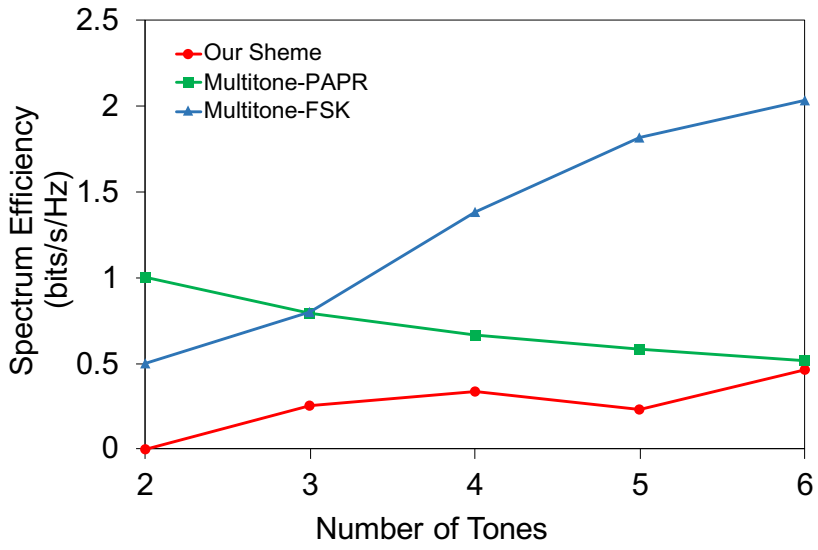

Fig. 4.7: Spectrum efficiency comparison; These results are refereed from the results of previous papers.

tone selection easier. This results in degrading the spectral efficiency.

4.4 Design Receiver System and Simulation Validations

Based on the previous results, I was able to encode bits based on the frequency tone arrangements. In this section, I validate my method using the SWIPT receiver, which consists of both information decoding units and the energy harvesting unit. The design requirement is that the SWIPT receiver should both receive RF energy harvesting power and RF signal simultaneously using the same antenna. In addition, I assumed that the receiver circuit has very low power computational resources.

4.4.1 Receiver System Model

The block diagram of the tested rectifier circuit to achieve SWIPT is shown in Fig. 4.8. It consists of two units; the first unit is for obtaining RF energy, which works as a battery source for the receiver circuit. The second rectifier unit works for obtaining PAPR by observing the peak voltage and the averaged voltage. I connected these units after the matching network.

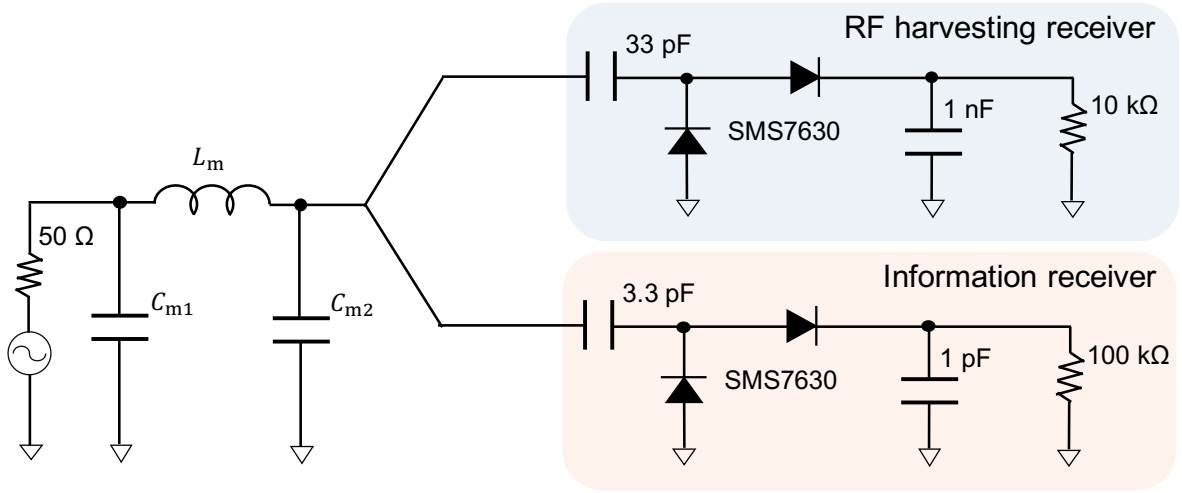

Fig. 4.8: The circuit model for ADS circuit simulation and experiment. The impedance was matched using an optimization tool in ADS. The received signal is split into two units; one is for the RF harvesting receiver (top), and the other is for calculating PAPRs. Both of the modules consists of passive elements.

Note that by changing the DC block capacitors for each unit, I would change the RF input power so that more power may flow into the energy harvesting unit [2]. I will refer to this two-unit type rectifier as a 2 stream rectifier and the rectifier design shown in Fig. 4.2 as a single-stream rectifier in later discussions.

4.4.2 PAPR Measurement Validation

I conducted simulations and experiments in order to see if the presented receiver circuit could successfully distinguish PAPR differences based on the previously showed signal generation method. The simulation and experiment setup is the same as that described in section 4.2.3. Note that the impedance matching was optimized to -10 dBm and did not rematch even with different input power since in a usual receiver system, changing the matching network depending on its input power is not practical. The layout and the manufactured SWIPT circuit are shown in Fig. 4.9.

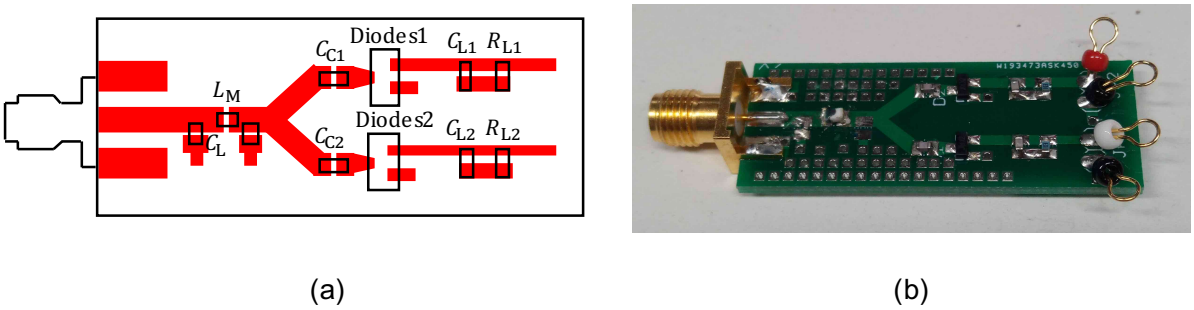

Fig. 4.9: (a). Layout of the SWIPT rectifier for the experiment. All the tested rectifiers are implemented using this layout. (b). The manufactured SWIPT circuit.

PAPR Performance Characterization against Input Power

For the tone selections, I utilized some of the tones from Table 4.4 - Table 4.6. If the candidate sets included multiple sets, I averaged the output PAPR of all the tested cases. The input power was set to -10 dBm, the communication bandwidth was fixed to 200 kHz, and the center frequency was set to 915 MHz. The output PAPR was derived based on the equation (**??**). I show the simulation and experimental results in Fig. 4.10 (a) and (b) for $N = 3$ and 4, respectively. Both experimental and simulation results show that I was able to distinguish $(N-1)(N-2)/2+1$ different combinations. However, for the experimental results, the PAPR value became unstable for power lower than -18 dBm. When the obtained output voltage was too small and the obtained peak voltage was relatively high, the peak to average power raised significantly. This resulted in unstable PAPRs when the low input powers were induced. Therefore, it is hard to use in practice for such small input power. In spite of this result, the typical energy harvesting receiver commercially available requires more than -12 dBm input power for its operation, so operating above -18 dBm is feasible for practical use [141].

Another thing to express is that the PAPR values change depending on the input power level within the same category. This means that even if the receiver device obtains a specific PAPR value, it cannot correctly identify which category it is in. For example, when the receiver device receives the $N = 4$ tone waveforms and receives output PAPR that is indicated as 8, the system cannot decide which category does the tone configuration of the transmitted

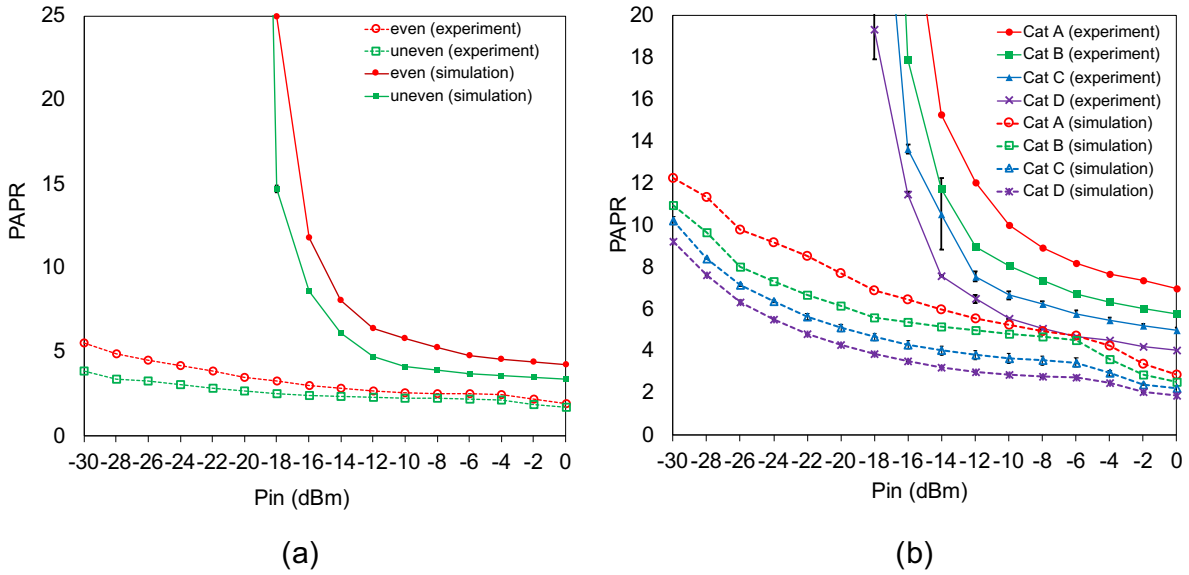

Fig. 4.10: Simulation results of PAPR comparison based on the categories in Table 4.4 for $N = 3$ with the introduced receiver circuit.

waveforms belongs to unless the receiver device obtained received power as well. This occurs because Category A with input power -6 dBm, Category B with input power -10 dBm, Category C with input power -12.2 dBm, and Category D with input power -14.1 dBm all output PAPR values of 8. Therefore, in order to utilize this scheme, it is required to have an initial reference signal used to measure the received power at the receiver node. Simply put, the transmitter device sends the preambles of all the categories at first so that the receiver can understand the mapping between the PAPR values and the categories. One might say that input power level changes depending on the timing of the transmitted signal. However, in a case where the transmitter and receiver nodes are in fixed places, the input power level would not change unless the wireless channel changes dramatically, like in an urban city. Therefore, assuming that in a rural area, where the wireless channel would not change dramatically, I could assume that the wireless channel might be fixed for a short period of time, which is enough time for the receiver node to receive information.

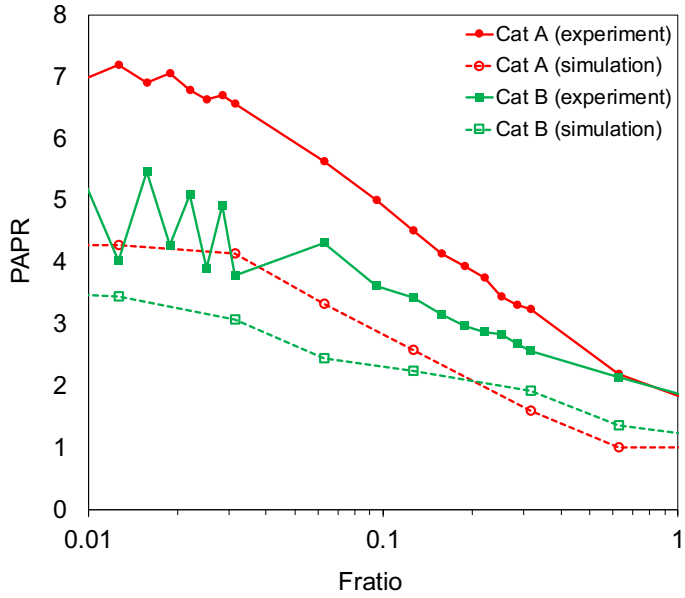

Fig. 4.11: Simulation and experimental results of PAPR comparisons against F_{ratio} for $N = 3$. The tested rectifier was the 2 stream rectifier that is shown in Fig. 5.2 and the BW was varied from 10 kHz to 1 MHz. The input power was set to -10 dBm.

PAPR Performance Characterization against F_{ratio}

I further investigate the PAPR difference against F_{ratio} for the case of $N = 3$, whose result is shown in Fig. 4.11. The tested receiver circuit is the same as in Fig. 4.8. I varied the bandwidth from 10 kHz to 1 MHz, which corresponds to F_{ratio} of 0.01 to 1. From Fig. 4.11, the PAPR difference between the categories A and B in Table 4.4 becomes smaller for larger F_{ratio}. When larger bandwidth is allocated, the generated IM2s are more likely to go beyond the F_{ratio} in the frequency domain, which results in having smaller AC components in the output voltage. Therefore, the output voltage fluctuation between the categories resembles each other. That is to say, my system fails to retrieve information for a larger bandwidth or a lower RC factor, which resembles the results from a single-stream rectifier in Fig. 4.3 (b). Note that I am assuming the use of this system to be for the UHF regime. In such a regime, the required bandwidth is at most 200 kHz, which is relatively small. As discussed in section 4.2.4, even though my method works with a small F_{ratio} regime, my method is enough for

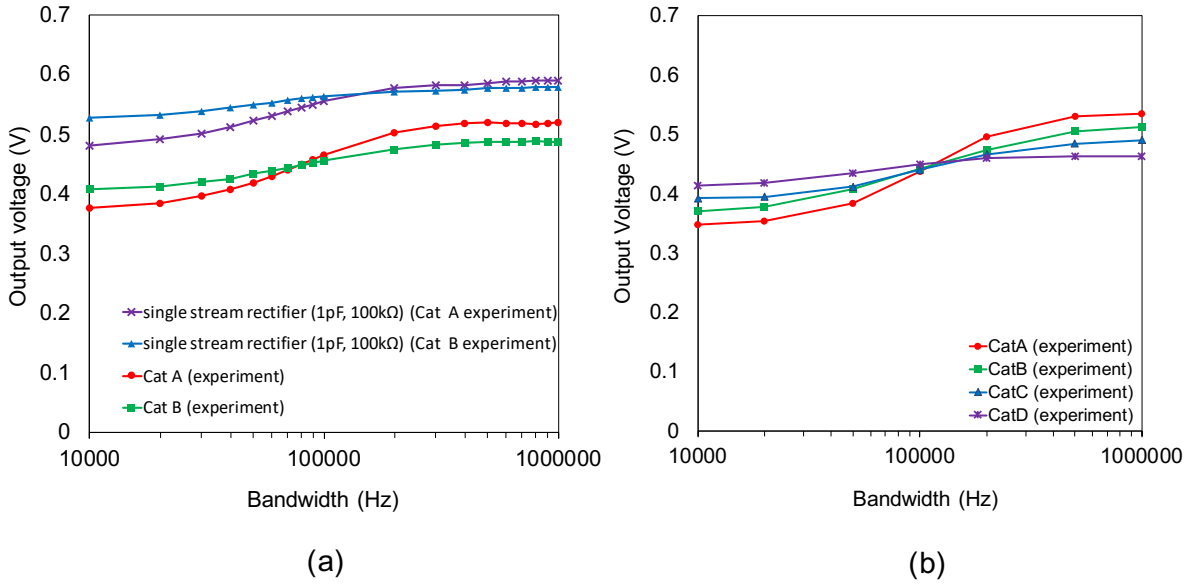

Fig. 4.12: Output voltage comparisons against bandwidth for (a). $N = 3$ and (b). $N = 4$. The tested rectifier was the 2 stream rectifier that is shown in Fig. 5.2, and the output voltage was inspected from the main RF unit. A single rectifier circuit was also tested for the case of (a). whose load resistance was 1 nF and 10 kΩ. The tested bandwidth was varied from 10 kHz to 1 MHz, and input power was set to -10 dBm.

operating at UHF. On the other hand, when I consider using this method to the system where the communication bandwidth can be much larger than my assumption, my method is not suitable for adoption. In such scenarios, the previously published method is beneficial for information retrieving [67].

PAPR Performance Characterization against F_{ratio}

Finally, I compare the output voltage acquisitions of the main RF harvesting unit. The experimental result of the output voltage from the main RF harvesting unit of the 2 stream type rectifier is shown in Fig. 4.12 (a). In addition, I compare it with the single-stream type rectifier shown in Fig. 4.3, whose load resistance and capacitance were 10 kΩ, and 1 nF for $N = 3$. The input power was set to -10 dBm, and bandwidth was varied from 10 kHz to 1 MHz. In terms of F_{ratio}, it corresponded to 0.6 to 62. This range is different from the aforementioned

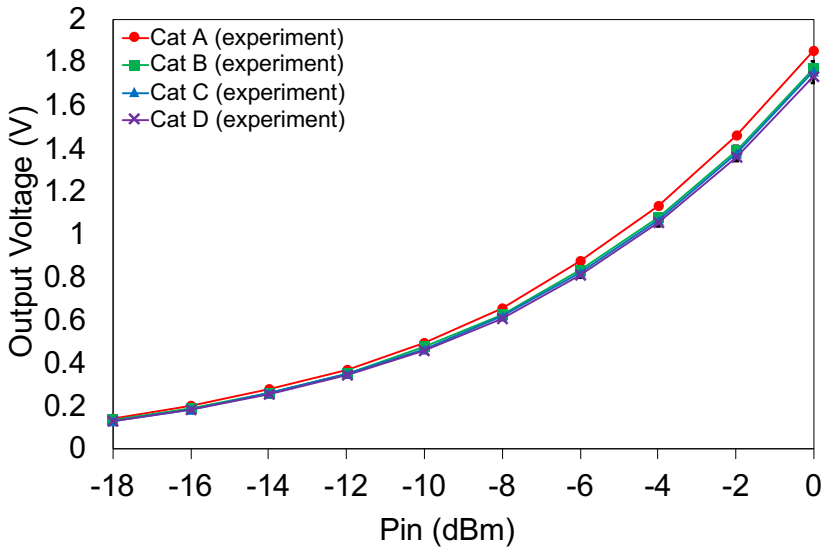

Fig. 4.13: Experimental results of output voltage comparisons against input power for $N = 4$. The input power was varied from -18 to 0 dBm, and the bandwidth was set to 200 kHz. The tested rectifier was the 2 stream rectifier that is shown in Fig. 5.2, and the output voltage was inspected from the main RF unit.

analysis due to the fact that the Δf_{cutoff} is different from those at the information unit. The experimental results show that increasing the bandwidth to some extent results in having higher output voltages in both the 2 stream rectifier case and the single-stream case. When higher bandwidth is allocated, the ripple of the output voltage ceases due to the RC filter effect, resulting in higher output voltages. On the other hand, when the bandwidth is small, the RC filter cannot cutoff the IM2 tones. In such case, the output voltage drops significantly during the negative half cycle of the waveforms, which causes the degradation of WPT performances especially for the case of a voltage doubler rectifier [116]. Comparing the single stream and the 2 streams case, the single-stream case rectifier yields better output voltage performance. This is due to the loss caused by separating the transmission line to the information unit, which consumes some amount of power.

Furthermore, the experiments show that the output voltages for the case of categories A and B flip when higher bandwidth is allocated. This shows that for evenly distributed cases (Category A) when the cutoff frequency cannot slice IM2 tones, severe performance

Table 4.7: Performance Summary

Method	Efficiency	Input power range	carrier frequency	number of tones	calculation cost (summation, multiplication)
Multitone PAPR [140, 99]	8% to 14% at −10 dBm	−20 dBm to 15 dBm	900 MHz	4	$O(N)$, $O(N)$
Multitone FSK [67]	7% to 9% at −5 dBm	−30 dBm to 0 dBm	2.45 GHz	4	$O(N\log N)$, $O(N\log N)$
Biased ASK [98]	22% to 28% at −15 dBm	−25 dBm to −5 dBm	2.45 GHz	2	$O(N)$, $O(1)$
Amplitude / Phase [66]	46% to 52% at −10 dBm	−20 dBm to −6 dBm	650 MHz to 1 GHz	2	$O(N)$, $O(1)$
This work	21% to 25% at −10 dBm	−20 dBm to 0 dBm	915 MHz	4	$O(N)$, $O(1)$

degradation occurs at the output voltage. It is also indicated that when the tones are unevenly distributed, even with the RC filter cutoff AC component of the output voltage, the yielded output voltage cannot improve similarly to the evenly distributed case. This corresponds to the fact that evenly distributed multitone waveforms can maximize the output voltage [83]. The results reveal that multitone waveforms with evenly distributed waveforms always yield the highest output voltage under the conditions that allocated bandwidth must be large enough. Investigating the tradeoff between the bandwidth and the tone arrangements is the future works since it is out of the scope of this paper.

I also compare the output voltage for the case when $N = 4$ in Fig. 4.12 (a), which behaves similarly to the case when $N = 3$. Increasing the number of tones results in having larger differences in terms of the voltage acquisition results from categories A and D, except for the case when the bandwidth reaches 100 kHz. It also shows that on one hand, it is required to allocate larger bandwidth or higher F_{ratio}, but on the other hand, in order to get better communication performance, F_{ratio}, should be small enough to distinguish the PAPR difference between the categories, which is also indicated in previous papers [67, 66]. Thus, F_{cutoff} needs to be designed properly for both the RF harvesting unit and the information unit. Finally, in Fig. 4.13 I show the results for different input power. The bandwidth was set to 200 kHz. As it can be seen from the result, by increasing the input power results in larger differences between the categories in terms of output voltages.

4.4.3 Optimizations

In the previous paper, due to the design of the receiver circuit, when the LP-filter is very narrow, the IM2s in the transmitted tones that reside far away from the DC region are attenuated. This results in detection errors because some of the tones are missed while detecting in the frequency domain. In order to tackle this problem, the previous paper [67], has dealt with pre and post optimizations, which are done at the transmitter and receiver side, respectively. These optimizations are executed based on the knowledge of the transfer function of the LP-filter at the receiver circuit and by multiplying the scaling factor of the waveforms.

In my system, it may be possible to implement such optimizations at both sides, but these optimizations suppress the communication rate eventually. This is because I fix the entire communication bandwidth for each tone configuration in order to make the system easier to select tones. As a result, the furthest IM2 tone generated from the candidate set is BW away from the DC region. If the BW happens to be larger than F_{cutoff}, signal detection errors will be prone to occur. In such a scenario, either BW or F_{cutoff} needs to be controlled so that BW becomes smaller than F_{cutoff}. Since the circuit parameter is not easily controlled, BW needs to be small. This results in degrading the communication rate.

Overall, in the perspectives of the pre and post optimizations, my system has less flexibility compared to the conventional FSK method due to the adoption of fixed bandwidth for tone selections. Finding a method to select tones from unfixed bandwidth conditions might be the future research direction.

4.5 Discussions

Overall, I have investigated the PAPR detection based multitone FSK. In this section I discuss the comparison with the conventional methods and the feasibility of optimizations that have been discussed in [67].

The advantage of my method relies on the fact that it can eliminate the FFT calculation and rely on a PAPR based method performed on the time domain. Typically, the calculation cost of FFT requires $O(N \log N)$ for multiplications and summations while the PAPR based

calculation requires $O(1)$ for multiplications and $O(N)$ for summations using the big-O notation. Therefore, in terms of the calculation cost, it is more applicable for a battery-less device. As also discussed in the introduction, the conventional method can implement passive filter banks in order to avoid the calculation of FFT to obtain information [67]. However, when I implement at UHF where the communication bandwidth lies typically below 1 MHz, it is hard to make a filter that can separate tones whose frequency spacing is around 1 MHz due to the requirement of a high Q factor. Therefore, even under the uniform FSK case, it is quite challenging to design such filters. It is also possible to implement the filter after the rectification process. However, in such case, the system must embed roughly the same amount of filters as the symbol index. Therefore, trade-off between the size of the receiver circuit and the modulation order needs to be considered. On the other hand, there are also disadvantages from the perspectives of interference or flexibility against the structures.

In terms of interference duration, the conventional method can post compensate the channel effect as they have shown by calculating and negating the channel effect. In addition, in the former paper, signals can be detected even with a small input power (typically around -30 dBm receive power) since it can inspect the spectrum using FFTs [67]. On the other hand in my system, based on the results, -18 dBm received power level is the minimum threshold for the device to correctly detect signals even under the non-interfered condition. Therefore, I conclude that under interference, my system is inferior to the conventional method. Note that the same discussion could be made for noise duration. However, typically, the microwave power transfer signal is significantly above the noise level, so this infers that there is no difference between the method in terms of noise.

As discussed in the previous section, the conventional method is more flexible with regard to the receiver structure since their method can pre or post optimize the waveform depending on the LP-filter at the receiver side. In order to select tone configurations more simply, I fixed the total bandwidth for each condition which in turn hinders optimization. Even though I could do pre-optimization so as not to be affected by the LP-filter, the communication rate deteriorates severely due to this operation.

Finally, I compared the performances with existing papers [140, 99, 67, 98, 66] in Table

4.7. The calculated values are based on the reported results in each paper. Compared with the Multitone FSK, the computational cost is significantly reduced which result from eliminating the calculation o FFT and utilizing PAPR measurement [67]. In addition, I was also able to reduce the calculation complexity against conventional multitone PAPR method. The conventional method calculates average power in order to obtain PAPRs whereas in my case, I only need to measure average output voltage and calculate the power after that, which indicates that multiplication occurs only one time per symbol for obtaining average power [140]. Although modulation based on amplitude or phase controlling method [66] gained the highest efficiency, the modulation method is too complex to be employed for $N > 3$. In my case, the efficiencies varies from 21% to 25% for the case when the number of tones were 4 and the input power range varied from -20 dBm to 0 dBm, which is feasible as I discussed in section. 4.4.2.

4.6 Summary

In this chapter, a frequency shift-type multitone signal SWIPT system based on the PAPR detection method is introduced. Different from FFT based signal detection, my method realizes signal detection more simply. I revealed that when the tones vary, the contents of frequency tones in the output voltage varies due to the diode's nonlinearity. In addition, I formulated the relation between the number of tones and the modulation orders and verified it using ADS circuit simulation as well as experiments with my introduced receiver circuit. Based on the results, I could distinguish the $\frac{(N-1)(N-2)}{2} + 1$ different PAPRs for $N = 3$, and $N = 4$, which corresponded to my formula. The limitation of my method is with power values under -18 dBm, the PAPR differences are no longer detected.

CHAPTER 5

CONCLUSIONS

5.1 The main contributions of this thesis

In this thesis, waveform design using multitone waveforms have been investigated in order to improve the operation range of battery-less devices as well as to transmit information and power simultaneously. The contributions of this thesis is as follows;

- Waveform designs for improving the performance of PCEs were proposed. The experiments showed that there exists saturation points in the frequency domain which indicates that the multitone waveforms have to allocate necessary frequency spacing in order to achieve better PCEs. In addition, the saturation points can be controlled primarily by the storage capacitances. For these findings, the necessary frequency spacings and the number of tones were suggested based on the parameters of the rectifiers. These characteristics agree with the wire and wireless transmission experiments. However,

when experiment with wireless transmissions, the bandwidth limitations of antennas are observed, which makes the design instructions to be modified.

- Waveform designs for improving the performance of sensitivities or peak voltage acquisitions were proposed. The effect of the frequency spacing of multitone waveforms in terms of rectifiers' sensitivities for voltage-doubler type rectifiers in the UHF band was revealed. In contrast to the PCE cases, the saturation point of peak voltage acquisitions exist approximately 100 times smaller than the saturation point of PCEs and the necessary frequency spacings need to be smaller than the saturation points of peak voltage acquisitions, which indicates that the design guideline for improving PCEs and peak voltage acquisitions were totally different. The experiments were conducted not only with simple rectifiers, but with receiver circuit that can be obtained commercially to see the effect of this guideline.

- Waveform designs for enabling the transmission of power and information simultaneously using multitone waveforms was proposed. The waveforms are frequency shift-type multitone and the output PAPRs are measured for information detection. This process can reduce the need of the FFT operations that have been required for the conventional methods. The principles of how frequency shift tones change the PAPRs at the receiver side were revealed and demonstrated through simulation and experiments. The distinguishable output PAPRs were estimated to $\frac{(N-1)(N-2)}{2} + 1$ and based on the experiments, this scheme can be operated with the minimum input of -18 dBm power.

5.2 Future Works

The future works related to this thesis are the following.

5.2.1 PCE or Peak Output Voltage Improvement of Using Multitone Waveforms

Theoretical realizations of waveform designs

This thesis mainly focused on the realizations to design better PCE or sensitivity performances through exhaustive experiments and simulation for voltage doubler-type rectifiers. However, when the types of the rectifier change it requires another experiments for corresponding rectifiers which is cumbersome to do. In order to systematically achieve these realizations, theoretical analysis should be explored. However, because of the difficulties of analyzing rectifiers reside in their nonlinear behaviors. Some works have shown the abilities of analyzing these rectifier behaviors for single diode rectifiers, but no other literature has achieved with rectifiers with more than one diode at this point. It might be required some approximations, but analytical realizations should be one of the research areas that will be explored in the future. One of the straight forward ways are to expand all the components of the rectifiers to elements (capacitors, inductors, or resistors) and see the transfer functions of them. This maybe one of the first steps to go through.

Other Diode Effectivities

Recently, the use of tunnel diodes have been widely used in spite of the difficulties of obtaining the manufactured ones. The behaviors of such diodes have some differences from schottky diodes, which might be required for designing waveforms. Most of the cases, these diodes will be used as a way to increase the sensitivities or to increase the backscatter waveforms, when designing the waveforms one might be wanted to design in order to increase these natures (sensitivities or backscatter capabilities).

Noise and Wireless Channel Effect

Although I have tested the additive white Gaussian noise (AWGN) channel conditions assuming that the wireless channel is flat. However, for more practical situation, channel might be more frequency selective. In addition, when considering the combination between the multiple-input multiple-output (MIMO) technique and the multitone technique, the channel

effect becomes very important since the beam forming technique requires to have CSIs [88, 142]. Therefore, exploring the effect of channel needs to be investigated. There are several related works with this topic, so how the experimental results align with the existing works also are interesting to see [56].

The Effect of Transmitter Nonlinearity

In this thesis, I assume the transmitter nonlinearity as optimal. However, in reality, the transmitter has amplifier has saturation region, so transmitting extremely high PAPR signals are distorted before traversing in the air. Therefore, the number of tones are needs to be carefully selected when considering the nonlinearity of the transmitter side or to apply some predistortion method used in MIMO techniques [143, 144].

Modeling with Multiple Elements

Despite the fact that I modeled using individual parameters, it can be achievable to model the suitable waveforms using different parameters such as load resistances and capacitances. In fact, it is natural to think that the output voltages are affected by the output load resistance and storage capacitance although the weight of the effectiveness is different. One could think the 2 stage model, where the first stage can be determined by the cutoff frequency formed by the storage capacitance and diode parasitic resistance, and the second stage behavior can be determined by the load resistance and the storage capacitance. Based on the experiments, the effect of the load resistance is increased. Specifically, when the load resistance becomes smaller, the PCE characteristics lean toward the right at the frequency domain or calming. This indicates that the load resistance especially when it is small, the PCE performances were affected in no small part. Therefore, the second stage might be some form of RC cutoff filter determined by the load resistance and the storage capacitance.

Low Power Feedback Method

When designing waveforms, it is crucial to understand the receivers' storage capacitances and the load resistances. Currently, these values are given at the transmitter side, but when it

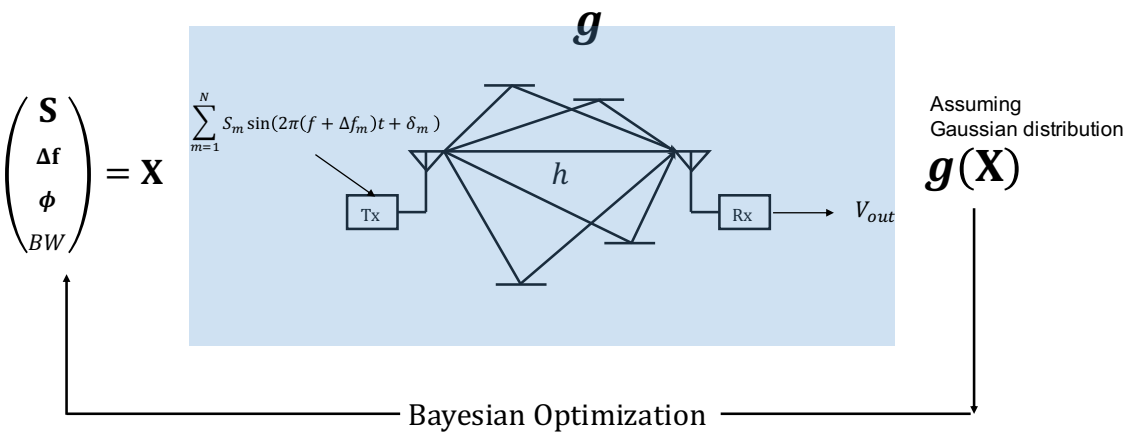

Fig. 5.1: The system model for Bayesian Optimization method is shown. Input value **X** is generated based on Bayesian optimization algorithm which learns a wireless channel in between the transmitter side and the receiver side, rectifiers' condition (antenna characteristics, matching network, and rectifier topologies). It learns by seeing rectified voltage as a key that is feed back from receiver side which I assume backscatter technology, but in this implementation, I did not implement the backscatter communication feedback.

comes to implement, it is becoming required to feedback in some way with low power. One of the naive solutions is that the receiver backscatter these values when the power probe signal is transmitted from the source. Given that backscatter signal, the transmitter can design the waveforms according to it.

5.2.2 Multitone Waveform Optimizations Using Bayesian Optimizations

One of the solutions for the aforementioned future challenges is to design the optimal waveforms through learning method. This method is promising because the learning system can understand the saturation due to the amplifier at the transmitter, wireless channels, and the parameters of the receiver devices. In order to learn them, it is required to feedback the knowledge about the wireless channels and the receiver parameters from receiver to transmitter either explicitly or implicitly feedback [145]. Unlike explicit feedback where a receiver has to calculate channel state information out of pilot signals from the transmitter side, the

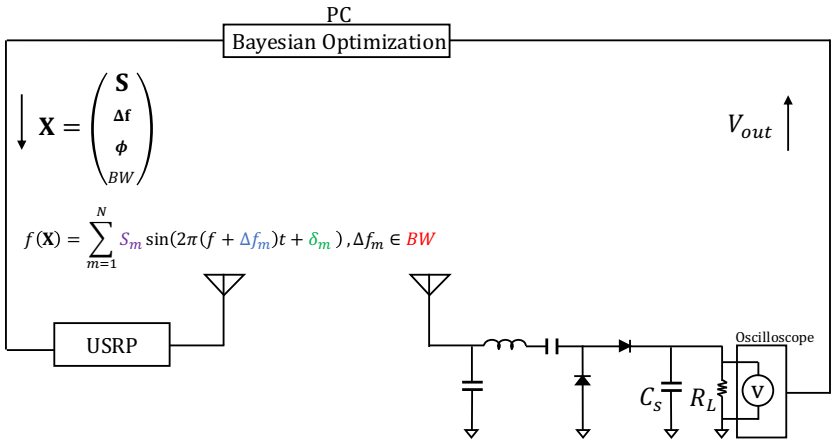

Fig. 5.2: Example experimental setup is shown. It consists of amplitudes, phases for each number of subcarriers N, and bandwidth(BW); all of which is represented by an input vector $\mathbf{X}$. $f(\mathbf{X})$ represents transmit signal. I aim to maximize the rectified voltage V_{out} using Bayesian Optimization algorithm.

receiver sends a pilot signal to the transmitter so that all the necessary calculation are pushed to transmitter side for implicit feedback [145, 146]. For the case of battery-free devices, implicit feedback needs to be done through backscatter communication which piggybacks incoming signals and modulates onto it though simply changing antenna impedance by switching. Therefore, actively sending feedback to a transmitter side that has been explored in some of the existing paper may not be practical for battery-less devices to achieve [86, 147, 148].

One of the promising feedback method is to use the received signal strength indicator (RSSI) for a feedback, and transmitter side iteratively updates the coefficient of beamforming vectors [149, 150, 151]. While this method eliminates a significant amount of energy, however, acquiring RSSI still require a large amount of energy for battery-free devices, which could shorten the working range of them. In [152], an energy-efficient method has been proposed where the transmitter side determine beamforming vectors by seeing the reflected signal from receiver devices. In this way, receiver devices do not require energy for calibration. However, these methods have been introduced for realizing the beamforming technique where a system tries to increase the received power, I am aiming to increase rectified voltage or power conversion efficiency. Because the system needs to deal with nonlinearities, PCE should be changed even with the same input power.

Therefore, one can utilize a Bayesian estimation method to blindly harvest energy so that power harvester adaptively update condition of waveform generation. Also, I use rectified voltage as a key to learning. This does not require power hungry operational amplifier that is included in RSSI, which could potentially save power. Moreover, utilizing rectified voltage means that I could update a better waveform depending on rectifier topology. As opposed to RSSI which just see power level at the receiver side front end, seeing rectified voltage interpret internal receiver circuit, matching network, antenna bandwidth, rectifier topology, load resistance and so forth. Updating transmit waveforms based on these nonlinear behaviors just by watching RSSI might not be enough for the measurement.

System Model for Promising Bayesian Estimation Approach

The system block of the example system is shown in Fig. 5.1. An inputs for a transmit signal is generated based on Bayesian Optimization, which uses a rectified voltage as a feedback in order to improve waveforms. Let input parameters are denoted as $\mathbf{X}$. Bayesian optimization optimize can be realized as following;

$$\max_{\mathbf{X}} g(\mathbf{X}), \tag{5.1}$$

where g is assumed to be Gaussian distribution, which represents a system of the channel between the transmitter side and the receiver side and rectification process at the receiver side for this case.

In order to find a new point $\mathbf{x}$, Expected Improvement can be utilized. Expected improvement finds a new $\mathbf{x}$ based on previously observed pairs of inputs and outputs and expectations of output value for each candidate inputs [153]. Assuming that k different pairs of $\mathbf{X}$ and $g(\mathbf{X})$ are obtained in the first place. In the Bayesian optimization, these initial values are assumed to have Gaussian distributions, so the prior distribution can be expressed as;

$$g(\mathbf{x_{1:k}}) \sim \mathcal{N}(\mu_0(\mathbf{x_{1:k}}), \mathbf{\Sigma_0}(\mathbf{x_{1:k}}, \mathbf{x_{1:k}})), \tag{5.2}$$

where, $g(\mathbf{x_{1:k}})$, $\Sigma_0(\mathbf{x_{1:k}}, \mathbf{x_{1:k}})$ can be expressed as;

$$g(\mathbf{x_{1:k}}) = [g(\mathbf{x_1}),\ g(\mathbf{x_2}),\ \ldots,\ g(\mathbf{x_k})] \tag{5.3}$$

$$\Sigma_0(\mathbf{x_{1:k}}, \mathbf{x_{1:k}}) = \begin{pmatrix} \sum_0(\mathbf{x_1}, \mathbf{x_1}) & \sum_0(\mathbf{x_1}, \mathbf{x_2}) & \cdots & \sum_0(\mathbf{x_1}, \mathbf{x_k}) \\ \sum_0(\mathbf{x_2}, \mathbf{x_1}) & \sum_0(\mathbf{x_2}, \mathbf{x_2}) & \cdots & \sum_0(\mathbf{x_2}, \mathbf{x_k}) \\ \vdots & \vdots & \ddots & \vdots \\ \sum_0(\mathbf{x_k}, \mathbf{x_1}) & \sum_0(\mathbf{x_k}, \mathbf{x_2}) & \cdots & \sum_0(\mathbf{x_k}, \mathbf{x_k}) \end{pmatrix}. \tag{5.4}$$

Here, is expectations of $g(x)$ μ_x is the expectation of $g(x)$ around x, and $\Sigma_0(\mathbf{x_{1:k}}, \mathbf{x_{1:k}})$) is the covariance, or kernel, for any pair of two points x_i, x_j. There are many kernels to be consider, but taking the Gaussian kernel as an example, it can be expressed as follows;

$$\Sigma(x, x') = a_0 \exp(-\|\mathrm{x} - \mathrm{x}'\|^2), \tag{5.5}$$

where, a_0 is a constant value. Now, the distribution of $g\mathbf{x}$ at around the new point 点 $\mathbf{x}$ can be obtained using Bayes Theory as follows;

$$g(\mathbf{x})|g(\mathbf{x_{1:k}}) \sim \mathcal{N}(\mu_{\mathbf{n}}(\mathbf{x}), \sigma^2_{\mathbf{n}}(\mathbf{x})), \tag{5.6}$$

where, $\mu_n(x)$ and $\sigma_n^2(x)$ is expressed as follows, respectively [154];

$$\mu_n(x) = \Sigma_0(x, x_{1:k})\Sigma_0(x, x_{1:k})^{-1}(f(x_{1:k}) - \mu_0(x_{1:k})) + \mu_0(x)$$

$$\sigma_n^2(x) = \Sigma_0(x, x) - \Sigma_0(x, x_{1:k})\Sigma_0(x_{1:\mathrm{k}}, x_{1:\mathrm{k}}^{-1})\Sigma_0(x_{1:k}, x)$$

Next, in order to select next point $\mathbf{x}$ to explore requires to utilize an acquisition function. For example consider using the Expected Improvement as the acquisition function, then the selecting next point requires following steps. If the maximum reward value up to k trials is f_k^*, the maximum value after $k+1$ trials is either $f(\mathbf{x})$ or f_k^* obtained from the next search. Therefore, the maximum value after $k+1$ trials will be $\max(f(\mathbf{x}) - f_k^*)$. However, $f(\mathbf{x})$ can only be known after observation. Therefore, by using the posterior distribution from the equation (5.6), it is possible to search for the next point to be searched at the kth trial as $E_k(\mathbf{x}) = E[\max(f(\mathbf{x}) - f_k^*)]$. Therefore, the next search point is determined by calculating $\mathbf{x_{k+1}} = \mathrm{argmax}E_k((\mathbf{x}))$ [155, 156].

Waveform Generation of Multitone Signal Parameters for the transmit signal are amplitudes of each tones s, frequency band BW, phase of each subcarriers ϕ, frequency difference of each tones Δf. If the generated waveforms consist of N number of tones, there is $3N+1$ parameters are required as an input. Also, parameters have conditions where $0 \leq \phi \leq 359$, BW is chosen

a set from {1 kHz, 2 kHz, ..., 10 kHz, 20 kHz, ...,100 kHz, 200 kHz, ..., 1 MHz, 2 kHz, ..., 10 MHz}. I discretize subcarrier selection in a way that bandwidth is partitioned between 52 bins and subcarrier band is selected from 50 bins by excluding both sides of bins. In order to set waveforms output power to be the same, amplitudes are first selected from $0 < s < 1$, and then after that, signal amplitudes are normalized. Normalization has been done through $\mathbf{S} = \frac{s_i}{\sum_{i=1}^{N} s_i^2}$. The generated waveforms are expressed as follows,

$$f(\mathbf{X}) = \sum_{m=1}^{N} S_m \sin(2\pi(f + \Delta f_m)t + \phi_m), \Delta f_m \in BW \tag{5.7}$$

Output Voltage Feedback When feedback from the receiver, simple value needs to be performed. In wireless communication field, often CSIs can be utilized for the feedback. However, in such case, calculation cost of CSIs at the receiver side is very severe. Thus, the simply feedback output voltage using backscatter is the least possible method to be achieved for battery-less devices. True that it is also possible to implement implicit feedback where the receiver sends a pilot signal to the transmitter so that all the necessary calculation are pushed to transmitter side. For the case of battery-free devices, implicit feedback needs to be done through backscatter communication, which assumes that the channels are assumed to be reciprocal. In any case, actively sending feedback to a transmitter side does not my scope [86, 147].

Challenge One of the challenges arising from this solution is that it requires a lot of time to converge. Since this method is performed online learning approach, one epoch cost, send signal, measure output voltage, send back the value and re-design waveforms.

5.2.3 Achieve Multitone SWIPT for Larger Bandwidth

Similar to the related researches, the analyzed Multitone SWIPT encounters tradeoffs where the system can either optimize information sending or harvesting power, but not optimized for both at the same time. The information transfer works under the condition that the F_{ratio} is relatively small. In the region, however, power transfer capability does not quite good

since the saturation point of PCE requires relatively larger frequency spacings. As the F_{ratio} becomes large (either having a larger product of the storage capacitance and the load resistance or having a larger bandwidth), output PAPRs are getting small due to frequency cut occurred by the RC filter. Therefore, the PAPR differences depending on the selections of the multitone waveforms become closer to 0, which becomes challenging for WIT, in contrast to WPT. This becomes major problem when the larger bandwidth is allocated in higher carrier frequency waveforms. One of the solutions might be that the MAC level control needs to be introduced to send information mainly or transfer power mainly.

Additionally, the proposed SWIPT system needs to be fully implemented and evaluated the communication rate as well as power transfer rate in a real situation in order to validate the proposed method.

References

[1] N. Garg and R. Garg, "Energy harvesting in IoT devices: A survey," in *2017 International Conference on Intelligent Sustainable Systems (ICISS)*, 2017, pp. 127–131.

[2] V. Talla, B. Kellogg, S. Gollakota, and J. R. Smith, "Battery-Free Cellphone," *Proc. ACM Interact. Mob. Wearable Ubiquitous Technol.*, vol. 1, no. 2, pp. 25:1–25:20, Jun. 2017. [Online]. Available: http://doi.acm.org/10.1145/3090090

[3] C. H. P. Lorenz, S. Hemour, W. Li, Y. Xie, J. Gauthier, P. Fay, and K. Wu, "Breaking the Efficiency Barrier for Ambient Microwave Power Harvesting With Heterojunction Backward Tunnel Diodes," *IEEE Transactions on Microwave Theory and Techniques*, vol. 63, no. 12, pp. 4544–4555, 2015.

[4] N. Shinohara, "The wireless power transmission: inductive coupling, radio wave, and resonance coupling," *Wiley Interdisciplinary Reviews: Energy and Environment*, vol. 1, no. 3, pp. 337–346, 2012. [Online]. Available: http://dx.doi.org/10.1002/wene.43

[5] A. Kurs, A. Karalis, R. Moffatt, J. D. Joannopoulos, P. Fisher, and M. Soljačić, "Wireless Power Transfer via Strongly Coupled Magnetic Resonances," *Science*, vol. 317, no. 5834, pp. 83–86, 2007. [Online]. Available: https://science.sciencemag.org/content/317/5834/83

[6] T. Imura, *Wireless Power Transfer Using Magnetic and Electric Resonance Coupling Techniques*. Springer Singapore, 2020. [Online]. Available: https://www.springer.com/gp/book/9789811545795

[7] K. Sumiya, T. Sasatani, Y. Nishizawa, K. Tsushio, Y. Narusue, and Y. Kawahara, "Alvus: A Reconfigurable 2-D Wireless Charging System," *Proc. ACM Interact. Mob. Wearable Ubiquitous Technol.*, vol. 3, no. 2, Jun. 2019. [Online]. Available: https://doi.org/10.1145/3332533

[8] R. Takahashi, T. Sasatani, F. Okuya, Y. Narusue, and Y. Kawahara, "A Cuttable Wireless Power Transfer Sheet," *Proc. ACM Interact. Mob. Wearable Ubiquitous Technol.*, vol. 2, no. 4, Dec. 2018. [Online]. Available: https://doi.org/10.1145/3287068

[9] T. Sasatani, M. J. Chabalko, Y. Kawahara, and A. P. Sample, "Multimode Quasistatic Cavity Resonators for Wireless Power Transfer," *IEEE Antennas and Wireless Propagation Letters*, vol. 16, pp. 2746–2749, 2017.

[10] T. Sasatani, C. J. Yang, M. J. Chabalko, Y. Kawahara, and A. P. Sample, "Room-Wide Wireless Charging and Load-Modulation Communication via Quasistatic Cavity Resonance," *Proc. ACM Interact. Mob. Wearable Ubiquitous Technol.*, vol. 2, no. 4, Dec. 2018. [Online]. Available: https://doi.org/10.1145/3287066

[11] A. Harish and M. Sachidananda, *Antennas and Wave Propagation*, ser. Oxford higher education. Oxford University Press, 2007. [Online]. Available: https://books.google.co.jp/books?id=yjY3ngEACAAJ

[12] C. Capps, "Near field or far field?" *Edn -Boston then Denver then Highlands Ranch Co-*, vol. 46, pp. 95–102, 08 2001.

[13] 小. 篠原真毅, ワイヤレス給電技術-電磁誘導・共鳴送電からマイクロ波送電まで- *(*設計技術シリーズ*)*. 科学技術出版株式会社, 2020.

[14] W. C. Brown, "Experimental Airborne Microwave Supported Platform," *Tech. Rep. RADC-TR-65-188, Contract AF30(602) 3481*, December 1965.

[15] W. C. Brown, "Satellite power stations: a new source of energy?" *IEEE Spectrum*, vol. 10, no. 3, pp. 38–47, 1973.

[16] R. M. Dickinson and W. C. Brown, "Radiated Microwave Power Transmission System Efficiency Measurements," in *Technical Memo 33-727; jet Propulsion Lab., California Institute of Technology: Pasadena, CA*, March 15 1975, pp. 1–43.

[17] W. C. Brown, "The History of Power Transmission by Radio Waves," *IEEE Transactions on Microwave Theory and Techniques*, vol. 32, no. 9, pp. 1230–1242, 1984.

[18] X. Lu, P. Wang, D. Niyato, D. I. Kim, and Z. Han, "Wireless Networks With RF Energy Harvesting: A Contemporary Survey," *IEEE Communications Surveys Tutorials*, vol. 17, no. 2, pp. 757–789, Secondquarter 2015.

[19] N. Shinohara, "The wireless power transmission: inductive coupling, radio wave, and resonance coupling," *Wiley Interdisciplinary Reviews: Energy and Environment*, vol. 1, no. 3, pp. 337–346, 2012. [Online]. Available: http://dx.doi.org/10.1002/wene.43

[20] S. Hemour, Y. Zhao, C. H. P. Lorenz, D. Houssameddine, Y. Gui, C. Hu, and K. Wu, "Towards Low-Power High-Efficiency RF and Microwave Energy Harvesting," *IEEE Transactions on Microwave Theory and Techniques*, vol. 62, no. 4, pp. 965–976, April 2014.

[21] C. H. P. Lorenz, S. Hemour, and K. Wu, "Physical Mechanism and Theoretical Foundation of Ambient RF Power Harvesting Using Zero-Bias Diodes," *IEEE Transactions on Microwave Theory and Techniques*, vol. 64, no. 7, pp. 2146–2158, July 2016.

[22] J. Ou, S. Y. Zheng, A. S. Andrenko, Y. Li, and H. Tan, "Novel time-domain schottky diode modeling for microwave rectifier designs," *IEEE Transactions on Circuits and Systems I: Regular Papers*, vol. 65, no. 4, pp. 1234–1244, 2018.

[23] C. Wang, B. Yang, and N. Shinohara, "Study and Design of a 2.45-GHz Rectifier Achieving 91% Efficiency at 5-W Input Power," *IEEE Microwave and Wireless Components Letters*, vol. 31, no. 1, pp. 76–79, 2021.

[24] C. Wang, N. Shinohara, and T. Mitani, "Study on 5.8-GHz Single-Stage Charge Pump Rectifier for Internal Wireless System of Satellite," *IEEE Transactions on Microwave Theory and Techniques*, vol. 65, no. 4, pp. 1058–1065, 2017.

[25] R. Shigeta, T. Sasaki, D. M. Quan, Y. Kawahara, R. J. Vyas, M. M. Tentzeris, and T. Asami, "Ambient RF Energy Harvesting Sensor Device With Capacitor-Leakage-Aware Duty Cycle Control," *IEEE Sensors Journal*, vol. 13, no. 8, pp. 2973–2983, 2013.

[26] J. R. Smith, *History of the WISP Program*. New York, NY: Springer New York, 2013, pp. 13–29. [Online]. Available: https://doi.org/10.1007/978-1-4419-6166-2_2

[27] S. Naderiparizi, A. N. Parks, Z. Kapetanovic, B. Ransford, and J. R. Smith, "WISPCam: A Battery-Free RFID Camera," in *2015 IEEE International Conference on RFID (RFID)*, 2015, pp. 166–173.

[28] X. Lu, P. Wang, D. Niyato, D. I. Kim, and Z. Han, "Wireless Networks With RF Energy Harvesting: A Contemporary Survey," *IEEE Communications Surveys & Tutorials*, vol. 17, no. 2, pp. 757–789, 2015.

[29] C. Song, Y. Huang, J. Zhou, J. Zhang, S. Yuan, and P. Carter, "A High-Efficiency Broadband Rectenna for Ambient Wireless Energy Harvesting," *IEEE Transactions on Antennas and Propagation*, vol. 63, no. 8, pp. 3486–3495, 2015.

[30] C. Song, Y. Huang, P. Carter, J. Zhou, S. D. Joseph, and G. Li, "Novel Compact and Broadband Frequency-Selectable Rectennas for a Wide Input-Power and Load Impedance Range," *IEEE Transactions on Antennas and Propagation*, vol. 66, no. 7, pp. 3306–3316, 2018.

[31] N. Takabayashi, N. Shinohara, T. Mitani, M. Furukawa, and T. Fujiwara, "Rectification Improvement With Flat-Topped eams on 2.45-ghz Rectenna Arrays," *IEEE Transactions on Microwave Theory and Techniques*, vol. 68, no. 3, pp. 1151–1163, 2020.

[32] Y. Huang, N. Shinohara, and T. Mitani, "Impedance Matching in Wireless Power Transfer," *IEEE Transactions on Microwave Theory and Techniques*, vol. 65, no. 2, pp. 582–590, 2017.

[33] D. Pozar, *Microwave Engineering, 4th Edition*. Wiley, 2011. [Online]. Available: https://books.google.co.jp/books?id=JegbAAAAQBAJ

[34] P. P. Wang, H. Jiang, L. Gao, P. Sen, Y. Kim, G. M. Rebeiz, P. P. Mercier, and D. A. Hall, "A Near-Zero-Power Wake-Up Receiver Achieving − 69-dBm Sensitivity," *IEEE Journal of Solid-State Circuits*, vol. 53, no. 6, pp. 1640–1652, 2018.

[35] C. L. J. Park and C. Park, "An Asymmetric-Width Broad-Side Coupled Transformer to Reduce the Parasitic Coupling Capacitancefor CMOS Power Amplifier Applications," *Progress in Electromagnetics Research M*, vol. 78, pp. 93–101, 2019.

[36] A. Lim, A. Tan, Z.-H. Kong, and K. Ma, "A Design Methodology and Analysis for Transformer-Based Class-E Power Amplifier," *Electronics*, vol. 8, no. 5, 2019. [Online]. Available: https://www.mdpi.com/2079-9292/8/5/494

[37] R. Bajwa and M. K. Yapici, "Integrated On-Chip Transformers: Recent Progress in the Design, Layout, Modeling and Fabrication," *Sensors*, vol. 19, no. 16, 2019. [Online]. Available: https://www.mdpi.com/1424-8220/19/16/3535

[38] X. Gu, L. Guo, S. Hemour, and K. Wu, "Optimum Temperatures for Enhanced Power Conversion Efficiency (pce) of Zero-Bias Diode-Based Rectifiers," *IEEE Transactions on Microwave Theory and Techniques*, vol. 68, no. 9, pp. 4040–4053, 2020.

[39] K. Rasilainen, J. Ilvonen, A. Lehtovuori, J. Hannula, and V. Viikari, "On Design and Evaluation of Harmonic Transponders," *IEEE Transactions on Antennas and Propagation*, vol. 63, no. 1, pp. 15–23, 2015.

[40] L. Guo, X. Gu, P. Chu, S. Hemour, and K. Wu, "Collaboratively Harvesting Ambient Radiofrequency and Thermal Energy," *IEEE Transactions on Industrial Electronics*, vol. 67, no. 5, pp. 3736–3746, 2020.

[41] R. N. Hall, "Tunnel diodes," *IRE Transactions on Electron Devices*, vol. 7, no. 1, pp. 1–9, 1960.

[42] C. A. Burrus, "Backward Diodes for Low-level Millimeter-Wave Detection," *IEEE Transactions on Microwave Theory and Techniques*, vol. 11, no. 5, pp. 357–362, 1963.

[43] F. Amato, C. W. Peterson, M. B. Akbar, and G. D. Durgin, "Long Range and Low Powered RFID Tags with Tunnel Diode," in *2015 IEEE International Conference on RFID Technology and Applications (RFID-TA)*, 2015, pp. 182–187.

[44] C. Qi, F. Amato, M. Alhassoun, and G. D. Durgin, "Breaking the Range Limit of RFID Localization: Phase-based Positioning with Tunneling Tags," in *2019 IEEE International Conference on RFID (RFID)*, 2019, pp. 1–8.

[45] A. Varshney, A. Soleiman, and T. Voigt, "TunnelScatter: Low Power Communication for Sensor Tags Using Tunnel Diodes," in *The 25th Annual International Conference on Mobile Computing and Networking*, ser. MobiCom '19. New York, NY, USA: Association for Computing Machinery, 2019. [Online]. Available: https://doi.org/10.1145/3300061.3345451

[46] A. Varshney and L. Corneo, "Tunnel Emitter: Tunnel Diode Based Low-Power Carrier Emitters for Backscatter Tags," in *Proceedings of the 26th Annual International Conference on Mobile Computing and Networking*. New York, NY, USA: Association for Computing Machinery, 2020. [Online]. Available: https://doi.org/10.1145/3372224.3419199

[47] T. Nakada and H. Nakamura, *Normally-Off Computing*. Tokyo: Springer Japan, 2017, pp. 57–63. [Online]. Available: https://doi.org/10.1007/978-4-431-56505-5_4

[48] M. Magno, V. Jelicic, B. Srbinovski, V. Bilas, E. Popovici, and L. Benini, "Design, Implementation, and Performance Evaluation of a Flexible Low-Latency Nanowatt Wake-Up Radio Receiver," *IEEE Transactions on Industrial Informatics*, vol. 12, no. 2, pp. 633–644, 2016.

[49] L. Zhang, J. Liu, H. Jiang, and Y. Guan, "Senstrack: Energy-efficient location tracking with smartphone sensors," *IEEE Sensors Journal*, vol. 13, no. 10, pp. 3775–3784, Oct 2013.

[50] M. Takagi, Y. Kawahara, and T. Asami, "A Low-Power Sensing Method Using Linux Kernel on Android Devices," in *Proceedings of the 13th ACM Conference on Embedded Networked Sensor Systems*, ser. SenSys '15. New York, NY, USA: ACM, 2015, pp. 413–414. [Online]. Available: http://doi.acm.org/10.1145/2809695.2817890

[51] R. Pérez-Torres and C. Torres-Huitzil, "A power-aware middleware for location amp; context aware mobile apps with cloud computing interaction," in *2012 World Congress on Information and Communication Technologies*, Oct 2012, pp. 691–696.

[52] A. J. Perez, M. A. Labrador, and S. J. Barbeau, "G-sense: a scalable architecture for global sensing and monitoring," *IEEE Network*, vol. 24, no. 4, pp. 57–64, Jul 2010.

[53] S. Naderiparizi, M. Hessar, V. Talla, S. Gollakota, and J. R. Smith, "Towards Battery-Free HD Video Streaming," in *15th USENIX Symposium on Networked Systems Design and Implementation (NSDI 18)*. Renton, WA: USENIX Association, 2018, pp. 233–247. [Online]. Available: https://www.usenix.org/conference/nsdi18/presentation/naderiparizi

[54] V. Talla, B. Kellogg, B. Ransford, S. Naderiparizi, S. Gollakota, and J. R. Smith, "Powering the Next Billion Devices with Wi-fi," in *Proceedings of the 11th ACM Conference on Emerging Networking Experiments and Technologies*, ser. CoNEXT '15. New York, NY, USA: ACM, 2015, pp. 4:1–4:13. [Online]. Available: http://doi.acm.org/10.1145/2716281.2836089

[55] V. Liu, A. Parks, V. Talla, S. Gollakota, D. Wetherall, and J. R. Smith, "Ambient Backscatter: Wireless Communication out of Thin Air," *SIGCOMM Comput. Commun. Rev.*, vol. 43, no. 4, pp. 39–50, Aug. 2013. [Online]. Available: http://doi.acm.org/10.1145/2534169.2486015

[56] Y. Huang and B. Clerckx, "Large-Scale Multiantenna Multisine Wireless Power Transfer," *IEEE Transactions on Signal Processing*, vol. 65, no. 21, pp. 5812–5827, Nov 2017.

[57] J. Liu, K. Xiong, P. Fan, and Z. Zhong, "Resource Allocation in Wireless Powered Sensor Networks With Circuit Energy Consumption Constraints," *IEEE Access*, vol. 5, pp. 22 775–22 782, 2017.

[58] T. D. Ponnimbaduge Perera, D. N. K. Jayakody, S. K. Sharma, S. Chatzinotas, and J. Li, "Simultaneous Wireless Information and Power Transfer (SWIPT): Recent Advances and Future Challenges," *IEEE Communications Surveys Tutorials*, vol. 20, no. 1, pp. 264–302, Firstquarter 2018.

[59] M. Giordani, M. Polese, M. Mezzavilla, S. Rangan, and M. Zorzi, "Toward 6G Networks: Use Cases and Technologies," *IEEE Communications Magazine*, vol. 58, no. 3, pp. 55–61, March 2020.

[60] Y. Nishizawa, T. Sasatani, M. Ishige, Y. Narusue, T. Umedachi, and Y. Kawahara, "Ramus: A frequency-multiplexed power bus for powering, sensing and controlling robots," *IEEE Robotics and Automation Letters*, vol. 5, no. 3, pp. 4126–4132, 2020.

[61] X. He, R. Wang, J. Wu, and W. Li, "Nature of power electronics and integration of power conversion with communication for talkative power," *Nature Communications*, vol. 11, no. 1, p. 2479, 2020.

[62] Z. Hu, N. Wei, and Z. Zhang, "Optimal Resource Allocation for Harvested Energy Maximization in Wideband Cognitive Radio Network With SWIPT," *IEEE Access*, vol. 5, pp. 23 383–23 394, 2017.

[63] R. Zhang and C. K. Ho, "MIMO Broadcasting for Simultaneous Wireless Information and Power Transfer," *IEEE Transactions on Wireless Communications*, vol. 12, no. 5, pp. 1989–2001, 2013.

[64] K. Tutuncuoglu and A. Yener, "Optimum Transmission Policies for Battery Limited Energy Harvesting Nodes," *IEEE Transactions on Wireless Communications*, vol. 11, no. 3, pp. 1180–1189, 2012.

[65] Y. Zeng, B. Clerckx, and R. Zhang, "Communications and Signals Design for Wireless Power Transmission," *IEEE Transactions on Communications*, vol. 65, no. 5, pp. 2264–2290, May 2017.

[66] M. Rajabi, N. Pan, S. Claessens, S. Pollin, and D. Schreurs, "Modulation Techniques for Simultaneous Wireless Information and Power Transfer With an Integrated Rectifier–Receiver," *IEEE Transactions on Microwave Theory and Techniques*, vol. 66, no. 5, pp. 2373–2385, May 2018.

[67] S. Claessens, N. Pan, D. Schreurs, and S. Pollin, "Multitone FSK Modulation for SWIPT," *IEEE Transactions on Microwave Theory and Techniques*, vol. 67, no. 5, pp. 1665–1674, May 2019.

[68] B. Clerckx, "Wireless Information and Power Transfer: Nonlinearity, Waveform Design, and Rate-Energy Tradeoff," *IEEE Transactions on Signal Processing*, vol. 66, no. 4, pp. 847–862, Feb 2018.

[69] 床木裕樹, "ワイヤレス電力伝送システムの国際制度化・標準化の最新動向," *Journal of the ITU Association of Japan*, vol. 48, no. 3, pp. 29–33, 2018.

[70] 篠原真毅 and 床木裕樹, "ワイヤレス電力伝送の技術，制度化，標準化最新動向," *The Journal of Institute of Electronics, Information and Communication Engineers*, vol. 101, no. 1, pp. 79–84, 2018.

[71] ITU-R, "Applications of wireless power transmission via radio frequency beam," https://www.itu.int/pub/R-REP-SM.2392-2016, 2016 (accessed December 30, 2020).

[72] ——, "Proposed new working document towards a pdn recommendation itu-r sm.[wpt.beam.frq]," https://www.itu.int/md/R15-WP1A.AR-C-0168/en, 2019 (accessed December 30, 2020).

[73] N. Shinohara, "Wireless Power Transfer in Japan: Regulations and Activities," in *2020 14th European Conference on Antennas and Propagation (EuCAP)*, 2020, pp. 1–4.

[74] ブロードバンドワイヤレスフォーラム (BWF)WPT-WG", "「空間伝送型ワイヤレス電力伝送システムの技術的条件」に関する提案," https://www.soumu.go.jp/main_content/000611759.pdf, 2019 (accessed December 30, 2020).

[75] W. P. T. C. for Practical Applications (WiPoT), "Wireless power transfer for practical application," http://www.wipot.jp/english/, note = 2015 (accessed December 30, 2020).

[76] A. of Radio Industries & Businesses (ARIB) Standard, "920MHz-BAND RFID EQUIPMENT FOR PREMISES RADIO STATION AND LAND MOBILE RADIO STATION," http://www.arib.or.jp/english/html/overview/doc/5-STD-T106v2_0-E1.pdf, year = 2019 (accessed December 30, 2020).

[77] 一般社団法人日本自動認識システム協会研究開発センター RFID 担当, “Rfid の基礎,” https://www.jaisa.or.jp/about/pdfs/20190329rev8.pdf, year = 2019 (accessed December 30, 2020).

[78] 荒井雅行, “Rfid リーダの技術と課題,” 電子情報通信学会　通信ソサイエティマガジン, vol. 2008, no. 7, pp. 41–50, 2008.

[79] M. S. Trotter, J. D. Griffin, and G. D. Durgin, “Power-Optimized Waveforms for Improving the Range and Reliability of RFID Systems,” in *2009 IEEE International Conference on RFID*, April 2009, pp. 80–87.

[80] A. Collado and A. Georgiadis, “Improving Wireless Power Transmission Efficiency Using Chaotic Waveforms,” in *2012 IEEE/MTT-S International Microwave Symposium Digest*, June 2012, pp. 1–3.

[81] ——, “Optimal Waveforms for Efficient Wireless Power Transmission,” *IEEE Microwave and Wireless Components Letters*, vol. 24, no. 5, pp. 354–356, May 2014.

[82] F. Bolos, J. Blanco, A. Collado, and A. Georgiadis, “RF Energy Harvesting From Multi-Tone and Digitally Modulated Signals,” *IEEE Transactions on Microwave Theory and Techniques*, vol. 64, no. 6, pp. 1918–1927, June 2016.

[83] A. S. Boaventura and N. B. Carvalho, “Maximizing DC Power in Energy Harvesting Circuits Using Multisine Excitation,” in *2011 IEEE MTT-S International Microwave Symposium*, June 2011, pp. 1–4.

[84] C. R. Valenta, M. M. Morys, and G. D. Durgin, “Theoretical Energy-Conversion Efficiency for Energy-Harvesting Circuits Under Power-Optimized Waveform Excitation,” *IEEE Transactions on Microwave Theory and Techniques*, vol. 63, no. 5, pp. 1758–1767, May 2015.

[85] B. Clerckx, E. Bayguzina, D. Yates, and P. D. Mitcheson, “Waveform Optimization for Wireless Power Transfer with Nonlinear Energy Harvester Modeling,” in *2015 International Symposium on Wireless Communication Systems (ISWCS)*, Aug 2015, pp. 276–280.

[86] B. Clerckx and E. Bayguzina, “Waveform Design for Wireless Power Transfer,” *IEEE Transactions on Signal Processing*, vol. 64, no. 23, pp. 6313–6328, Dec 2016.

[87] ——, “Low-Complexity Adaptive Multisine Waveform Design for Wireless Power Transfer,” *IEEE Antennas and Wireless Propagation Letters*, vol. 16, pp. 2207–2210, 2017.

[88] B. Clerckx and J. Kim, “On the Beneficial Roles of Fading and Transmit Diversity in Wireless Power Transfer With Nonlinear Energy Harvesting,” *IEEE Transactions on Wireless Communications*, vol. 17, no. 11, pp. 7731–7743, Nov 2018.

[89] M. D. Prete, A. Costanzo, M. Magno, D. Masotti, and L. Benini, "Optimum Excitations for a Dual-Band Microwatt Wake-Up Radio," *IEEE Transactions on Microwave Theory and Techniques*, vol. 64, no. 12, pp. 4731–4739, Dec 2016.

[90] Z. Liu, Z. Zhong, and Y. Guo, "In Vivo High-Efficiency Wireless Power Transfer With Multisine Excitation," *IEEE Transactions on Microwave Theory and Techniques*, vol. 65, no. 9, pp. 3530–3540, Sep. 2017.

[91] N. Decarli, M. Del Prete, D. Masotti, D. Dardari, and A. Costanzo, "High-Accuracy Localization of Passive Tags With Multisine Excitations," *IEEE Transactions on Microwave Theory and Techniques*, vol. 66, no. 12, pp. 5894–5908, 2018.

[92] D. Vasisht, G. Zhang, O. Abari, H.-M. Lu, J. Flanz, and D. Katabi, "In-Body Backscatter Communication and Localization," in *Proceedings of the 2018 Conference of the ACM Special Interest Group on Data Communication*, ser. SIGCOMM '18. New York, NY, USA: Association for Computing Machinery, 2018, pp. 132—-146. [Online]. Available: https://doi.org/10.1145/3230543.3230565

[93] M. Rostami, K. Sundaresan, E. Chai, S. Rangarajan, and D. Ganesan, "Redefining Passive in Backscattering with Commodity Devices," in *Proceedings of the 26th Annual International Conference on Mobile Computing and Networking*, ser. MobiCom '20. New York, NY, USA: Association for Computing Machinery, 2020. [Online]. Available: https://doi.org/10.1145/3372224.3380880

[94] R. Zhao, F. Zhu, Y. Feng, S. Peng, X. Tian, H. Yu, and X. Wang, "OFDMA-Enabled Wi-Fi Backscatter," in *The 25th Annual International Conference on Mobile Computing and Networking*, ser. MobiCom '19. New York, NY, USA: Association for Computing Machinery, 2019. [Online]. Available: https://doi.org/10.1145/3300061.3300121

[95] N. Neshatvar, L. Regnacq, D. Jiang, Y. Wu, and A. Demosthenous, "Monitoring Myocardial Edema Tissue with Electrical Impedance Spectroscopy," in *2020 IEEE International Symposium on Circuits and Systems (ISCAS)*, 2020, pp. 1–4.

[96] H. Zappen, F. Ringbeck, and D. U. Sauer, "Application of Time-Resolved Multi-Sine Impedance Spectroscopy for Lithium-Ion Battery Characterization," *Batteries*, vol. 4, no. 4, 2018. [Online]. Available: https://www.mdpi.com/2313-0105/4/4/64

[97] B. Sanchez, G. Vandersteen, R. Bragos, and J. Schoukens, "Optimal multisine excitation design for broadband electrical impedance spectroscopy," *Measurement Science and Technology*, vol. 22, no. 11, p. 115601, sep 2011. [Online]. Available: https://doi.org/10.1088/0957-0233/22/11/115601

[98] S. Claessens, N. Pan, M. Rajabi, D. Schreurs, and S. Pollin, "Enhanced Biased ASK Modulation Performance for SWIPT With AWGN Channel and Dual-Purpose Hardware," *IEEE Transactions on Microwave Theory and Techniques*, vol. 66, no. 7, pp. 3478–3486, July 2018.

[99] D. I. Kim, J. H. Moon, and J. J. Park, "New SWIPT Using PAPR: How It Works," *IEEE Wireless Communications Letters*, vol. 5, no. 6, pp. 672–675, Dec 2016.

[100] J. Kim, B. Clerckx, and P. D. Mitcheson, "Experimental Analysis of Harvested Energy and Throughput Trade-off in a Realistic SWIPT System," in *2019 IEEE Wireless Power Transfer Conference (WPTC)*, June 2019, pp. 1–6.

[101] S. Claessens, Y. T. Chang, D. Schreurs, and S. Pollin, "Receiving ASK-OFDM in Low Power SWIPT Nodes without Local Oscillators," in *2019 IEEE Wireless Power Transfer Conference (WPTC)*, 2019, pp. 20–25.

[102] D. Tse and P. Viswanath, *Fundamentals of Wireless Communication*. Cambridge University Press, 2005.

[103] M. S. Varela and M. G. Sanchez, "Rms delay and coherence bandwidth measurements in indoor radio channels in the uhf band," *IEEE Transactions on Vehicular Technology*, vol. 50, no. 2, pp. 515–525, 2001.

[104] N. Pan, D. Belo, M. Rajabi, D. Schreurs, N. B. Carvalho, and S. Pollin, "Bandwidth Analysis of RF-DC Converters Under Multisine Excitation," *IEEE Transactions on Microwave Theory and Techniques*, vol. 66, no. 2, pp. 791–802, Feb 2018.

[105] T. Hirakawa, C. Wang, and N. Shinohara, "RF-DC Conversion Efficiency Improvement for Microwave Transmission with Pulse Modulation," *Wireless Power Transfer*, vol. 6, no. 1, p. 57–66, 2019.

[106] M. S. Trotter and G. D. Durgin, "Survey of Range Improvement of Commercial RFID Tags with Power Optimized Waveforms," in *2010 IEEE International Conference on RFID (IEEE RFID 2010)*, April 2010, pp. 195–202.

[107] N. B. Carvalho, K. A. Remley, D. Schreurs, and K. G. Gard, "Multisine signals for wireless system test and design [application notes]," *IEEE Microwave Magazine*, vol. 9, no. 3, pp. 122–138, 2008.

[108] C. R. Valenta and G. D. Durgin, "Harvesting Wireless Power: Survey of Energy-Harvester Conversion Efficiency in Far-Field, Wireless Power Transfer Systems," *IEEE Microwave Magazine*, vol. 15, no. 4, pp. 108–120, June 2014.

[109] H. Gomes, A. R. Testera, N. B. Carvalho, M. F. Barciela, and K. A. Remley, "The Impact of Long-term Memory Effects on Diode Power Probes," in *2010 IEEE MTT-S International Microwave Symposium*, May 2010, pp. 596–599.

[110] S. Farsi, P. Draxler, H. Gheidi, B. K. J. C. Nauwelaers, P. Asbeck, and D. Schreurs, "Characterization of Intermodulation and Memory Effects Using Offset Multisine Excitation," *IEEE Transactions on Microwave Theory and Techniques*, vol. 62, no. 3, pp. 645–657, 2014.

[111] A. Boaventura, D. Belo, R. Fernandes, A. Collado, A. Georgiadis, and N. B. Carvalho, "Boosting the Efficiency: Unconventional Waveform Design for Efficient Wireless Power Transfer," *IEEE Microwave Magazine*, vol. 16, no. 3, pp. 87–96, April 2015.

[112] M. Jordão, R. Correia, and N. B. Carvalho, "Multi-Sine Channel Optimization for RF-to-dc Performance Characterization," *URSI Radio Science Bulletin*, vol. 2018, no. 364, pp. 39–11, 2018.

[113] A. Boaventura, N. B. Carvalho, and A. Georgiadis, "The Impact of Multi-Sine Tone Separation on RF-DC Efficiency," in *2014 Asia-Pacific Microwave Conference*, 2014, pp. 606–609.

[114] A. J. S. Boaventura and N. Carvalho, "Extending Reading Range of Commercial RFID Readers," *IEEE Transactions on Microwave Theory and Techniques*, vol. 61, no. 1, pp. 633–640, 2013.

[115] A. J. Soares Boaventura, A. Collado, A. Georgiadis, and N. Borges Carvalho, "Spatial Power Combining of Multi-Sine Signals for Wireless Power Transmission Applications," *IEEE Transactions on Microwave Theory and Techniques*, vol. 62, no. 4, pp. 1022–1030, April 2014.

[116] N. Shariati, J. R. Scott, D. Schreurs, and K. Ghorbani, "Multitone Excitation Analysis in RF Energy Harvesters–Considerations and Limitations," *IEEE Internet of Things Journal*, vol. 5, no. 4, pp. 2804–2816, Aug 2018.

[117] T. Ikeuchi, Y. Kawahara, and J. R. Smith, "Experimental Characterization of Narrowband Power Optimized Waveforms," in *2019 IEEE Wireless Power Transfer Conference (WPTC)*, June 2019, pp. 1–6.

[118] B. Clerckx, Z. B. Zawawi, and K. Huang, "Wirelessly Powered Backscatter Communications: Waveform Design and SNR-Energy Tradeoff," *IEEE Communications Letters*, vol. 21, no. 10, pp. 2234–2237, Oct 2017.

[119] N. Pan, S. Claessens, M. Rajabi, D. Schreurs, and S. Pollin, "Multi-sine Wireless Power Transfer with a Realistic Channel and Rectifier Model," in *2017 IEEE Wireless Power Transfer Conference (WPTC)*, May 2017, pp. 1–4.

[120] D. Belo and N. B. Carvalho, "Harmonic Spaced Multisines for Efficient Wireless Power Transmission," in *2015 IEEE Wireless Power Transfer Conference (WPTC)*, 2015, pp. 1–4.

[121] C. A. Balanis, *Antenna theory: analysis and design*. Wiley-Interscience, 2005.

[122] Coilcraft, "Chip Inductors 0603CS (1608)," https://www.coilcraft.com/getmedia/022eb894-7253-40d0-b07c-650d362fc80e/0603cs.pdf, 2020 (accessed October 15, 2020).

[123] MICRONIX, "Anechoic chamber my5310 5410," http://www.micronix-jp.com/file-download/catalog/pdf/my5310_5410.pdf, 2020 (accessed October 28, 2020).

[124] G. Dold, *RSWaveGenerator*, (accessed October 28, 2020). [Online]. Available: https://github.com/gdold/RSWaveformGenerator

[125] T. M. Inc., "Awgn channel," https://www.mathworks.com/help/comm/ug/awgn-channel.html, 2020 (accessed 2020-11-15).

[126] Powercast, "P2110B Module Datasheet," https://www.powercastco.com/documentation/p2110b-module-datasheet, 2020.

[127] "Operation within the bands 902–928 mhz, 2400–2483.5 mhz, and 5725–5850 mhz."

[128] C. R. Valenta and G. D. Durgin, "Rectenna Performance Under Power-Optimized Waveform Excitation," in *2013 IEEE International Conference on RFID (RFID)*, 2013, pp. 237–244.

[129] "WISP 5," https://github.com/wisp/wisp5, (accessed 2020-09-15).

[130] M. Weiser, "The Computer for the 21st Century," *Scientific American*, vol. 265, no. 3, pp. 66–75, January 1991. [Online]. Available: http://www.ubiq.com/hypertext/weiser/SciAmDraft3.html

[131] I. Krikidis, S. Timotheou, S. Nikolaou, G. Zheng, D. W. K. Ng, and R. Schober, "Simultaneous wireless information and power transfer in modern communication systems," *IEEE Communications Magazine*, vol. 52, no. 11, pp. 104–110, 2014.

[132] Z. Hu, C. Yuan, and F. Gao, "Maximizing Harvested Energy for Full-Duplex SWIPT System With Power Splitting," *IEEE Access*, vol. 5, pp. 24 975–24 987, 2017.

[133] R. Jiang, K. Xiong, P. Fan, Y. Zhang, and Z. Zhong, "Optimal Design of SWIPT Systems With Multiple Heterogeneous Users Under Non-linear Energy Harvesting Model," *IEEE Access*, vol. 5, pp. 11 479–11 489, 2017.

[134] B. Clerckx, R. Zhang, R. Schober, D. W. K. Ng, D. I. Kim, and H. V. Poor, "Fundamentals of Wireless Information and Power Transfer: From RF Energy Harvester Models to Signal and System Designs," *IEEE Journal on Selected Areas in Communications*, vol. 37, no. 1, pp. 4–33, Jan 2019.

[135] E. Boshkovska, D. W. K. Ng, N. Zlatanov, and R. Schober, "Practical Non-Linear Energy Harvesting Model and Resource Allocation for SWIPT Systems," *IEEE Communications Letters*, vol. 19, no. 12, pp. 2082–2085, 2015.

[136] E. Bayguzina and B. Clerckx, "Asymmetric Modulation Design for Wireless Information and Power Transfer With Nonlinear Energy Harvesting," *IEEE Transactions on Wireless Communications*, vol. 18, no. 12, pp. 5529–5541, 2019.

[137] F. Bolos, J. Blanco, A. Collado, and A. Georgiadis, "RF Energy Harvesting From Multi-Tone and Digitally Modulated Signals," *IEEE Transactions on Microwave Theory and Techniques*, vol. 64, no. 6, pp. 1918–1927, June 2016.

[138] C. Im, J. Lee, and C. Lee, "A Multi-Tone Amplitude Modulation Scheme for Wireless Information and Power Transfer," *IEEE Transactions on Vehicular Technology*, vol. 69, no. 1, pp. 1147–1151, 2020.

[139] N. Pan, M. Rajabi, S. Claessens, D. Schreurs, and S. Pollin, "Transmission Strategy for Simultaneous Wireless Information and Power Transfer with a Non-Linear Rectifier Model," *Electronics*, vol. 9, p. 1082, 07 2020.

[140] H. Abbasizadeh, S. Y. Kim, B. Samadpoor Rikan, A. Hejazi, D. Khan, Y. G. Pu, K. C. Hwang, Y. Yang, D. I. Kim, and K.-Y. Lee, "Design of a 900 MHz Dual-Mode SWIPT for Low-Power IoT Devices," *Sensors*, vol. 19, no. 21, 2019. [Online]. Available: https://www.mdpi.com/1424-8220/19/21/4676

[141] "Wireless Technology Services," \\http://www.powercastco.com/, (accessed 2016-10-02). [Online]. Available: http://www.powercastco.com/

[142] B. A. Mouris, H. Ghauch, R. Thobaben, and B. L. G. Jonsson, "Multi-Tone Signal Optimization for Wireless Power Transfer in the Presence of Wireless Communication Links," *IEEE Transactions on Wireless Communications*, vol. 19, no. 5, pp. 3575–3590, 2020.

[143] S. A. Bassam, M. Helaoui, and F. M. Ghannouchi, "Crossover Digital Predistorter for the Compensation of Crosstalk and Nonlinearity in MIMO Transmitters," *IEEE Transactions on Microwave Theory and Techniques*, vol. 57, no. 5, pp. 1119–1128, 2009.

[144] X. Liu, Q. Zhang, W. Chen, H. Feng, L. Chen, F. M. Ghannouchi, and Z. Feng, "Beam-Oriented Digital Predistortion for 5g Massive MIMO Hybrid Beamforming Transmitters," *IEEE Transactions on Microwave Theory and Techniques*, vol. 66, no. 7, pp. 3419–3432, 2018.

[145] B. Clerckx, G. Kim, J. Choi, and Y. Hong, "Explicit vs. implicit feedback for su and mu-mimo," in *2010 IEEE Global Telecommunications Conference GLOBECOM 2010*, 2010, pp. 1–5.

[146] R. Wang and D. R. Brown, "Optimal wireless power transfer with distributed transmit beamforming," *Journal of Communications and Networks*, vol. 19, no. 2, pp. 134–146, 2017.

[147] J. Kim, B. Clerckx, and P. D. Mitcheson, "Prototyping and experimentation of a closed-loop wireless power transmission with channel acquisition and waveform optimization," in *2017 IEEE Wireless Power Transfer Conference (WPTC)*, May 2017, pp. 1–4.

[148] M. Varasteh, J. Hoydis, and B. Clerckx, "Learning to communicate and energize: Modulation, coding, and multiple access designs for wireless information-power transmission," *IEEE Transactions on Communications*, vol. 68, no. 11, pp. 6822–6839, 2020.

[149] K. Huang and X. Zhou, "Cutting the last wires for mobile communications by microwave power transfer," *IEEE Communications Magazine*, vol. 53, no. 6, pp. 86–93, 2015.

[150] K. W. Choi, D. I. Kim, and M. Y. Chung, "Received power-based channel estimation for energy beamforming in multiple-antenna rf energy transfer system," *IEEE Transactions on Signal Processing*, vol. 65, no. 6, pp. 1461–1476, 2017.

[151] P. S. Yedavalli, T. Riihonen, X. Wang, and J. M. Rabaey, "Far-Field RF Wireless Power Transfer with Blind Adaptive Beamforming for Internet of Things Devices," *IEEE Access*, vol. 5, pp. 1743–1752, 2017.

[152] G. Yang, C. K. Ho, and Y. L. Guan, "Multi-antenna wireless energy transfer for backscatter communication systems," *IEEE Journal on Selected Areas in Communications*, vol. 33, no. 12, pp. 2974–2987, 2015.

[153] C. E. Rasmussen and C. K. I. Williams, *Gaussian Processes for Machine Learning (Adaptive Computation and Machine Learning)*. The MIT Press, 2005.

[154] ——, *Gaussian Processes for Machine Learning (Adaptive Computation and Machine Learning)*. The MIT Press, 2005.

[155] P. I. Frazier, "A tutorial on bayesian optimization," *arXiv*, 2018.

[156] E. Brochu, V. M. Cora, and N. de Freitas, "A tutorial on bayesian optimization of expensive cost functions, with application to active user modeling and hierarchical reinforcement learning," *arXiv*, 2010.

Publication List for This Thesis

Journal

[J1] T. Ikeuchi, Y. Kawahara, "Peak to Average Power Ratio Based Signal Detection for Frequency Shift Multitone SWIPT System, " in IEEE ACCESS, vol. 9, pp. 4158–4172, 2021, doi: 10.1109/ACCESS.2020.3048193.

[J2] T. Ikeuchi, J. R. Smith, Y. Kawahara, "Bandwidth Characterization of Multitone UHF Power Transfer Waveforms, " Wireless Power Transfer **Under review**

International Conference

[C1] T. Ikeuchi, J. R. Smith, Y. Kawahara, "Experimental Characterization of Narrowband Power Optimized Waveforms, " Proceedings of IEEE Wireless Power Transfer Conference (WPTC), London, United Kingdom, pp. 6–11, 2019.

[C2] T. Ikeuchi, Y. Kawahara, "Signal Detection Method Based on Peak to Average Ratio for Frequency Shift Multitone SWIPT System, " Proceedings of IEEE Wireless Power Transfer Conference (WPTC), Seoul, South Korea, pp. 119–122, 2020.

Publication List Excluded from This Thesis

Journal

[J3] 高木雅, 池内尚史, 川原圭博, 浅見徹, “マイクロ波給電を応用したスマートフォンの外付け電源管理システム, ” 情報処理学会論文誌, Vol. 59, No, 10, pp. 1802–1813 (2018.10), ISSN 1882-7764, Oct. 2018.

International Conference / Workshop

[C3] M. Takagi, T. Ikeuchi, Y. Kawahara, “WakeDroid: a Remote Boot Trigger for Android Devices as IoT Nodes, ”Proceedings of IEEE International Conference on Communications (ICC), W04-S1 EHWC, Kansas City, MO, USA, May, 2018.

Domestic Symposium / Conference

[D1] 池内尚史, 高木雅, 川原圭博, 浅見徹, “マイクロ波給電を用いた Android スマートフォンの遠隔起動トリガの実験的検討, ” 情報処理学会ユビキタスコンピューティングシステム研究会, Oct 2016.

[D2] 池内尚史, 高木雅, 石毛真修, 角谷和宣, 川原圭博, 浅見徹, “B-18-2 Android スマートフォン遠隔起動トリガの遠隔監視システム, ” 電子情報通信学会総合大会講演論文集, Mar 2017.

[D3] 池内尚史, 高木雅, 角谷和宣, 邱浩, 高宮真, 川原圭博, “スマートフォンを用いた間欠的センシングのための外付け電源管理システムの設計, ” 情報処理学会全国大会, Mar 2018.

[D4] 高木雅, 池内尚史, 川原圭博, “B-18-1 Android 端末による間欠センシングのためのマイクロ波給電を用いた選択的遠隔起動トリガ, ” 電子情報通信学会総合大会講演論文集, Mar 2017.

[D5] 石毛真修, 高木雅, 池内尚史, 川原圭博, 浅見徹, “スマートフォンを用いた間欠的センシングのための外付け電源管理システムの設計, ” 情報処理学会全国大会, Mar 2017.

Awards

[A1] 52thInformation Processing Society of Japan (IPSJ) Ubiquitous Computing System (UBI) 研究会, 学生奨励賞受賞 (2016)

[A2] Cisco Systems Virtual Hackathon Asia Passific Award

[A3] IEICE WPT mini 4wd circuit race (2nd award)